Bottom-up generation of synthetic cells and tissues using microfluidic devices for double emulsion generation

by

Kaitlyn E. E. Ramsay

B.Sc. Hons., Queen's University, 2017

A Dissertation Submitted in Partial Fulfillment of the

Requirements for the Degree of

DOCTOR OF PHILOSOPHY

in the Department of Chemistry

Bottom-up generation of synthetic cells and tissues using microfluidic devices for double emulsion generation

by

Kaitlyn E. E. Ramsay

B.Sc. Hons., Queen's University, 2017

Supervisory Committee

Dr K. Elvira, Supervisor

(Department of Chemistry)

Dr L. Rosenberg, Departmental Member

(Department of Chemistry)

Dr M. Akbari, Outside Member

(Department of Mechanical Engineering)

ABSTRACT

Synthetic cells and tissues engineered from the bottom-up using non-living building blocks have many potential applications in medicine and biochemistry. Nonetheless, the applications of these synthetic cells and tissues remain limited by virtue of the challenging, costly, and uncontrollable methodologies available for their construction. Droplet microfluidic techniques, which are powerful analytical tools that can be used for the accurate and precise control over micro-sized droplets, offer potential solutions to these problems. The development of these droplet microfluidic platforms is a burgeoning and challenging field, with room for many impactful innovations. In the following dissertation, I first show the development of two different droplet microfluidic platform for the generation of two variations of synthetic cells: the first from polymeric-based building blocks and the second from biomimetic lipid-based building blocks. I then use the former of these platforms for the bottom-up generation of functional synthetic tissues (also known as prototissues). Using these techniques, I am able to elicit previously elusive structural and behavioral information. These methods contribute towards the creation of superior mimics of sophisticated life-like structures as well as a better understanding of how bespoke microfluidic platforms can be engineered to yield reliable and reproducible results. I have shown that microfluidic technologies are an invaluable tool for the creation and study of life-like systems and that these synthetic cells and tissues open up new avenues for research into multidisciplinary applications.

Contents

List of Figures

Figure 2.1 **Modular microcapillary platform for multicompartmental double emulsion formation**. a) Diagram of the assembled modular microcapillary platform for multicompartmental double emulsion formation. The platform is comprised of two junction boxes (Junction 1 and Junction 2) which are cast from a flexible resin using 3D printed moulds. They are used to link the capillaries together and seal them to prevent leakage. Junction box 1 holds the capillaries for the inner (red) and middle (yellow) phases. The inner capillary is inserted into the inlet of junction box 1, crosses both junction boxes and exits the outlet of junction box 2. The middle phase capillary is inserted into the outlet of junction box 1 and exits the outlet of junction box 2. The outer capillary (blue) is inserted into the outlet of junction box 2. The middle phase is inserted from the top of junction box 1 and the outer phase is inserted from the top of junction box 2. The three capillaries are different lengths to enable the formation of the inner droplets (red) in the middle phase (yellow), and then the outer droplets in the outer phase (blue) in the outer capillary. Diagram not to scale. b) One of the 3D printed moulds used to cast the junction boxes, which contains a projection designed to fit the required capillary. c) and d) Side and top views, respectively, of a junction box. The protrusion on the left allows the insertion of PTFE tubing or glass capillaries, and the protrusion on the top allows for the insertion of the middle and outer phases through a blunted metal syringe tip. e) Shows a front view of one of the protrusions though which a capillary is inserted into the junction box. The scale bar is constant for images b to e. f) Shows the assembled modular microcapillary platform configured for the formation

Figure 2.5 **Modular microcapillary platform for binary W/O/W multicompartmental double emulsion formation**. a) Diagram of the assembled modular microcapillary platform for binary W/O/W multicompartmental double emulsion formation. The platform is the same as in Figure 2.1a, except that two inner capillaries are inserted into each of the two holes in the inlet of Junction 1 to form the two types of inner droplets. Diagram not to scale. b) Diagram showing the composition of the modular microcapillary platform and of the binary multicompartmental droplets. For binary W/O/W multicompartmental double emulsion formation, the inner and middle capillaries were PTFE and the outer capillary was glass. The inner phases were water with SDS, the middle phase was FC-40 with PFO, and the outer phase was water with SDS. The inner phases were dyed for ease of visualisation. c-g) Microscopy images of the binary population of W/O/W bi-, tetra-, hexa-, octa- and deca-compartmental double emulsions generated with the modular microcapillary platform, where half of the inner droplets are red, and half are blue. h-l) Microscopy images of binary W/O/W tetra-compartmental double emulsions showing all possible combinations of inner droplets (4,0-, 3,1-, 2,2-, 1,3-, and 0,4-tetra-compartmental double emulsions respectively) generated with the modular microcapillary platform, where the number on the left denotes the number of blue droplets and the number on the right denotes the number of red droplets. m) Graph showing the accuracy of encapsulation as a function of the multicompartmental double emulsion composition (n = 30 for each droplet type). Error bars show the standard deviation. n) Droplet size analysis for each type of multicompartmental

ACKNOWLEDGEMENTS

First and foremost I'd like to thank my supervisor, Dr Katherine Elvira, without whom I couldn't have finished a Master's degree, much less my PhD. I came to her fledgling group in 2017 very lost, with crippling doubts and anxiety about my ability to do scientific research. Katherine showed me infinite patience and kindness. She lead by example, and put in a significant amount of time mentoring me. In my early days we met every week to go over my experimental plans. I am forever grateful that she took a gamble on me, and saw potential in me at moments when I didn't see it in myself. I'd also like to thank our collaborator, Dr Pierangelo Gobbo, whose excitement about the work we were doing together helped keep me motivated throughout.

I'd like to thank each of my fellow graduate student group members. First, Elanna Stephenson, who served as a confidant and research role-model. I will always respect her scientific brilliance and her ability to persevere through difficult moments that invariably come up in one's PhD. Next, Jaime Korner, whose steady confidence and determination is something I greatly admire and aspire towards. Though she has no apparent political ambitions, I expect she will somehow become the first female president of the United States. I must also thank Sean Farley, for though he is vegan, he is surprisingly fun to be around. He also single handedly saved our microcapillary project with his engineering skills. I'd also like to thank Alejandro Forigua. He's the little lab brother I never wanted, he's certainly irksome enough. That said, I care for him dearly, and would be remiss if I didn't say he was a great support during the difficult COVID months. I'd like to thank our newest member, postdoctoral fellow Dr Arash Dalili. Arash provided invaluable input and assistance on my work with liposomes and I look forward to working more with him in the future. Last but not

least I'd like to thank Alex McDonald (our newest graduate student) for being such a fun presence and for aggreeing to finish up the liposome project for me.

I'd also like to thank several chemistry department members. First to my good friends, Nicholas Richard (who kindly edited my introduction), Alivia Wang, Dr Alok Shaurya, Dr Arunova Maity, Diego Garcia, Alan Wei, Dr Harmen Zijlstra, Charlotte Dewar, Archita Adluri, Ankur Awasthi, Liza Silverman, Jin Yang, Chelsea Wilson, Dr Karol Valente, Dr Miller Crotti (and his beautiful family), Dr Isaac Omari, and the fabulous/ gorgeous Dr Roman Belli, who supported me emotionally and academically while I struggled in lab. There were also several notable staff members who provided guidance and input. Dr Stanislav Konorov, provided invaluable assistance to me with his fluorescent microscopy expertise. Dr Mathias Paul was a good friend and 3D printing expert who assisted me greatly in my early development of the microcapillary device and 3D printed wafer holder. Sean Adams, the Chemistry Department glassblower, was always incredibly helpful. He is also a great friend with whom I loved to have long chats. Dr Mohsen Akbari has taught me a lot about microfluidic science, both as my MECH 580 professor and as my committee member. He has also been very supportive of me in my pursuit of a career in medicine. Lastly, thanks to Dr Lisa Rosenberg, who is my committee member and was my CHEM 509 professor. She has always challenged me to be the best scientist I can be. She has also patiently provided numerous references for me, for which I am very grateful.

I'd also like to thank the friends in my personal life, Jenna Khamis (my bestie), Sara Khamis, Priyanka Rawat, Yelim Oh, Melissa Chong, (future medical Dr) Hardeep Kevin Gill, Dr Tatiana Popa, Katarina Laketic, Lindsey Frederiksen, Parmissa and Jaya Randhawa, Nathan Sanz, Dr Bibhuti Bhusan Rath, Dr Deepika Kandalya, Vani Verma, Dr Diana Mercado, Mohammad Alikamari, Juan Manuel Rueda Espinosa,

and Heidi Riek (plus her cutie pup Nutmeg). They have been greatly supportive and encouraged work-life balance.

I have a long list of undergraduate students to thank as well, as every one of them was remarkable, and a pleasure to supervise. In particular, I'd like to thank Kate Hammond, my first friend, Jae Levy, for their kooky genius, Ricardo Ramírez, for his steady dependability, Pooja Hariharan, for her work ethic and kindness, Katie Stagg, for her love of puppies and funny anecdotes, Jaling Kersen, who is definitely one of the coolest and most adventurous people I've ever met, and, lastly, Maria Hangad, who is (for better or worse) like a younger version of me in many ways.

Most importantly, I'd like to thank my family. First, my Mum, who has always been there for me through both good and bad times. She's the strongest person I know, and is someone who I aspire to be like. Next, my Dad, who I don't have to aspire to be like because I am already exactly like him (I got my good looks, genius, and great sense of humor from him). I'd also like to thank my partner, Dr Anuj Joshi (and his family), who provided a constant sense of daily support. Anuj is in stark contrast to me in many ways; he can always seem find the bright side to any situation. Without him, I doubt I could have stuck out the ups and downs of grad school. Anuj also did several top-to-bottom proofreads of my thesis. He used his editing superpowers to bail me out (I am also, admittedly, quite impatient while I write). My sweet pets, Monty, Balok, Tribble and Barney, also deserve heartfelt gratitude for their cuteness and constant source of love. I'd also like to thank my siblings, Lili (the funny one) and Kenna (the smart one). They supplied me with memes, sassy comments, and funny artwork which made the day to day stresses of graduate school bearable. I'd like to thank my grandparents, Edward and Bonnie Brown, who have always believed in and loved me unconditionally. Lastly, I'd like to thank my extended family as I

am close with each and every one of them. Aunt Laurie and Uncle Jaesun for their career advice and support, Uncle Andrew and Aunt Michelle for their fun stories, Aunt Kathy for the massages/ fashion advice, Uncle Micheal and Aunt Camille for the love and fun games (and guinea pigs/ puppies), Uncle Paul for the good books, Uncle Jaime for the good movies, and Aunt Norah for always checking in on me. I also have a long list of cousins (Molly Brown, Dylan Brown, Brendan Suh, Maegan Suh, Eddie Northcott, Charlie Northcott, Adam Ramsay, Will Ramsay, Margaret Ramsay, Catherine Ramsay, Sarah Ramsay and David Ramsay), each of whom has been a constant fun presence throughout my life.

"Invention, it must be humbly admitted, does not consist in creating out of void, but out of chaos; the materials must, in the first place, be afforded: it can give form to dark, shapeless substances, but cannot bring into being the substance itself. [...] Invention consists in the capacity of seizing on the capabilities of a subject, and in the power of moulding and fashioning ideas suggested to it."

Mary Shelley

DEDICATION

I have only accomplished what I have so far due to the support and patience of my close family (Mom, Dad, Liam, Kenna, Barney, Monty, Anuj, and Balok)*.

**Arranged in chronological order of encounter, not preference. Specified because each of them are drama queens and complained about the order in which they were named...*

Chapter 1

Introduction

The following dissertation details the fabrication of synthetic cell and tissue-like entities from non-living building blocks. Droplet microfluidic technologies were used in order to precisely control the complex construction parameters. This research was conducted in order to address emerging challenges in bio-inspired engineering for use in medicine and biochemical research.

1.1 Microfluidic technologies and droplets

Microfluidic science is defined broadly as the processing or manipulation of small (in the range of 10^{-9} to 10^{-18} liters) volumes of fluids that are geometrically constrained to a small scale (tens to hundreds of micrometers in size).[1] The small size of microfluidic devices, as well as the low volumes of the fluids they hold, poses several notable advantages over conventionally sized systems. This includes less reagent usage and cost, as well as an increased ease in portability, experimental control and analytical throughput. In order to fall within a microfluidic regime, the Reynolds

number (a unitless value which describes the ratio between the inertial and viscous forces in fluids) must generally be smaller than 10^2.[2] Fluids behave counter-intuitively on the microfluidic scale. Microfluidic regimes result in a prevalence of laminar over turbulent flow; by consequence, mixing of reagents occurs mainly *via* diffusion. Factors such as energy dissipation, surface tension, and fluidic resistance also begin to dominate due to the high surface to volume ratio.[1]

Droplet microfluidics is a specific branch of microfludic science. It involves the manipulation of discrete volumes of fluids in immiscible phases.[3,4] In droplet microfludics, the continuous phase is the medium through which the droplets flow and the dispersed phase refers to the phase being broken up into droplets[3,4] (Figure 1.1a). The size of the generated droplets is controlled by the flow rate ratio of the continuous to the dispersed phase, the interfacial tension, and the geometry of the channels.[3,4] Droplets can be formed both actively and passively.[5] Active droplet formation requires an external energy input (magnetic, electric, centrifugal) for droplet generation. Passive droplet formation requires no additional energy input and is advantageous because it often produces similar results to active droplet formation but with simpler device designs. In passive droplet formation, the continuous phase flow rate is typically higher than the dispersed phase flow rate. At the end of the dispersed phase channel, the fluid is strained until it breaks due to shear forces and forms droplets.[5] The work outlined in my dissertation only makes use of passive droplet formation strategies.

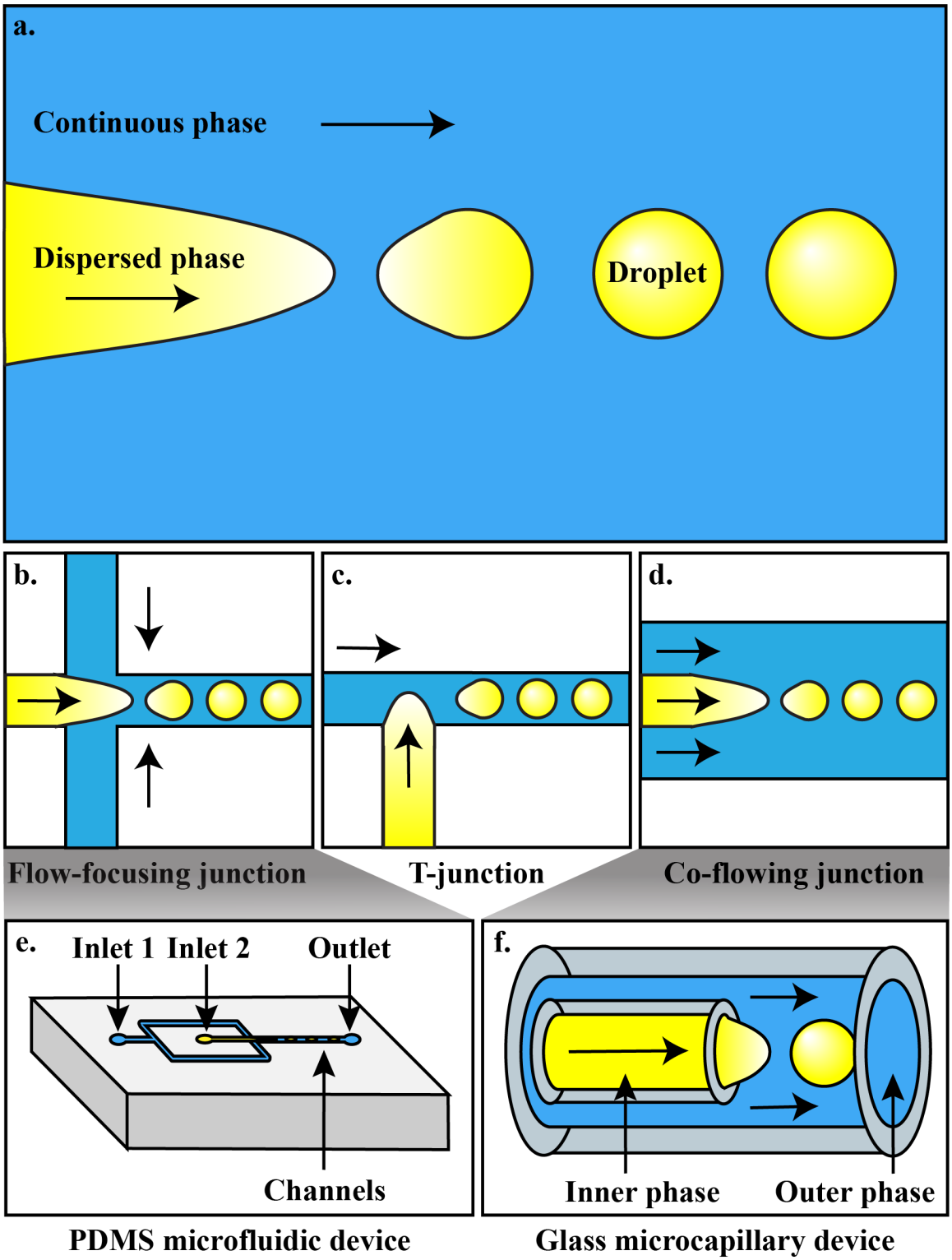

Figure 1.1: **Introduction to microfluidic technology.** Yellow represents a disperse oil phase and blue represents a continuous aqueous phase. Arrows show the direction of fluid flow. a, The fundamentals of droplet formation with labels denoting the continuous and dispersed phases and the direction of fluid flow. b, Droplet formation in a flow focusing junction. c, Droplet formation in a T-junction. d, Droplet formation in a co-flowing junction. e, An example of a flow focusing PDMS microfluidic platform with moulded microchannels capable of droplet formation. f, An example of glass microcapillaries in a co-flowing alignment capable of droplet formation.

There are three main microfluidic geometries used for passive droplet formation. Figure 1.1b and e illustrate the flow-focusing microfluidic geometry[5]. In a flow focusing junction, the continuous phase flows from two sides (typically at an angle) to meet the dispersed phase, which then subsequently undergoes a shear-force that creates a droplet. This force is most often generated *via* a narrowing in the channel, which generates symmetric shearing, followed by a channel of greater or equal width, which forms a droplet. T-junctions involve the continuous and dispersed phases meeting each other at a 90° angle to each other (Figure 1.1c). The dispersed phase extends into the continuous phase until it is stretched, and shear-forces break off a droplet. A co-flowing junction is a 3D version of flow focusing junction in which the dispersed phase channel is three-dimensionally enclosed inside a continuous phase channel (Figure 1.1d and f).

In addition to the different droplet formation geometries, the material composing the microfluidic device ensures the consistency and stability of the droplets formed. As shown in Figure 1.1e-f, there are two materials which are most commonly used for droplet formation.[3] Polydimethylsiloxane (PDMS) devices are generally made using conventional soft lithography, which involves replicating structures using elastomeric materials and moulds.[3] From these moulds, micro-channels (where fluids flow through) can be accessed by biopsy punching inlets (where fluids enter) and outlets (where fluids exit) into the PDMS. A schematic example of a flow-focusing PDMS device is shown in Figure 1.1e. PDMS is an useful material for droplet microfluidics as it is relatively inexpensive, easily moulded and bonded, and transparent to visible light. That said, PDMS is not without its drawbacks. Its porosity results in a lack of stability in the presence of organic solvents (like chloroform or hexanes) and damaging changes to the microfluidic channels such as swelling and deformation may occur. PDMS is also not fully compatible with some biological materials, such as

proteins, as they often adhere to the channels and impede stable droplet formation. PDMS is also inherently hydrophobic, which is undesirable when forming oil droplets since they will stick to the sides of the channel. There are several PDMS surface treatment protocols available to mitigate these issues, but there are instances where more stable droplet formation can be achieved with more solvent resistant materials such as glass. Glass is inherently more hydrophillic than PDMS, which is good for oil droplet formation.[3] It can also easily be surface treated for aqueous droplet formation. Glass is transparent to visible light which allows for easy droplet visualization. It is also generally more stable in the presence of organic solvents. Figure 1.1f shows a schematic example of glass microcapillaries (micro-sized capillaries) in a co-flow alignment. Droplet formation of the inner (yellow) phase is shown upon encapsulation by the outer (blue) phase. On the downside, glass microcapillary devices are often more challenging and costly to put together due to their complexity and fragility.

There are two main motivations for creating microfluidic droplets over macro-scale droplets (Figure 1.2). The first motivation is precise compartmentalization. Microfluidic droplet formation offers a method to manipulate very small and precise volumes of samples. It also provides a way of accurately encapsulating biological or chemical components in a high throughput (experimental automation such that large scale repetition become feasible) manner. The second motivation is to generate droplets with a very high monodispersity (a coefficient of variation of particle size distribution must be less than 10% to be considered monodisperse).[6] This is contrary to conventional batch methods for droplet production such as mixing or centrifugation, which results in polydisperse droplets.[3] With these two motivations in mind, microfludic technologies have the potential to benefit material science and the food and pharmaceutical industries.[3]

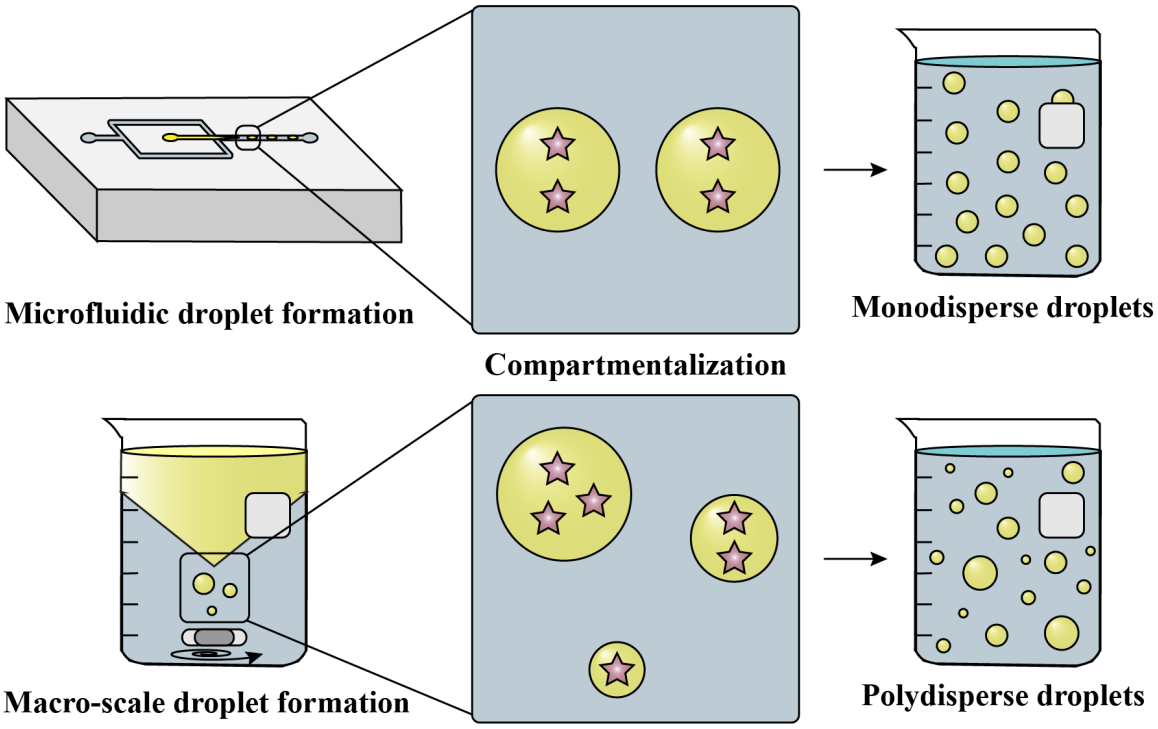

Figure 1.2: **Motivation for microfluidic technology.** Schematic showing a comparison between microfluidic droplet formation from a flow focusing device and macro-scale droplet formation from mixing with a stir-bar in a beaker. Light blue indicates the aqueous phase and the yellow circles indicate the oil droplets. Pink stars indicate arbitrary components (for example DNA, RNA, proteins, droplets...etc.) which are being encapsulated into droplets by the oil phase. Microfluidic droplet formation results in more precise and accurate encapsulation efficiency as well as monodisperse droplets. Macro-scale droplet formation results in lower encapsulation precision and accuracy as well as polydisperse droplets.

1.2 Microfludic technologies for double emulsion generation

The term emulsion is a general term which refers to a fine dispersion of droplets that includes two (or more) immiscible fluid phases (Figure 1.3a-d). The most common immiscible fluid phases used are water (or aqueous) and oil.[7] Emulsions can be classified as water-in-oil emulsions (i.e. water droplets in a bulk oil phase, denoted W/O [Figure 1.3a]) or oil-in-water emulsions (i.e. oil droplets in a bulk water phase, denoted O/W [Figure 1.3b]). The term multiple emulsion indicates that there are several layers of fluids in each droplet.[8] Multiple emulsions have been exploited in many applications, specifically in evolutionary biology,[9,10] food sciences,[11] cosmetics,[12] and medicine,[13]

among others, as they can incorporate an added layer of control and complexity. The double emulsion is a specific subclass of multiple emulsion in which only two liquids are separated by a third liquid which is not miscible. For double emulsions, the fluid which forms the inner droplet is termed the inner phase, the fluid which forms the encapsulating droplet is termed the middle phase, and the fluid which surrounds the resulting double emulsion is termed the outer phase. The two principle versions of double emulsions are oil-in-water-in-oil emulsions (i.e. oil droplets in water droplets in a bulk oil phase, denoted O/W/O [Figure 1.3c]) and water-in-oil-in-water double emulsions (i.e. water droplets in oil droplets in a bulk water phase, denoted W/O/W [Figure 1.3d]). There are also several other iterations possible for immiscible like-phases (such as oil-in-oil-in-water, denoted O/O/W, which will be detailed in Chapter 2).

As double emulsions become more complex, so too does their nomenclature. Double emulsions which contain several inner phase droplets are often termed "multi-compartmental" double emulsion droplets.[14–16] Naming becomes more complicated when there is more than one inner droplet phenotype. As there is no clear procedure for specifying double emulsion composition present in the literature, I have come up with my own protocol as highlighted in Figure 1.3e-m. As I will discuss in detail in Chapter 5, in order to denote the total inner droplet composition of the double emulsion, a multiplying affix is used. A multicompartmental double emulsion which contains a single droplet is termed a mono-compartmental double emulsion (1.3e), one containing two droplets is termed a bi-compartmental double emulsion (1.3f), one containing three droplets is termed a tri-compartmental double emulsion (1.3g), one containing four droplets is termed a tetra-compartmental double emulsion (1.3h), and so on. In order to specify the droplet type for each of the inner droplets, two numerical prefixes are added, an example is illustrated in Figure 1.3i-m with tetra-

compartmental double emulsions. The first numerical prefix denotes the number of phenotype 1 (shown as dark blue in Figure 1.3i-m) inner droplets and the second number denotes the number of phenotype 2 (shown as red in Figure 1.3i-m) inner droplets. For example, a tetra-compartmental double emulsion with one blue droplet and three red inner droplets is a 1,3-tetra-compartmental double emulsion. Hence, Figure 1.3i-m shows 4,0-, 3,1-, 2,2-, 1,3- and 0,4-tetra-compartmental double emulsions respectively.

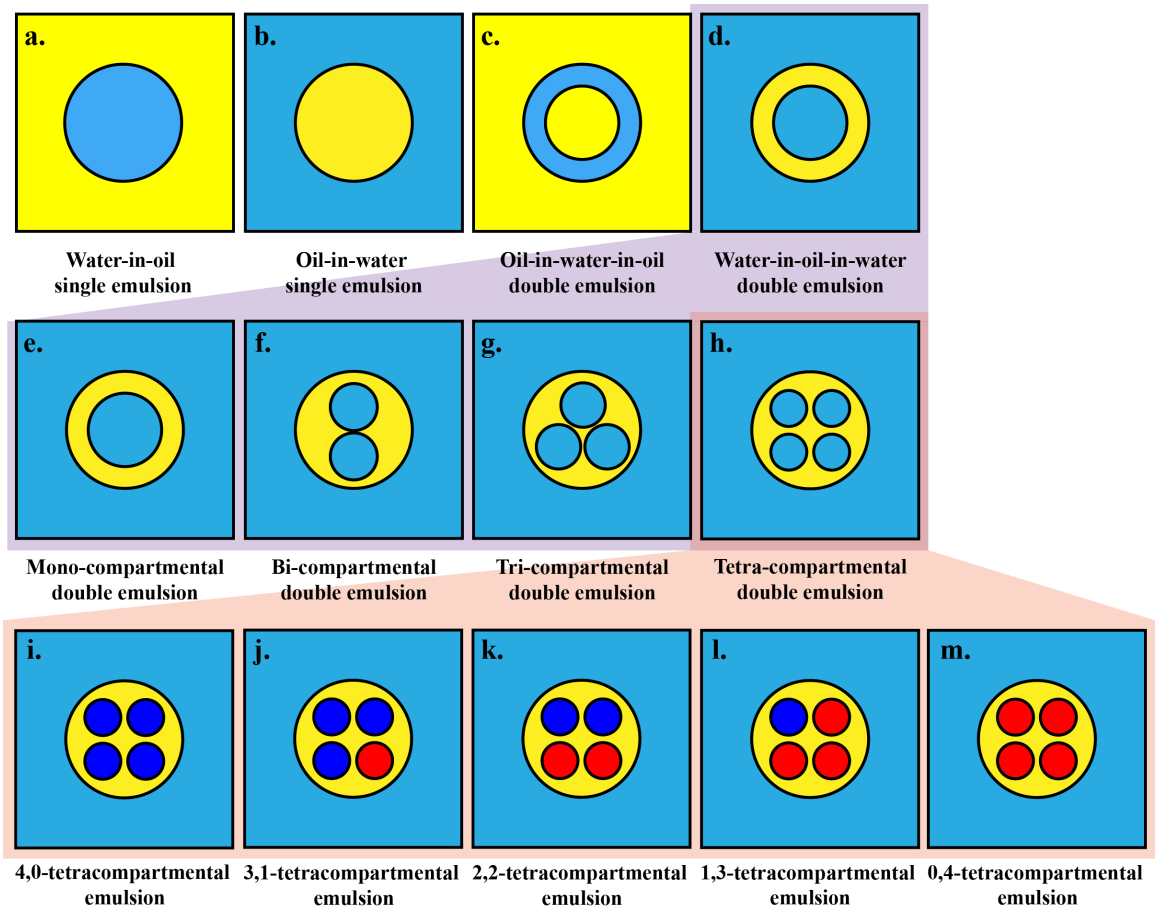

Figure 1.3: **Double emulsion nomenclature.** Light blue denotes water and yellow denotes oil a, Water-in-oil emulsion droplet. b, Oil-in-water emulsion droplet. c, Oil-in-water-in-oil double emulsion droplet. d, Water-in-oil-in-water double emulsion droplet. e, Mono-compartmental double emulsion droplet. f, Bi-compartmental double emulsion droplet. g, Tri-compartmental double emulsion droplet. h, Tetra-compartmental double emulsion droplet. i-m, Dark blue and red denote aqueous droplets of different phenotypes. Images represent 4,0-, 3,1-, 2,2-, 1,3- and 0,4-tetra-compartmental double emulsion droplets.

There are two main approaches used to generate microfluidic double emulsion droplets:

one- and two-step emulsification.[2,8,17,18] Both techniques involve the use of two sets of emulsifiers. In the case of a W/O/W double emulsion, there would be a hydrophobic emulsifier, which is designed to stabilize the interface of the W/O internal emulsion, and a hydrophilic emulsifier, which is designed to stabilize the interface of an O/W emulsion. The composition of the double emulsion plays a vital role. The properties and concentration of the fluids, as well as the different surfactants, significantly impact the emulsion stability. It is well established that the inner hydrophobic emulsifiers must be used at high concentrations whereas the hydrophilic emulsifiers are used in low concentration in order to best maintain stability. In a one-step emulsification, the W/O emulsion uses a single mixing step in which the water phase is continuously added into the oil phase (which contains the surfactant blend) via catastrophic inversions and under continuous agitation. Afterwards, the added phase is dispersed, as the droplet population increases until phase flipping occurs. Though simple and more rapid, the one-step emulsification protocol does not generally offer as high a level of control as two-step emulsification. In two-step emulsification, the first set of W/O emulsions are formed under high shear conditions. When done without the use of microfluidic techniques, the secondary emulsification is normally carried out without shear force as this would disrupt the already formed primary emulsions. With microfluidic double emulsions however, shear force can be used a second time to generate a monodisperse population of double emulsions. This technology allows for access to the control and high throughput advantages of two-step emulsification without resulting in unintended polydispersity.

1.3 Synthetic cells

Synthetic cells are compartmentalized entities which have the minimum requirements for some life-like functionalities. The concept of synthetic cells was initially introduced in the 1960s by Thomas Chang.[19] Chang focused his efforts on the bottom-up engineering of a semipermeable membrane which allowed the diffusion of small molecules such as proteins, enzymes, and hemoglobin, among others, into and out of the synthetic cell. Since then, there has been an explosive interest worldwide in synthetic cells.[20] Synthetic cells have applications in a wide variety of fields such as medicine,[10,21–23] catalytic reactions,[24,25] and protein synthesis.[26,27] Synthetic cells are most often synthesized using bottom-up engineering, which proposes that a cell-like entity can be built from simple, non-living, components. The cell membrane, which acts to separate the interior of all cells from the outside environment, is most often the starting point in the bottom-up engineering of synthetic cells.[17] The two most common synthetic cell membrane constructs are either polymeric or lipid-based.[17].

1.3.1 Polymeric-based synthetic cells

The use of non-biological materials in bottom-up synthetic biology tries to bridge the gap between biology and chemistry, and aims to help us better understand the boundaries between living and non-living matter. Polymeric-based synthetic cells use materials which are engineered to mimic one or more features of biological cells.[28] There are no restrictions on the types of materials, methods, or chemical reactions that can be used to build this genre of synthetic cell.[28] In recent history, a series of different polymeric synthetic cells have been synthesized based on polymersomes, which are amphiphilic synthetic block co-polymers that form synthetic cell membranes;[29,30] dendrimersomes, which are self-assembled from amphiphilic Janus (two-faced) den-

drimers (highly branched, star-shaped macromolecules);[31] coacervates, which are colloid (homogeneous noncrystalline substance made of large molecules or microscopic particles of one substance dispersed through a second substance)-rich viscous liquid phase microdroplets;[32,33] proteinosomes, which are semi-permeable elastic membranes which is made up of a closely packed monolayer of interconnected protein–polymer building blocks;[28,34,35] and inorganic colloidosomes, which are colloids made from only inorganic materials.[36–38]

There are a few examples of polymeric synthetic cells created using microfluidic devices.[17] Martino *et al.* used a glass microcapillary device for polyethylene glycol-b-polylactic acid (PEG-b-PLA) polymersome production. They used double emulsions which consisted of an aqueous droplet surrounded by a shell of PEG-b-PLA diblock copolymer dissolved in toluene/chloroform. These solvents then underwent a de-wetting transition, leaving behind a polymersome with a unilamellar (singular) bilayer.[39] Kim *et al.* also used a glass microcapillary device to generate polyethylene PEG-b-PLA polymersomes. The marked difference is that Kim *et al.* encapsulated multiple compartments within their double emulsions. These more complex "double polymerosomes" were capable of controlled and sequential dissociation in a programmed fashion. Though an important step forward in the field of polymeric synthetic cells, these publications are limited by the fact that they use glass microcapillary devices which, as mentioned previously, are generally time consuming, challenging, and costly to assemble. As an alternative, there are two recent examples of polymeric synthetic cells which are generated using PDMS microfluidic devices. Thiele *et al.*, described the formation of polymersomes from double emulsions stabilized with co-polymer using a PDMS microfluidic device.[40] In the same vein, Ugrinic *et al.* used a PDMS microfluidic device to generate proteinosome microdroplets which were comprised of BSA and glucose oxidase conjugated to poly(N-

isopropylacrylamide) (PNIPAAm) chains.[41] Though the above-mentioned work is a promising first step, the researchers did not incorporate more complex life-like functionalities such as the ability to interconnect or communicate between cells.

There are both assets and drawbacks to using non-biological building blocks in the generation of synthetic cells. On one hand, use of non-biological building blocks removes the limitations of working with lipids and proteins such as their tendency to degrade over time as well as their requisite biomimeticity, which can be a limiting factor in the genre of components which can be used for their construction.[28] On the other hand, working with non-biological material has the potential to limit the medical applications of these synthetic cells due to a lack in bio-compatibility.

1.3.2 Lipid-based synthetic cells

The most popular synthetic cell membrane construct is lipid-based.[17] As opposed to polymeric-based synthetic cells, this genre of synthetic cell is limited to strictly biological building blocks. A positive consequence of this limitation is that lipid-based synthetic cells are often more bio-mimetic. Cell membranes consist of two flat sheets of phospholipid molecules, known as a lipid bilayer. As shown in Figure 1.4, there are three main structures that phospholipids bilayers form in solution.[42] The liposomal structure is that which most closely resembles living cells found living *in vivo*.

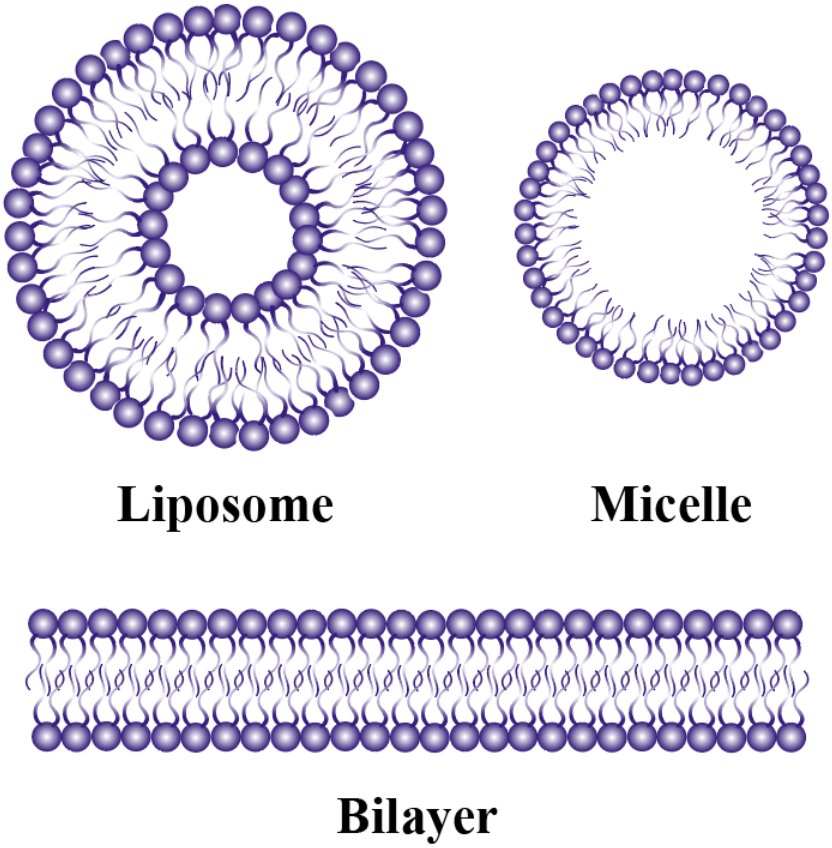

Figure 1.4: **Types of model lipid membranes.** Illustration of the three main types of lipid assemblies: liposomes (a spherical double layer of lipids), micelles (a spherical single layer of lipids) and a bilayer sheet (a planar sheet consisting of a double layer of lipids).

Liposomes consist of two spheres of phospholipid molecules, as shown in Figure 1.5a. The phospholipid molecules contain hydrophillic heads and hydrophobic tails which result in an energetically favorable bilayer formation when exposed to an aqueous solution.[43] In most cells *in vivo*, the inner and outer leaflets differ in terms of phospholipid composition (Figure 1.5b). The red blood cell is a notable example of a cell with an asymmetric bilayer that is involved in important physiological functioning.[44] Lipid asymmetry arises since many phospholipids are synthesized and inserted initially into the inner monolayer. Those that make up the outer layer are then transported from the inner layer by enzymes called flippases.[44] Liposomes were first artificially syn-

thesized in the late 1960s[45] and are highly useful for a wide range of applications. They have become a standard tool as drugs development or delivery platforms drug delivery due to their inherent biomimeticity.[43] Most notably, liposomes are useful as synthetic cell models as they can be composed of, and surrounded by, much simpler elements than *in vivo* cells.[17,46–48]

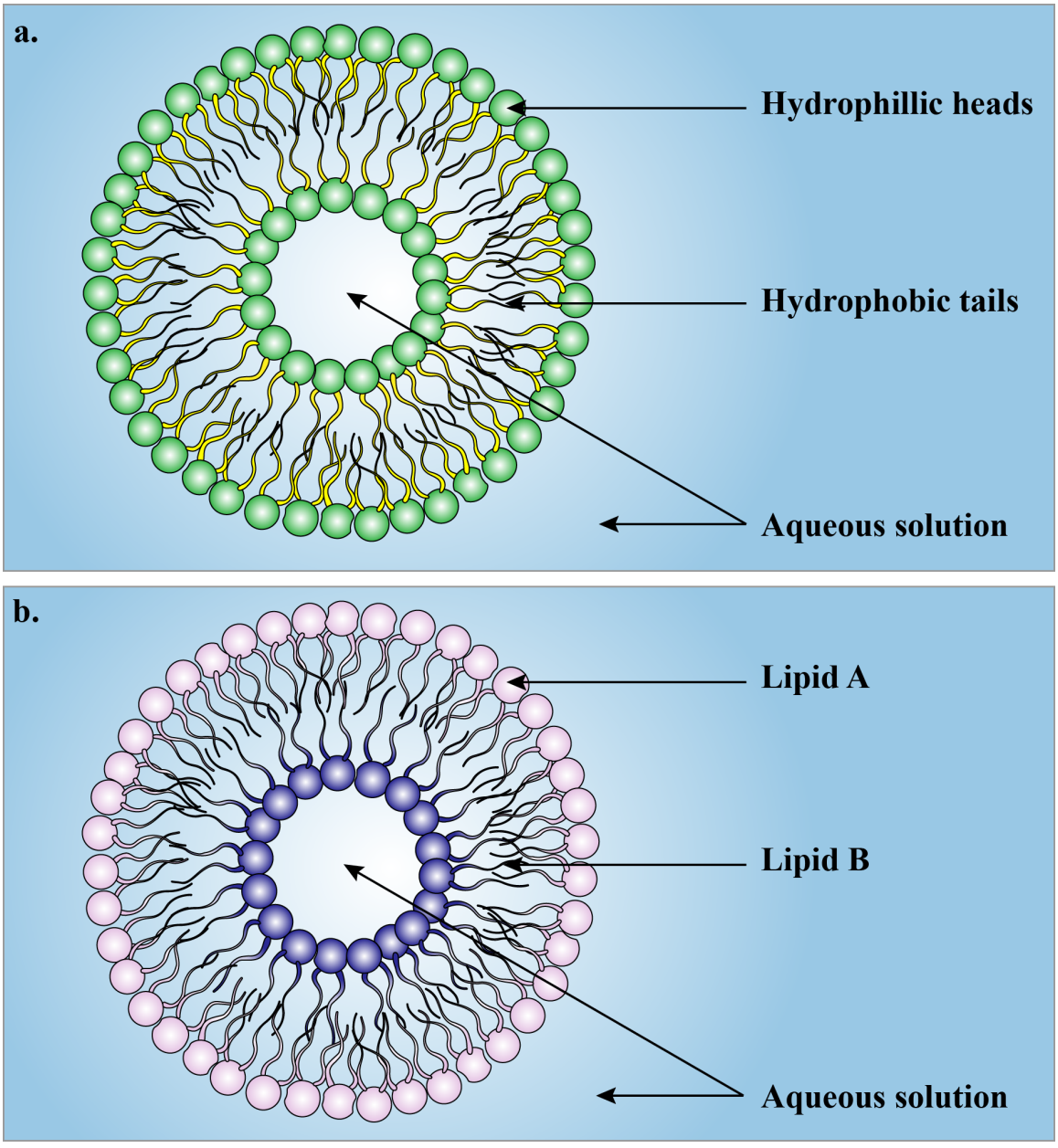

Figure 1.5: **Schematic of liposomes.** a, A symmetric liposome formed from phospholipids in an aqueous solution. b, An asymmetric liposome with Lipid A and B arbitrarily denoting the different lipid types

Despite their many advantages, conventional methods for synthesizing liposomes, such as electroformation,[49] extrusion,[50] reverse phase evaporation,[51] freeze-drying,[52] droplet emulsion transfer,[53] and hydration/swelling,[54] often result in low yields of polydisperse liposomes with inefficient component encapsulation (such DNA, RNA, proteins, droplets...etc.).[55] When liposomal asymmetry is the desired outcome, matters are even more complicated. Lipid asymmetry can be most easily mimicked in the lab using model planar bilayer systems.[44] It has been shown in the literature that it is possible to synthesize asymmetric planar bilayers by utilizing two different monolayers in Langmuir-Blodgett deposition[56] or a combination of Langmuir-Blodgett and vesicle rupture deposition.[57] That said, these techniques are labour intensive, require a high level of expertise and cannot result in liposomes, which are the more biomimetic form that lipids take in solution. Microfluidic devices have also been shown to be able to generate asymmetric liposomes; this will be elaborated upon later in Chapter 4.

The use of microfluidic technologies for symmetric liposome formation allows for a significantly greater level of control and mitigates the disadvantages associated with conventional liposome fabrication methods. There are two main routes to generate uniform liposomes using microfluidic devices: either single W/O emulsification,[58–61] or double W/O/W emulsification.[62–67] For the single emulsification method, the W/O emulsions are made on-chip and are subsequently transferred to an aqueous phase on-chip *via* micro-channels in order to yield liposomes.[55,58–61] Though relatively simple, the W/O emulsion route is often low-yielding, as most lipid droplets burst when transferred to the second aqueous phase. The other approach involves the use of double emulsions which can be generated using pulsed jetting,[65,66] fluid shearing,[62–64] or transient membrane ejection techniques.[67] These techniques will be described in more detail in the introduction to Chapter 4. The double emulsification approach is

known to more often generate high yields of mono-disperse liposomes.[55] That said, these three strategies often require a complex device design with delicate operating conditions and generate liposomes which contain residual oil within the lipid membranes.[64,65]

1.4 Synthetic tissues

Though there has been an explosion of research into the area of synthetic cells within the past 50 years,[20] the next natural step in biomedical engineering, the synthetic tissue, remains woefully understudied. It is only in the past ten years that the study into synthetic tissues began in earnest. Though there are many detailed reviews on synthetic cells to date,[68–72] there are few comprehensive reviews on synthetic tissues. Recently, there have been a handful of perspectives (which are different from reviews in that they are more speculative and often provide suggestions/ opinions) written on synthetic tissues.[28,73,74] Our collaborator, Dr Pierangelo Gobbo, focused his 2020 perspective on the materials approach, but did not delve too deeply into the biomimetic side of synthetic tissues.[28] Bailey *et al.* emphasized droplet interface bilayers (DIBs) in his own 2019 review on synthetic tissues but did not fully evaluate some of the recent polymeric-based synthetic tissue approaches.[73] Lastly, an opinion piece by Gonzales *et al.* focused mainly on summarising recent developments for the spatial localisation of microcompartments rather than evaluating their functionality as synthetic tissues.[74] Here I address some of the gaps in the literature and provide a detailed review of the theoretical and methodological contributions to the field of bottom-up synthetic tissue fabrication as it stands today. More specifically, I will be reviewing the most promising methods used in the development of synthetic tissues as well as some of the exciting new fields to which these synthetic tissues may be

applied.

The term "tissue" is generally used to describe a grouping of cells which are found in close proximity in the body, perform a specific function, and share a common embryonic origin.[75] Recent approaches in the field of synthetic tissues generally seek to mimic one, or several, of these qualities. For the purposes of this dissertation, synthetic tissues are made up of synthetic cells (as opposed to living cells). There are generally four goals for researchers in the field of synthetic tissue. The first is that a synthetic tissue must be made up of synthetic (non-living) cells, which are defined as compartmentalized units that contain a membrane which separates the inside of the cell from the outside environment. The second is that the synthetic cells which make up a synthetic tissue must be interconnected in a manner which allows life-like functionality. It bears noting that when we refer to "interconnection" in the field of synthetic cells and tissues we are referring to either the protein-protein or click chemistry (alkyne, azide or alkyne-azide) interactions between synthetic cells. As an extension of this, the third goal is that the synthetic cells must be able to communicate with each other. In nature, communication can be in multiple forms such as electrical, enzymatic, light, and touch-based communication. Lastly, and most importantly, these synthetic tissues should be able to behave in a coordinated manner which belies some sort of life-like functionality (such as contraction). Here I summarize the most salient examples of these types of synthetic tissues to date, as well as some of the more notable steps that have been taken towards the generation of these tissues.

Due, in part, to the novelty of the field, there are several confounding uses of the terms "synthetic cells" and "synthetic tissues" in the literature. A cursory search of these terms will yield a myriad of publications which focus on the biomedical engineering

of synthetic tissues from living cells. Though significant and impactful advancements have been made in this area, for the purposes of this review of the literature I will be excluding this particular genre of synthetic tissue and will only be considering those which have been built from the bottom-up from non-living building blocks. There are also other terms used interchangeably with synthetic cells and synthetic tissues, such as "protocells" and "prototissues". Protocells are thought of as being the first form of life on earth, billions of years ago. They are broadly defined as structures which are formed from the aggregation of abiotic components which display life-like characteristics.[28] These terms tend generally to be used when the goal of the work is to mimic primitive life-like functionality rather than to achieve biomimicry. Other terms that are often used in the literature are "artificial cell" or "artificial tissue", which are also broadly used to describe tissues built from living cells.[76,77] Again, I disclude this genre of tissue from the following review. For ease of reading, I will be using the terms "synthetic cells" and "synthetic tissues" throughout this introduction as well as in chapters 4. In chapters 3 and 5 I use the terms "protocell" and "prototissues" as the purpose of the work in these chapters was to mimic primitive life-like functionality rather than to achieve biomimicry.

1.4.1 Polymeric-based synthetic tissues

A polymeric-based synthetic cell is comprised of an inert plastic polymer in combination with non-living biological molecules (i.e. proteins, lipids... etc.). In comparison with a lipid-based membranes, polymeric-based membranes are not explicitly designed with *in vivo* cell-likeness in mind. That said, the use of a polymeric membrane in synthetic cells poses several advantages, namely that they are often more stable and life-like functions are more easily incorporated, as they are not limited by the materials that can be used. The following studies are the only two examples to date

of synthetic tissues which are made from polymeric-based synthetic cells.

The first example was published by Gobbo *et al.* in 2018.[78] They described the programmed assembly of spatially integrated prototissues made from a binary community of bio-orthogonally linked BSA-nanoconjugate proteinosomes. The researchers synthesized two types of thermally responsive protein-polymer nanoconjugates with either a strained alkyne or pendant azide functional group. They used these amphiphilic BSA-nanoconjugates to prepare two distinct populations of bio-orthogonally reactive proteinosomes which could be interconnected using click chemistry to form prototissues. These prototissues (shown in Figure 1.6) are capable of collective thermoresponsive behaviors, mechanochemical transduction and enzymatically modulated reversible contraction. These behaviors stem from a coordinated interaction between multiple chemically coupled proteinosomes. This work provided the first example of synthetic polymeric tissues which were stable in water (which is better mimic of true biological systems). As a step further, their systems were able to behave in a life-like manner when subjected to temperature changes as well as demonstrate rudimentary communication between the synthetic cells which make up the tissue. Though promising, the methods used by these researchers are disadvantaged by two principle limitations: they afford limited control over the prototissue structure and they offer poor reproducibility.

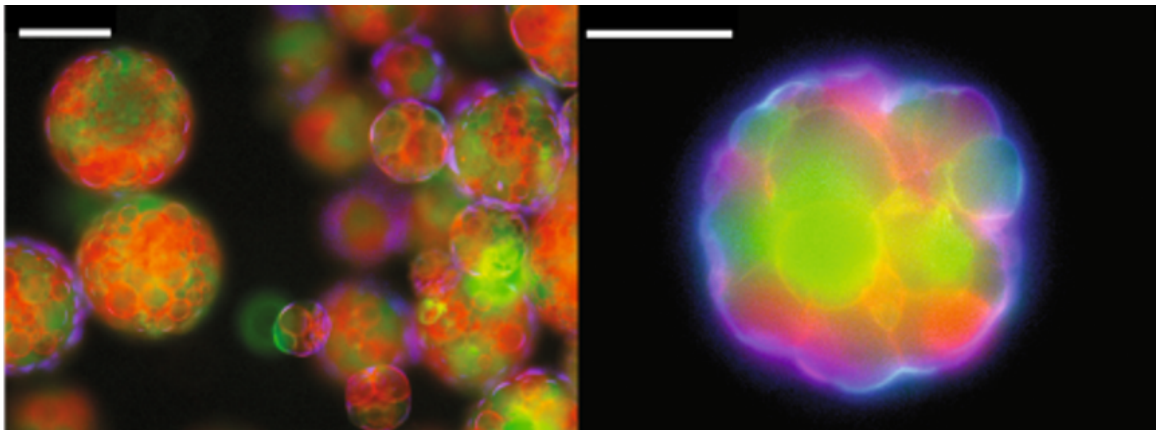

Figure 1.6: **Programmed assembly of proteinosomes into synthetic prototissue spheroids**. Prototissue spheroids consisting of a spatially interlinked network of bio-orthogonally ligated crosslinked proteinosomes (red and green) encased in a non-bio-orthogonally crosslinked proteinosome membrane (blue). Scale bar is 100 μm. Image reproduced from Gobbo *et al.*[78] with permission.

More recently Zhu *et al.* published work highlighting the multilevel compartmentalization of aqueous colloidosomes *via* interfacial aqueous-phase separation (separation of immiscible phases) (Figure 1.7).[79] They designed a method which allowed for the rapid multilevel compartmentalization of aqueous droplets. These synthetic multicellular structures were termed "blastosomes" since they are similar to blastula (a stage in embryonic development) in appearance. The rapid assembly of these particles resulted in biomimetic non-equilibrium shapes of water which is an accurate mimic for life-like behaviour. That said, these polymeric synthetic tissues suffer from the same disadvantages as the methodology used by Gobbo *et al.*, in that the researchers had no control over the composition of their synthetic tissues which results in poor reproducibility tissue-to-tissue.

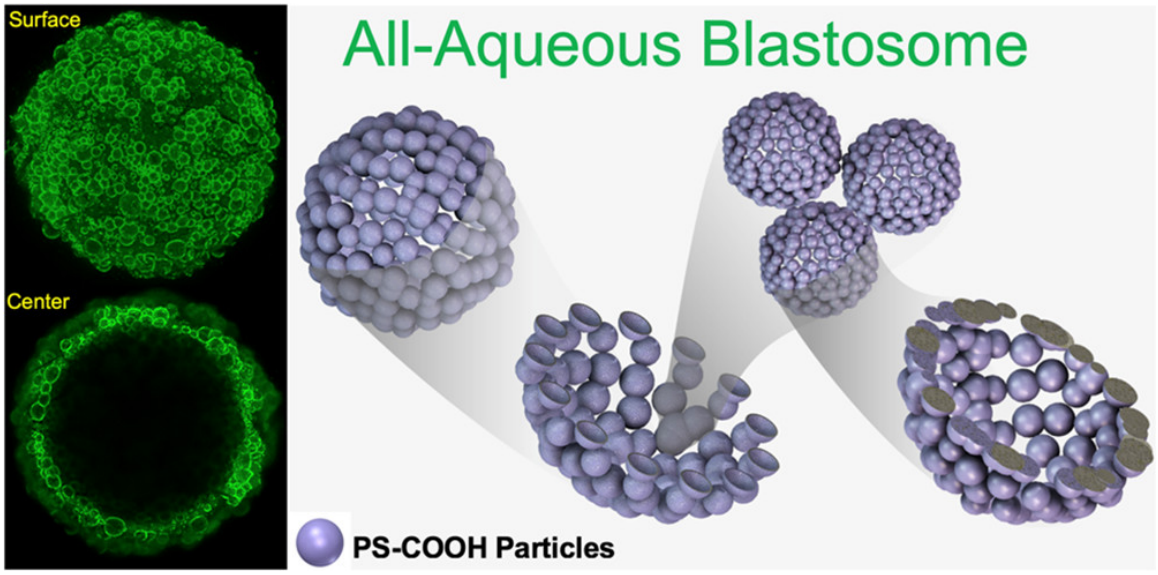

Figure 1.7: **All-aqueous membranous colloidosomes in aqueous two-phase systems.** Image reproduced from Zhu *et al.*[79] with permission.

1.4.2 Lipid-based synthetic tissues

The more biomimetic genre of synthetic tissue is built from lipid-based synthetic cells. The following work is inspired by the constitution of naturally occurring cell membranes to built synthetic tissues.

1.4.2.1 Liposomes

As liposomes are the most popular foundations for synthetic cells, it follows that they are also the most popular functional unit for synthetic tissues. Synthetic tissues are generally made up from giant unilamellar vesicles (GUVs), which are liposomes that contain a single bilayer and have a size range of 1-200 μm (the term vesicle refers to a self-contained structure which is enclosed by a lipid bilayer).[48]

One of the earliest examples of a tissue-like material involved the formation of geometrically complex lipid-based nanotube-vesicle networks with higher-order topologies.[80] As can be seen in Figure 1.8a, the researchers developed a microelectrofusion method

to construct fluid-state GUV networks which were capable of significant geometric complexity. The membranes of their GUVs were penetrated with nanotubes using a combination of mechanical force and anodic electric pulses. Interestingly, the formation of their nanotube networks was shown to follow a minimum-bending energy algorithm which solved a pathway minimization: this meant that their tissue-like aggregates could be programmed (Figure 1.8b). In addition, this electrofusion method even allowed for the integration of biological cells into the lipid nanotube-vesicle networks. This work was one of the first examples of interconnecting synthetic cell-like entities. That said, these networks were limited in their ability to perform life-like functions and hence are not full synthetic tissues.

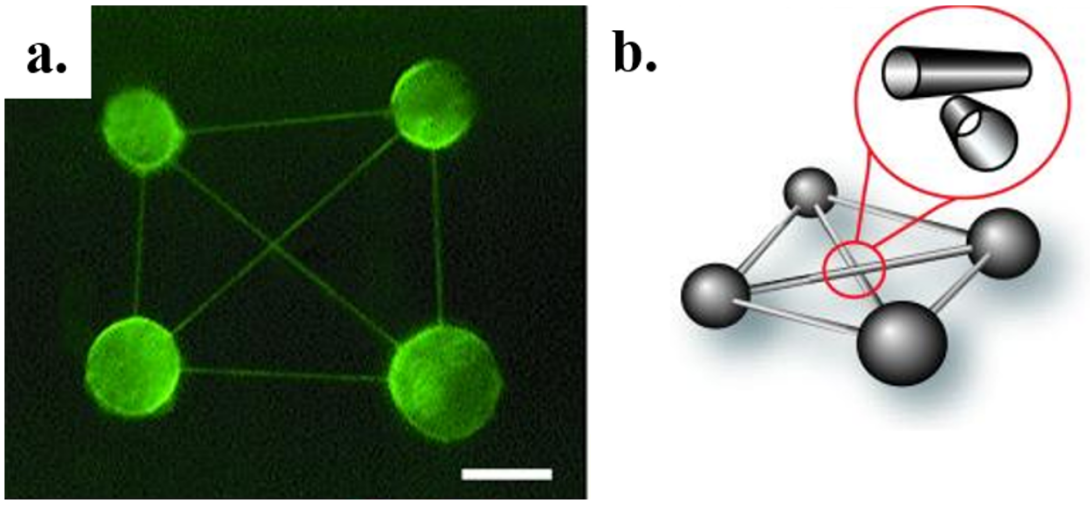

Figure 1.8: **Geometrically complex lipid nanotube-vesicle networks.** a, Fluorescence micrograph of the lipid membranes stained with a green fluorescent dye. The paths of nanotubes (green lines) are crossed in an overlaid fashion. Scale bar is 10 μm. b, Schematic for the formation of fully connected networks of GUVs using nanotubes. Image reproduced from Karlsson *et al.*[80] with permission.

The experimental approach taken by Carrara *et al.* used a "droplet transfer" method, whereby the different phases were layered and centrifuged sequentially, to create cooperative GUV colonies (Figure 1.9).[81] These synthetic tissues were created by placing the two different GUV populations (FITC [green fluorescent tagged]-dextran, and RITC [red fluorescent tagged]-dextran) into hydrophobic wells. The surface interac-

tions and differences in density between the internal and external phases caused the sedimentation of the GUV colonies. The researchers were able to mimic primitive solute capture, liposome fusion, and colony growth; all of which are the basic physicochemical mechanisms of primitive life forms. This work details a simple and easily reproduced methodology for the construction of higher order tissue-like aggregates. That said, the researchers had limited control over the relative sizes of the GUVs which made up their synthetic tissue, nor did they have control over the composition of the tissue itself. Moreover, these tissues possessed no independent functionality: in order to mimic colony growth, the GUVs had to be added manually.

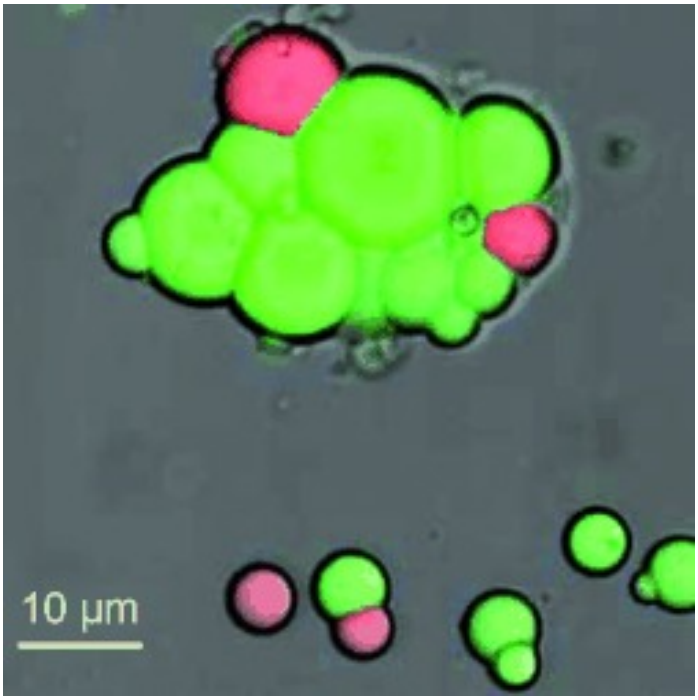

Figure 1.9: **Giant unilamellar vesicle colonies.** Artificial colonies, formed *via* the interaction of a binary population of giant vesicles (fluorescently tagged red and green) to form synthetic tissues. Image reproduced from Carrara *et al.*[81] with permission.

Mantri *et al.* engineered a dimeric protein pore that connected adjacent lipid bilayers in order to investigate the communication among compartmentalized parts of a tissue-like droplets (Figure 1.10).[82] They also evaluated the possibility of the dimeric

protein pore spanning more than one bilayer at a time – a common feature in biological membranes. Their choice to use bacterial (α7)-hemolysin pores as sub-units was due to its ability to communicate and execute its main function to transport molecules or ions along droplet bilayers shown in previous studies. This study serves as evidence for the capacity of liposomes to mimic *in vivo* intercellular communication and connections. That said, these synthetic tissues were not shown to be capable of performing life-like collaborative functions such as contraction.

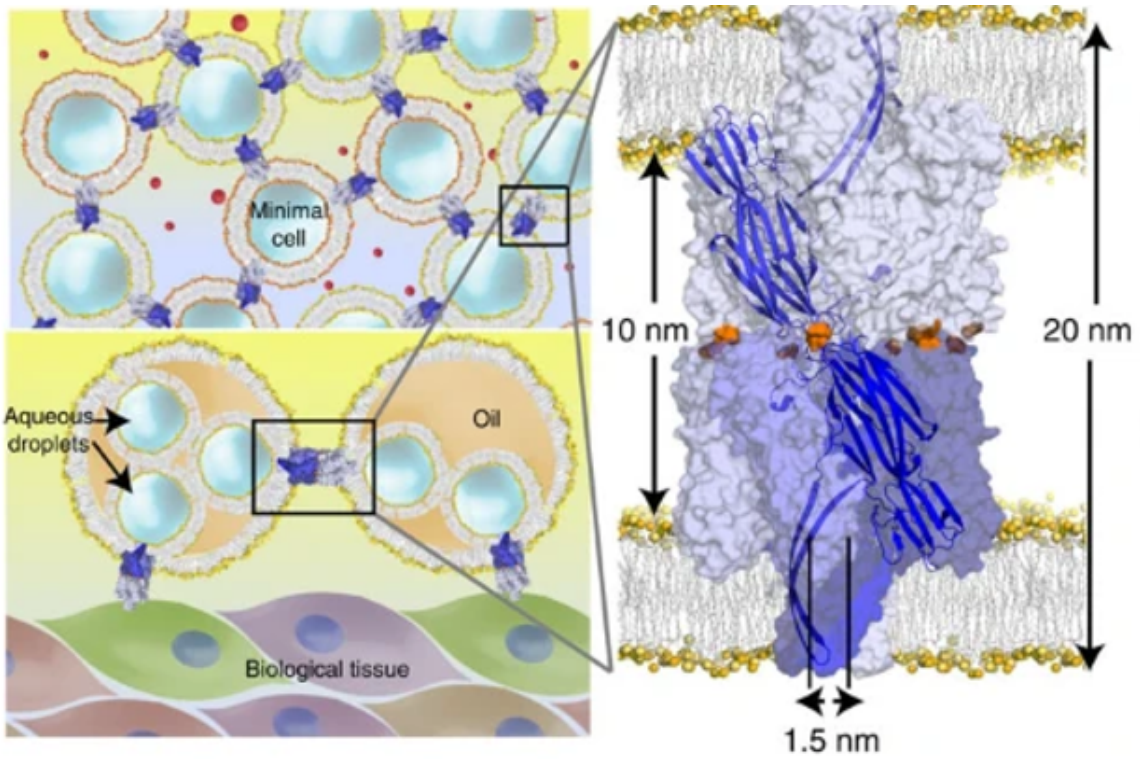

Figure 1.10: **An engineered αHL pore dimer** The upper panel shows schematic of synthetic cells made of liposomes communicating through proteins that connect them together. The lower panel shows monolayer-encased droplet networks attached to *in vivo* cells. Image on the right shows a space-filling model of the engineered pore dimer used to interconnect cells. Image reproduced from Mantri *et al.*[82] with permission.

For their synthetic tissues, Hadorn *et al.* used functionalized GUVs and W/O emulsion droplets with biotinylated single-stranded DNA oligonucleotides with streptavidin linkers.[83] As can be seen in Figure 1.11, they were able to demonstrate highly specific and reversible DNA-directed self-assembly of GUVs and emulsions into

vesicle-droplet hybrid structures. The researchers were also able to demonstrate that their controllable aggregation was reversible with respect to a temperature change. They claimed that application of this general assembly control system to diverse multiphase soft materials may provide the mechanism to assemble complex modular synthetic tissues in a controllable and reversible way. That said, aside from being able to control assembly and disassembly of their synthetic tissue-like materials, the researchers reported no other tissue-like functionality.

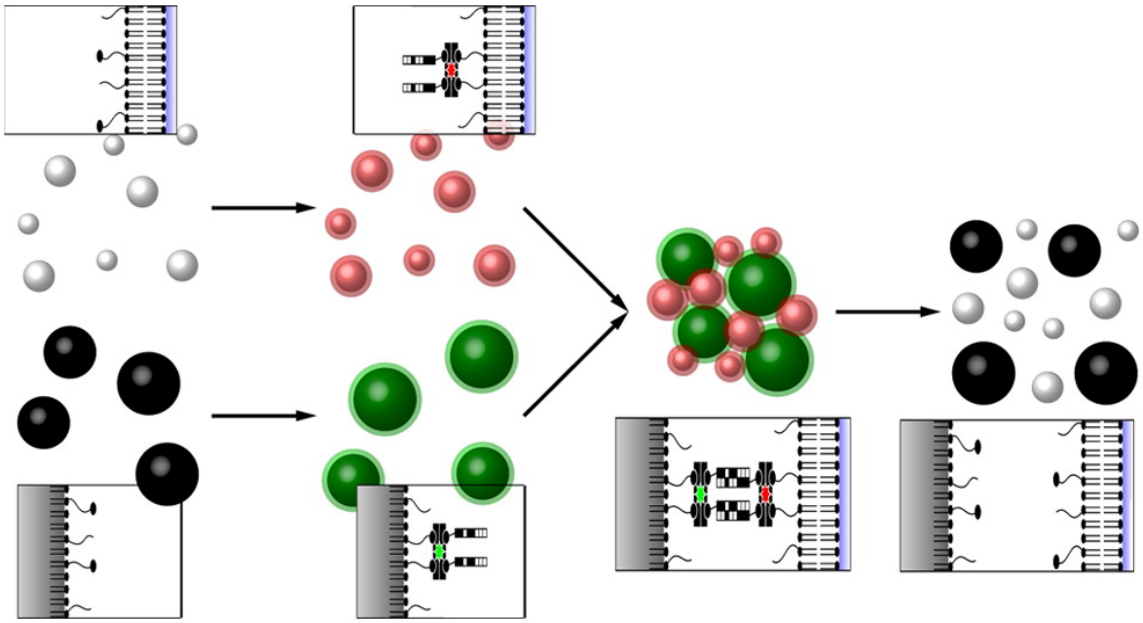

Figure 1.11: **W/O emulsion droplets with single-stranded DNA oligonucleotides.** Scheme showing the surface functionalization of droplets functionalized with complementary biotinylated single-stranded DNA oligonucleotides (btn-ssDNA). Binary mixture of liposomes (red and green) attached with complementary btn-ssDNA oligonucleotides. Scale bar is 5 μm. Image reproduced from Hadorn *et al.*[83] with permission.

Villringer *et al.* addressed some emerging questions in the bottom-up synthetic engineering of synthetic tissues by mimicking cell-to-cell adhesion using multivalent lectins with opposing binding sites that were are able to crosslink glycan-functionalised GUVs (Figure 1.12).[84] They observed that the crosslinking process of these multivalent lectins and glycan functional groups resulted in elongated cellular junctions. As a result, the GUVs took on the appearance of polygonal clusters which visually resem-

bled tissues *in vivo*. Interestingly, the ligand receptor interactions of these synthetic tissues were also shown to result in increased stability against sheer forces on account of fluid flow. The lectin-glycan GUV model was able to showcase that synthetic cell-to-cell adhesion *in vitro* provides stability in the same way as cell-to-cell adhesion *in vivo*; both are characterized as an intricate process of repulsion and attraction. This work is a notable contribution towards the design of synthetic tissues as they are shown to interconnect in a life-like manner. That said, the functionality of these synthetic tissues was limited to qualitative (visual) data and they were not shown to perform any collaborative functions.

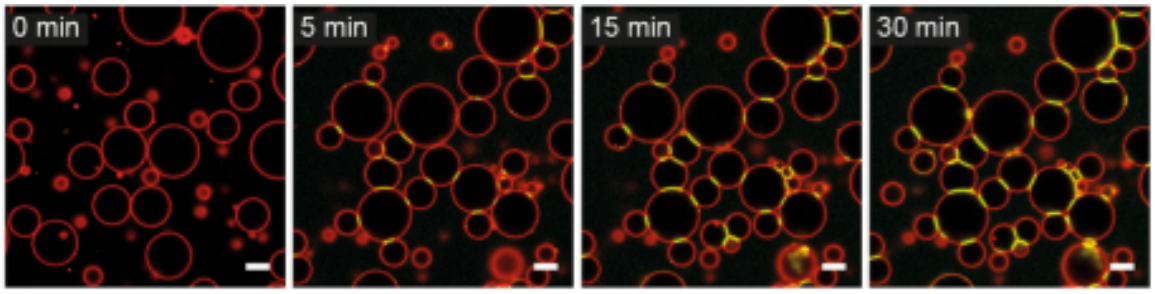

Figure 1.12: **Lectin-glycan functionalized GUVs.** Timelapse of lectin binding to glycan-functionalised (connection turns yellow) GUVs (red) which results in synthetic cells crosslinking to form synthetic tissues overtime. Image reproduced from Villringer *et al.*[84] with permission.

Bolognesi *et al.* outlined a novel method for the construction, reconfiguration and dismantling of higher-order liposomal assemblies using optical tweezers (Figure 1.13).[85] Optical tweezers are an instrument which uses a highly focused laser beam to hold and move microscopic objects in a manner akin to tweezers. Their liposomes were connected *via* electrostatically controlled adhesion. Using this methodology, distinct liposomes could be interconnected across length scales by axon-like tethers. Interconnection in this way facilitated material exchange between synthetic cells and allowed laser-triggered vesicle merging. This merging allowed for the mixing and dilution of intercellular content, as well as the initiation of protein expression *via* the delivery of biomolecular reaction components. The optical tweezer set-up also allowed for the

generation of highly precise and flexible synthetic tissues. That said, the set-up of the optical tweezers is labor intensive and requires a high degree of specialization to operate. It would be challenging to scale up this genre of synthetic tissue for multidisciplinary study.

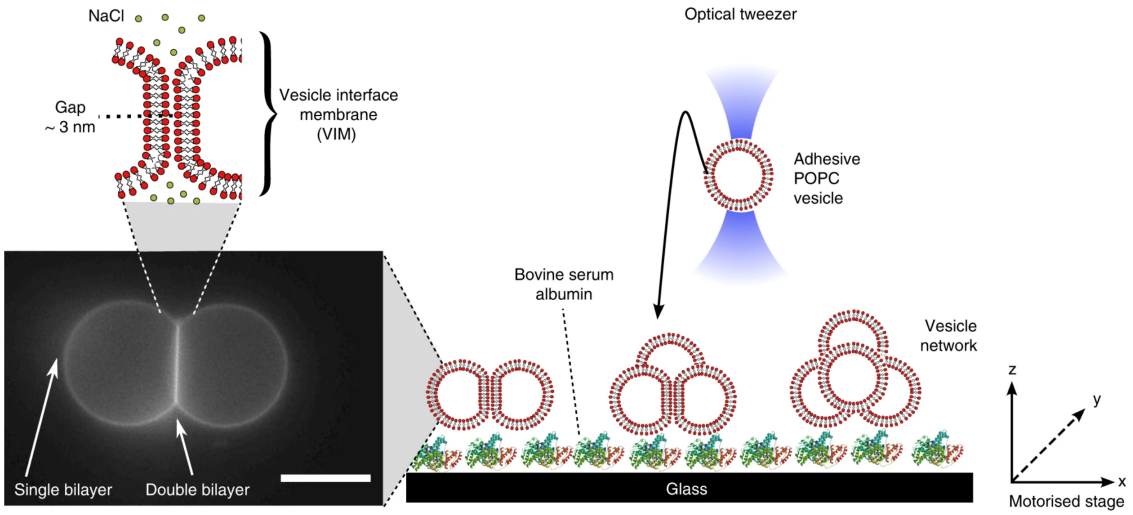

Figure 1.13: **GUVs assembled using optical tweezers.** Schematic for the setup for the controlled assembly of GUV networks using optical tweezers. Scale bar is 10 μm. Reproduced from Bolognesi *et al.*[85] with permission.

Recent work by Li *et al.* used magnetic fields to manipulate diamagnetic GUVs into programmed configurations. As can be seen in Figure 1.14, the magnetic arrangement was carried out on a stainless steel (SS) mesh with patterned microwells. Interestingly, like tissues *in vivo*, the GUVs in these synthetic tissues were shown to exhibit increased osmotic stability relative to their synthetic cell-like GUVs counterparts. Moreover, these magnetic GUVs were able to take on infinite 3D configurations and were shown to be able to perform feats of primitive communication. The formation of spatially coded and communicating micro-architectures from large quantities of synthetic cells, especially for lipid-based systems which most closely resemble cells *in vivo*, is still challenging. The work by Li *et al.* provides an important breakthrough in synthetic tissue design and construction. That said, the diamagnetic GUVs require

aqueous media containing high levels of toxic $MnCl_2$ and a constant magnetic field to maintain the patterns. By consequence, they are limited by how closely they can mimic true life-like structures.

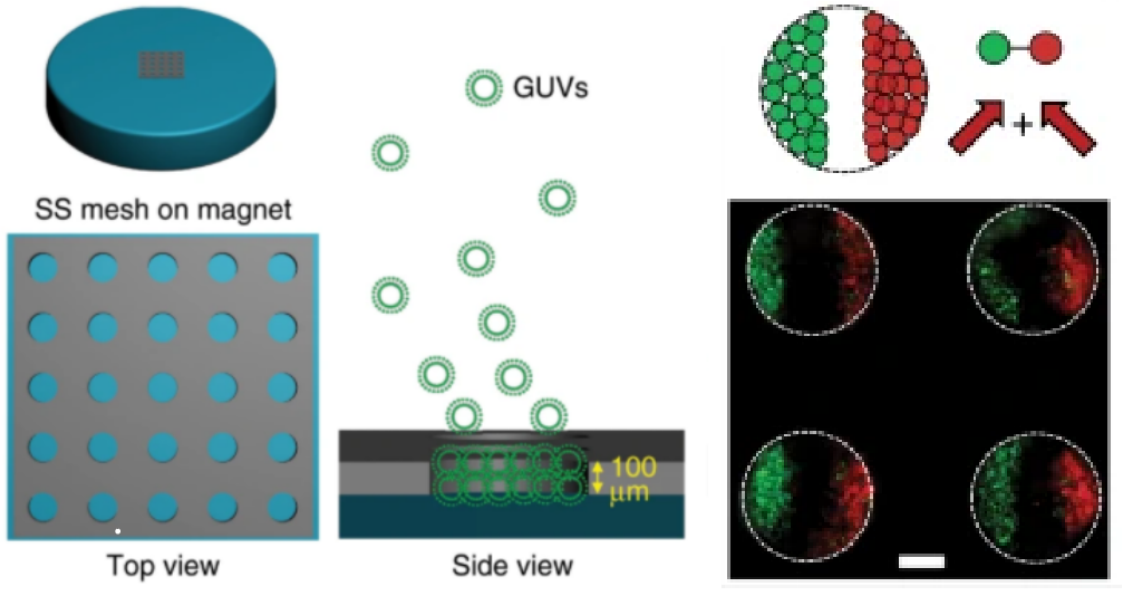

Figure 1.14: **Magnetic GUV tissues.** The image on the left shows a top and side view of the device used for GUVs assembly which consists of a SS mesh placed on a magnet. The image on the right shows a schematic and fluorescent image of the two different GUV populations assembling together. Image reproduced from Li *et al.*[86] with permission.

1.4.2.2 Droplet interface bilayers (DIBs)

Droplet interface bilayers (DIBs) are another commonly used bilayer arrangement of lipids. Contrary to liposomes however, DIBs are single lipid bilayers formed between two monolayer-coated aqueous droplets in an oil phase. A multisome is a more complex DIB (or multiple DIBs) which is encapsulated within a lipid monolayer. Funakoshi *et al.* were the first to create DIBs in 2006.[87] With DIBs, it is possible to more easily vary the lipid composition of the inner and outer leaflets so as to create asymmetry.[88] That said, DIBs are limited in their ability to accurately mimic cell-to-cell junctions seen *in vivo* between two separate sets of bilayers (instead, DIBs share a single bilayer). However, there are several DIB studies of interest to this literature

review as they showcase multiple linkages of synthetic cells through DIB formation that allow for the creation of synthetic tissues which display life-like characteristics.

The first approaches involved the manual layering of DIBs to form 2D and 3D networks (Figure 1.15). There are three examples in the literature which take this approach. Wauer *et al.* showed the assembly of DIBs in robust, freestanding magnetic 3D geometries (Figure 1.15a).[89] Dupin *et al.* outlined geometrically controlled 2D spatial arrangements of DIBs which contained synthetic *in vitro* gene circuitry (Figure 1.15b).[90] Lastly, Bachler *et al.* developed an approach whereby a microfluidic platform could be used to enable the precise positioning of nanoliter droplets with specific lipid compositions (Figure 1.15c).[91] In all articles, the researchers were able to demonstrate how pores could be inserted into the bilayers so that electrical and chemical communication pathways could be generated. Taken together, these methods mark an important step toward the simple and programmable engineering of synthetic tissues using DIBs which are capable of life-like communication. That said, these manual methods are not easily scaled up to be high throughput and the researchers were only studied a few dozen synthetic cells at a time.

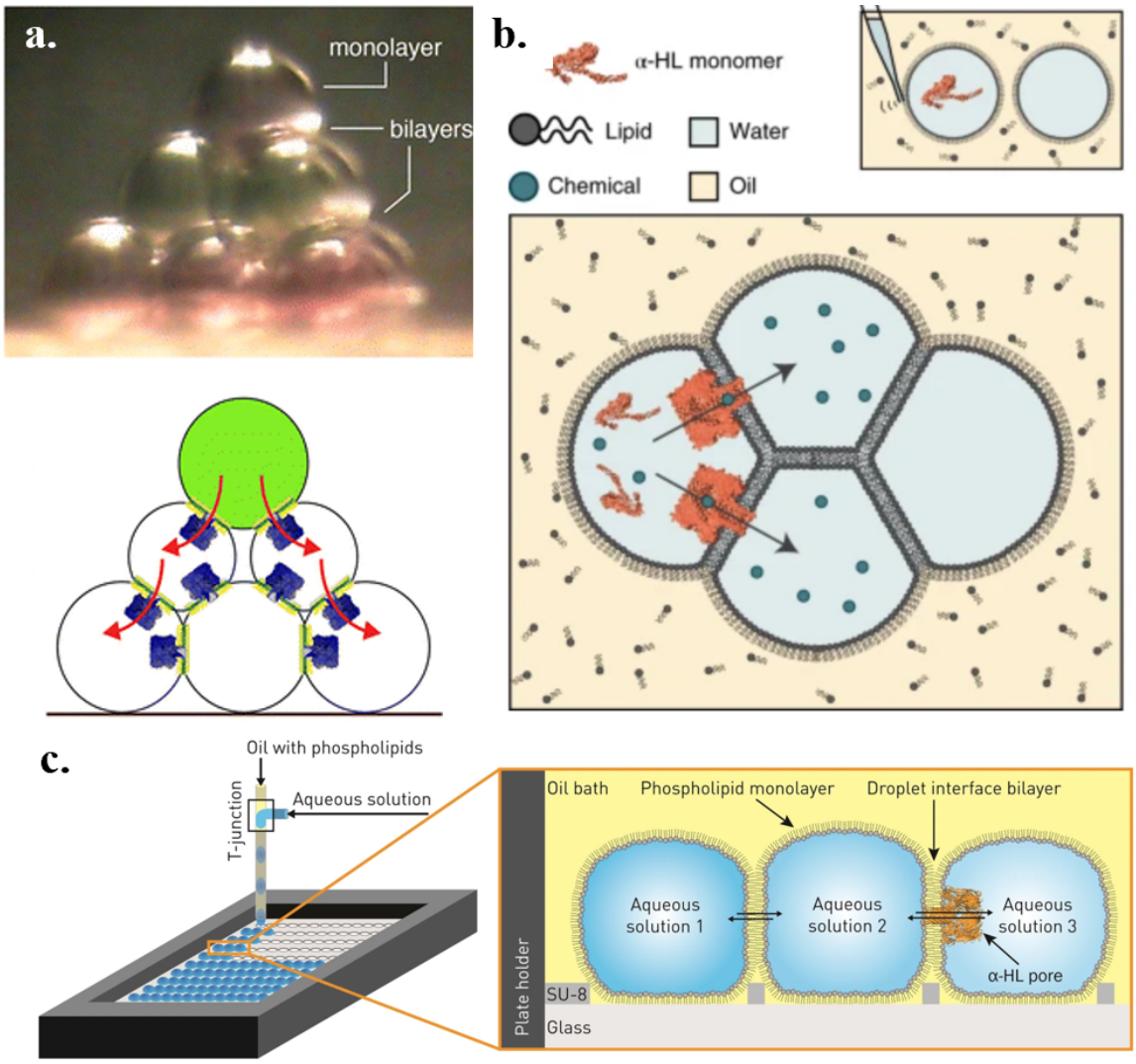

Figure 1.15: **2D and 3D DIB-based synthetic tissues.** a, Image of lipid-coated droplets in a robust, freestanding 3D geometry (top) along with a scheme depicting pore insertion between droplets for intercellular communication (bottom). Image reproduced from Wauer *et al.*[89] with permission. b, Scheme of the DIB networks showing the water droplets (blue) which are incubated in a lipid-in-oil bath (yellow) where they form DIBs. Protein pores such as α-haemolysin (orange) can incorporated into the bilayers. Image reproduced from Dupin *et al.*[90] with permission. c, Schematic of synthetic tissue formation from DIBs. Image on the left shows nanoliter droplet formation using a microfluidic T-junction onto an array. Image on the right shows DIB configurations. Images reproduced from Bachler *et al.*[91] with permission.

More recent approaches in the generation of synthetic tissues from DIBs involve the use of 3D printing to scale-up. Villar *et al.*'s 2013 study focused on DIBs to assess the potential of several thousands of aqueous droplets to form a stable network and behave in a coordinated manner that mimicked living tissues (Figure 1.16a).[92] They 3D

printed aqueous droplets using droplet generators and submerged these droplets into a lipid-containing oil environment to enable DIB formation. These printed bilayer networks were structurally and thermodynamically stable with relative resistance to external forces. Villar *et al.* assessed the tissue-like functionality of their DIB networks though the insertion of α-hemolysin (a pore protein). Alcinesio *et al.* followed up on this work with an improved 3D printing technique which permitted the fabrication of complex synthetic tissues, where precisely positioned compartments could perform coordinated tasks (Figure 1.16b).[93] Both articles make use of 3D printing, a useful and high throughput technique, in the generation of their synthetic tissues. These DIB networks were also capable of cell-cell interconnection and life-like intracellular communication. These networks contained no coordinated functionalities which limits the extent to which they can be compared to *in vivo* tissues. The 3D printed techniques used are also highly technical and require significant experience to operate and reproduce.

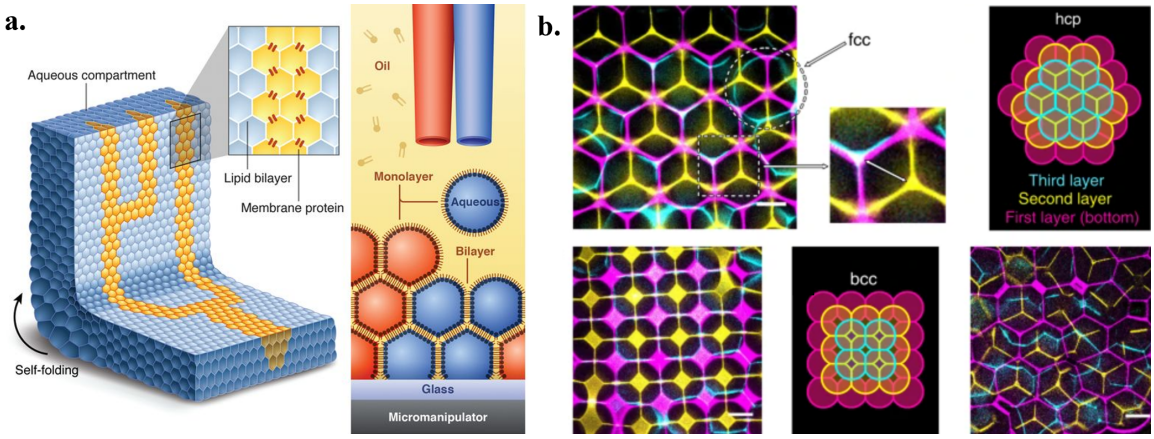

Figure 1.16: **3D printed DIBs.** a, Schematic of a printed droplet network as well as the printing process. Shows two different aqueous droplet generators which deposit droplets into lipids dissolved in oil. Image reproduced from Villar *et al.*[92] with permission. b, Confocal and schematic images of sophistically organized DIBs into predetermined patterns. Images reproduced from Alcinesio *et al.*[93] with permission.

There are two notable studies conducted by Bayoumi *et al.*[94] and Baxani *et al.*[95] which explore the incorporation of DIBs into hydrogels for added stability and as

a step towards the generation of synthetic tissues (Figure 1.17). Bayoumi *et al.* used a hydrogel comprised of an agarose matrix in order to encapsulate manually inserted aqueous droplets (Figure 1.17a). On the other hand, Baxani *et al.* used a microfluidic system to form a hydrogel layer made of alginate which then surrounded a predetermined number of DIBs (1.17b)[95]. Both studies confirmed the viability of hydrogel materials to enhance the structure stability of DIBs between multiple droplet compartments for the bottom-up synthesis of synthetic tissues from DIBs. However, the addition of a hydrogel stabilizer limits the degree to which these DIBs systems can be compared to life-like tissues.

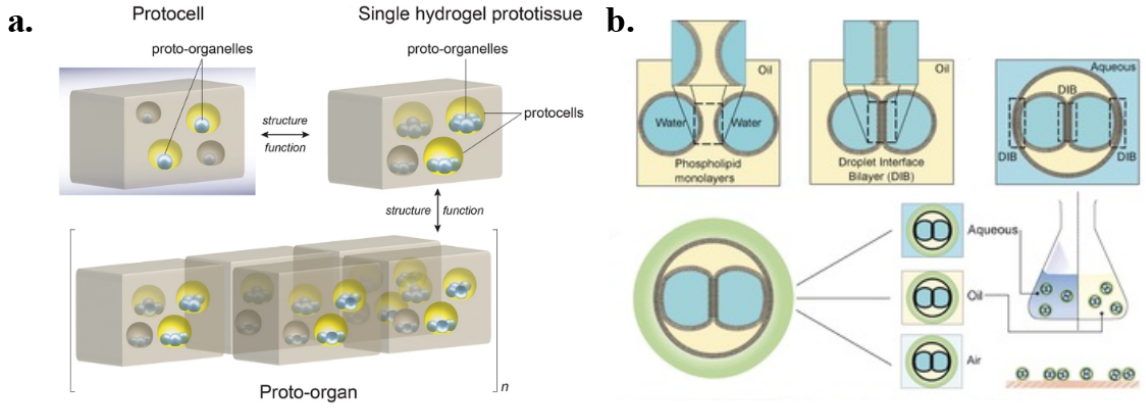

Figure 1.17: **Droplet interface bilayers in hydrogel.** a, An assembly of synthetic cells (termed protocells) suspended in hydrogels (brown boxes). Multiple aqueous droplets in the same oil compartment (also embedded in hydrogel) are termed synthetic tissues (or proto-organelles). Image reproduced from Bayoumi *et al.*[94] with permission. b, Schematic showing the formation of DIBs from two droplets of water in oil (with added lipid) which are subsequently encased in a hydrogel droplet. Below highlights the stability of these DIBs in air, oil and water. Image reproduced from Baxani *et al.*.[95] with permission.

There are also examples in the literature of DIBs in aqueous environments instead of an external environment composed of oils.[88] Villar *et al.* explored the significance of DIB interactions and functionality in an aqueous physiological environment that more closely resembled the physiological environment of living cells.[96] Figure 1.18, shows a visual representation of their multisomes. Bilayers were formed between the innermost aqueous droplets and between the aqueous droplet and the oil monolayer.

A follow-up study by Booth *et al.* constructed synthetic tissues in the same manner but they were capable of more sophisticated communication.[97] One droplet contained a protein synthesis system and a prodrug-activating enzyme. The second droplet contained a small-molecule prodrug analog. When a Zn^{2+} sensitive protein pore was made in the first droplet, it allowed the prodrug to become activated by the enzyme in the second droplet. For both publications, the change in external environment from a hydrophobic to aqueous improved the biomimeticity of these synthetic tissues without compromising the incorporation of channels or pores which enable functionality. That said, due to the confines of the oil droplet which must surround the DIBs, there is a limit to the size and complexity of these synthetic tissues.

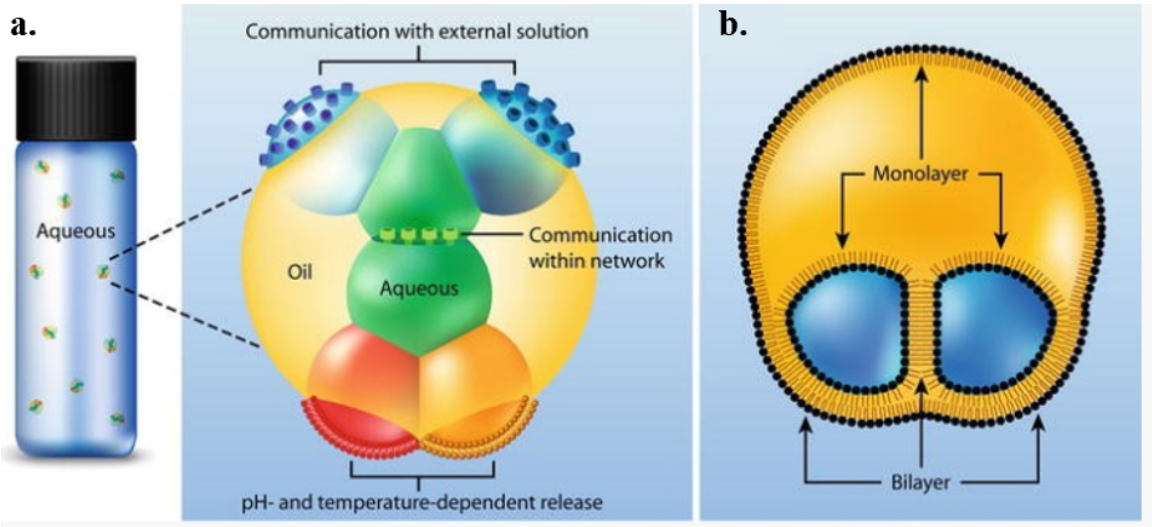

Figure 1.18: **Multisomes.** a, Image of a multisome with two inner droplets of different composition. These aqueous droplets are connected by lipid bilayers, which allow for communication through protein pores. b, Simpler schematic of the multisome. Images reproduced from Villar *et al.*[96] with permission.

There are also examples of synthetic DIB-based tissues performing more sophisticated life-life communication. Booth *et al.* made use of a light-activated DNA promoter which could be used to turn on the expression of genes within the synthetic cells (Figure 1.19a).[98] In their follow-up article,[99] they demonstrated external control of DIB networks by activating protein expression within a singular droplet which resulted in

graded levels of protein expression (Figure 1.19b). Both studies are notable examples of higher-level communication within DIB-based synthetic tissue. That said, the DIBs are contained within a surrounding oil environment to maintain stability which limits the biomimeticity of these synthetic tissues.

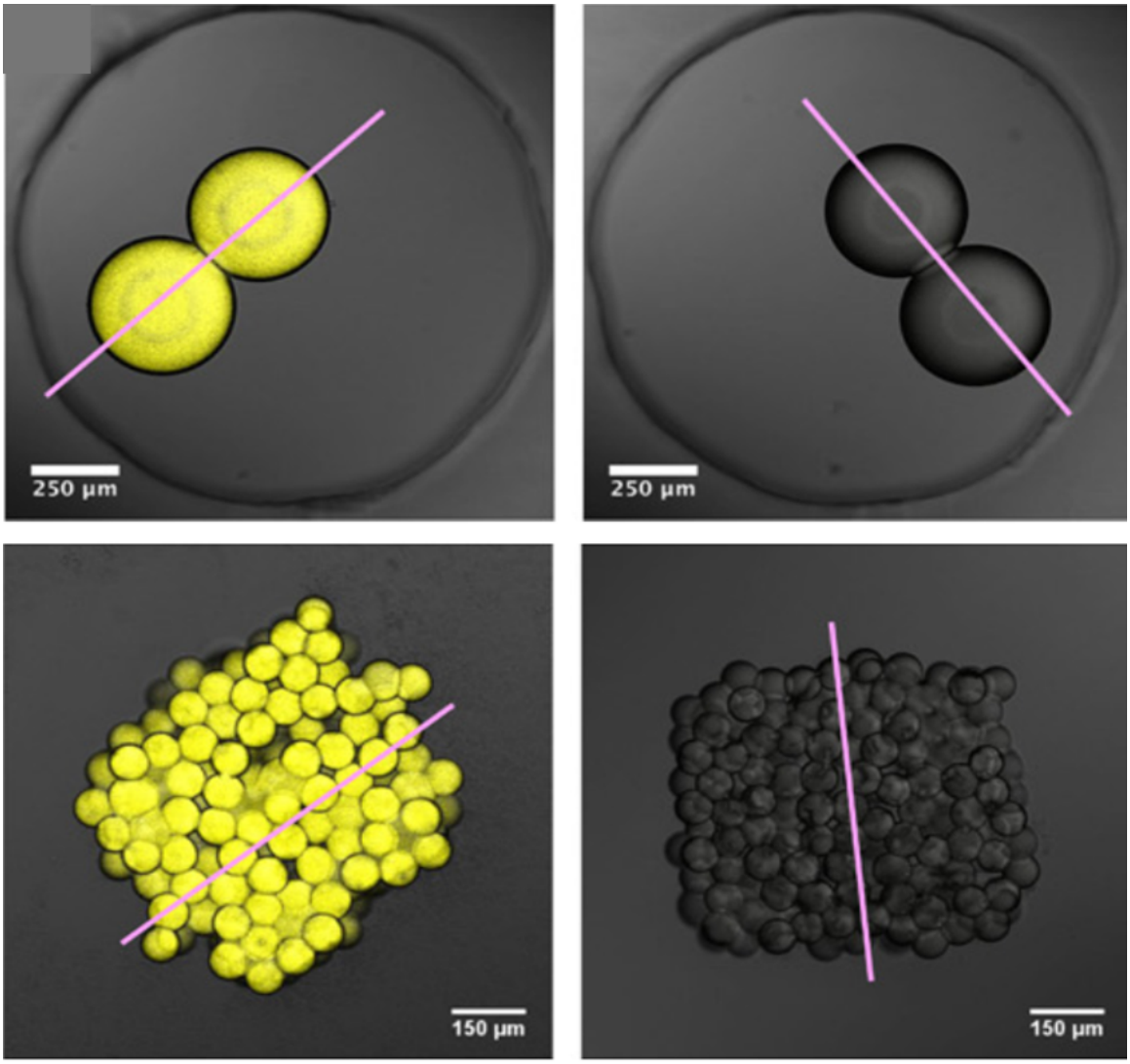

Figure 1.19: **Light activated DIBs.** Top images show synthetic cells containing DNA which expresses protein (yellow) upon light activation. Bottom images show a larger grouping of these light-activated synthetic cells into light-activated synthetic tissues. Image reproduced from Booth *et al.*[98] with permission.

1.5 Aim of my work

Though the field of bottom-up synthetic cells and tissues is still in its infancy, there have been a number of notable breakthroughs in recent times. The following dissertation details how microfluidic technologies allow for the precise and accurate control over the bottom-up construction of synthetic cells and tissues; this is essential for the minimization of confounding variables in their quantitative study.

There are three core aims that I sought to address throughout my PhD:

1. Engineer reliable microfluidic platforms for the generation of double emulsions.

2. Use these platforms for the fundamental study of synthetic cells.

3. Generate more complex functional synthetic tissues from these synthetic cells in a bespoke manner.

My first aim was to engineer a statistically reliable microfluidic platform for the generation of double emulsions. I wanted to know if the platform would allow the incorporation of biological components (lipids and proteins) into the double emulsions. This aim sought to address the gap present in the literature for statistically reliable, reproducible, and user-friendly microfluidic double emulsion platforms.

My second aim was broken down into two subsections. The first subsection involves the use of my microfluidic platform to generate polymeric synthetic cells which are capable of interconnecting as a step towards the generation of prototissues. The second was to address the question of whether I could create lipid-based synthetic cells for drug development. This aim sought to build upon the burgeoning field of synthetic cells by adding a layer of life-like complexity (such as the novel ability to interconnect) using microfludic tools.

My third aim was to use these microfluidic platforms and synthetic cells to build synthetic tissues. More specifically, I sought to highlight new features and functions that had not been observed before through the use of microfluidic technologies.

Hence, my dissertation contains the following chapters:

Chapter 1 details a review of the literature which is required to understand the dissertation. Specifically contains a review of double emulsions, synthetic cells and synthetic tissues.

Chapter 2 describes my work on the development of a glass microcapillary platform, which was undertaken to facilitate later research on biomimetic lipid-based synthetic cells. This work is in review in Lab on a Chip.

Chapter 3 describes my work on the development of a PDMS microfluidic platform, which was undertaken to facilitate later research on polymeric-based synthetic cells and tissues.

Chapter 4 describes my work on lipid-based synthetic cells which were generated using my previously described microcapillary device. This work could be applied to model red blood cells for the study of passive malarial drug diffusion.

Chapter 5 describes my fundamental studies on polymeric-based synthetic tissues using my previously described PDMS microfluidic device. This work is under review in Chemical Science.

Chapter 6 details the impact of the work done in my dissertation. I also enumerate avenues for future work.

Chapter 2

A plug-and-play modular microcapillary platform for the generation of multicompartmental double emulsions using glass or fluorocarbon capillaries

Microfluidic technologies are a powerful tool for the generation of monodisperse double emulsions which can be used in multidisciplinary applications such as medicine and biochemistry. However, microfluidic platforms are limited to laboratories that have the knowledge to design, fabricate and operate them. Even in experienced microfludic laboratories, the porosity of PDMS (the most commonly used material for microfluidic device fabrication) can pose several disadvantages to biologically relevant studies as it can result in the absorption of small hydrophobic molecules such as drug or bio-

molecules to the surface of the microfluidic device.[100] Hence, I designed and developed a cheap microcapillary device that requires only glass and PTFE microcapillaries and a cheap 3D printer in order to make multicompartmental double emulsions.

I conceived the original idea and performed all of the experimental work presented in the following publication. Sean Farley, originally an undergraduate work-study student in our group, now a Master's student, designed and tested the 3D printed mould and junction boxes. Sean Farley also analysed all of the data. Dr Elvira, Sean Farley, and I wrote and revised the manuscript, which is now published in Lab on a Chip. I wrote the first draft of the Abstract, Introduction, figure captions, approximately 1/3 of the Results and Discussion section, and the Materials and Methods section. I also made all of the figures. For my early pre-publication work, please refer to Appendix C.

2.1 Introduction

As a technology, droplet microfluidic devices are impactful because they allow unprecedented control over minute volumes of fluids in high-throughput. Particularly multiple emulsions, which are droplet systems composed of at least three immiscible fluids arranged as droplets encapsulated within one another, have found application in areas such as drug development and delivery[13,101,102] because encapsulation enables precise control over the composition and dosing regime of the formulation.[103] For most biological applications, double emulsions, which are the most commonly used type of multiple emulsion, usually take the form of a water droplet, inside an oil droplet, in a water surrounding phase, otherwise known as water-in-oil-in-water emulsions (W/O/W),[104–106] but all combinations are possible, giving rise to oil-in-water-in-oil (O/W/O)[107,108] and oil-in-oil-in-water (O/O/W)[109] double emulsions. An extra level

of complexity can be added in the form of multicompartmental double emulsions, where several droplets of the innermost phase are encapsulated in the middle (and then outer) phases. These inner droplets can be of the same composition or, to create more sophisticated systems for use as, for example, artificial cells[110], of different compositions[111].

Despite their potential, droplet microfluidic devices are not commonly used outside of specialised academic laboratories, and are underutilised in industrial settings. This is in part due to the complexity associated with the design, fabrication and operation of microfluidic platforms and because of the cost associated with setting up the "lab-around-the-chip". Microfluidic devices are most most often fabricated from polydimethylsiloxane (PDMS), a cheap but porous silicon polymer, which also limits the reproducibility of the droplet systems created on these platforms.[112] Thermoplastic or glass microfluidic devices are more reliable, but are even more complicated to fabricate, requiring access to expensive equipment for hot embossing or injection molding, or familiarity with wet etching processes, respectively.[113] A key advantage of microfluidic devices made from thermoplastics is that they are amenable to mass production for commercial applications,[114] and a key advantage of glass microfluidic devices is that they can be used with almost any type of solvent.[115] Although glass microfluidic devices are not highly amenable to mass production for commercial applications, they can be easier to use in non-microfluidic academic laboratories because of the inherent stability of glass surfaces, which is lacking in PDMS devices.

One way to simplify the fabrication of glass microfluidic devices for double or multiple emulsion formation is to use glass microcapillaries as the microfluidic channels.[116] In these systems, two glass capillaries are placed within one another to form the inner droplets using coaxial flow of the inner and middle phases, which move in the same

direction. A third glass capillary is placed on the outside to create the outer droplets, which are formed using coaxial flow inserted in the opposite direction. Generally, the capillaries are aligned manually so as to enable droplet formation,[117] and they are then glued to a glass microscope slide to hold them in place.[118] In most cases, the tips of the capillaries are heated and extended (flame tipping) to decrease their inner diameter to enable the formation of smaller droplets. However, both the manual alignment of the capillaries and the flame tipping process are very user dependent, and hence the inter-device reproducibility is low.[119] A more reproducible method is to use machining to make holders for the glass microcapillaries, though this requires access to expensive specialised equipment. For example, holders can be fabricated using computer numerical control (CNC) machining of polyoxymethylene copolymer blocks,[120] or a CNC sliding head lathe can be used to produce end caps with large recesses into which the capillaries are inserted.[119]

More recently, new methods for aligning the capillaries have been developed. One method is to use "off the shelf" components such as PEEK tees[121,122] or glass microscope slides and cover slips[123] as makeshift holders for the glass microcapillaries. The advantage of these approaches is that they are easy to make, but they often do not allow the generation of more complex droplet systems and can be prone to leaking. Therefore, another approach uses 3D printing to generate holders for the glass capillaries that have screws to accurately bring the opposing capillaries close to each other for droplet creation. In one example, these holders were then placed on a base for alignment,[124] but this base can warp during the printing process, which causes misalignment of the capillaries, unless it is made using a high-end 3D printer that adjusts the temperature, or has a box to create an even temperature distribution during the printing process. In addition, as the authors state, the seal between the rigid 3D printed holders and the glass capillaries is variable and hence an adhesive

is often required to glue the capillaries to the holders. A more recent approach does not use a base to align the capillaries and adds O-rings to limit leaking.[125] However, this approach still requires the use of a high-end 3D printer to accurately and reliably print the screw for alignment of the capillaries so as to limit leaking through the screw thread.

Despite their potential for being an easy method of making microfluidic devices for multiple emulsion formation, the assembly of glass microcapillary platforms is still laborious, costly and not reproducible. Hence, this technology has not been widely adopted for use outside of microfluidic academic laboratories. There are four main challenges associated with current methods for the creation of glass microcapillary platforms. Firstly, the alignment of the capillaries is difficult to control and reproduce. Secondly, the glue that is often required for device assembly can block the glass capillaries, can contaminate the fluid phases, and the assembled platform cannot easily (or not at all) be disassembled and cleaned for reuse. Thirdly, the most reproducible methods for holding and aligning glass capillaries require high-end equipment for machining or 3D printing. Lastly, to make different types of multiple emulsions the surface of some of the glass capillaries needs to be treated to make them hydrophobic, which is cumbersome.

Here we present a simple and modular plug-and-play microcapillary platform that overcomes these problems. Our microcapillary device uses any combination of glass and/or polytetrafluoroethylene (PTFE) capillaries which are aligned by simple insertion into junction boxes to make multicompartmental double emulsions. These junction boxes are fabricated using a low cost 3D printer to create a mould to cast the boxes from a flexible polyurethane resin. The use of this resin means that no gaskets or glue are needed to stop leaking. Hence the platform is reusable and reconfigurable

by simply switching out different types of capillaries to create the surfaces required for the formation of different types of multicompartmental double emulsions. The combination of hydrophilic (glass) and hydrophobic (PTFE) capillaries negates the need to perform surface modification of the capillaries and the type of coaxial flow we use removes the necessity of capillary alignment and ensures reproducibility between trials, devices, and researchers. We show the modular plug-and-play nature of our microcapillary platform by using it to form a variety of multicompartmental double emulsions and quantify droplet formation accuracy and reproducibility for between 1 and 10 inner droplets in each case. We form water-in-oil-in-water (W/O/W), oil-in-water-in-oil (O/W/O) and oil-in-oil-in-water (O/O/W) multicompartmental double emulsions in addition to binary W/O/W multicompartmental double emulsions where the inner droplets have different compositions.

2.2 Materials and methods

2.2.1 Materials

Light mineral oil, sodium dodecyl sulfate (SDS), FC-40, and 1H,1H,2H,2H-perfluoro-1-octanol (97%, PFO) were purchased from Millipore Sigma. Standard Resin for printing the mould was purchased from Elegoo. Polyurethane resin (Vytaflex 30) and Release Spray were purchased from Smooth-on. Iroshizuku Fountain Pen Ink was purchased from Amazon (Vermillion Red and Light Blue). All reagents were used as received. Glass capillaries were purchased from Vitrocom. Polytetrafluoroethylene (PTFE) tubing was purchased from Zeus Inc. or Chromatography Specialties. Jensen global 20 and 30 gauge IT series blunt stainless steel needles were purchased from Howard Electronics.

2.2.2 Fabrication of the junction boxes

The modular microcapillary platform is a coaxial assembly of three sizes of glass and/or PTFE capillaries held together and aligned using junction boxes cast from 3D printed moulds. The junction boxes were made from polyurethane resin with different inlet and outlet holes sized to fit the OD of the different capillaries. Each junction box was made from two moulds, one for the inlet half of the box and one for the outlet half (Figure S1). Sections of the mould that are negatives for capillary holes were sized slightly smaller than the OD of the capillary to ensure a tight fit. Size parameters for capillary hole negatives were determined experimentally, and once a correct fit was found we were able to reproducibly manufacture parts that fit the capillaries. The size of capillary that can be held by the junction box is limited by the resolution of the printer. We were able to print negatives small enough to hold capillaries with an OD of 0.33 mm using our printer. The moulds for the junction boxes were designed using Fusion 360 (Autodesk, see ESI) and 3D printed using a Mars Pro 3D Printer (Elegoo). The Elegoo Mars is a consumer 3D printer that uses Digital Light Processing (DLP) and costs 200 US dollars. The moulds were printed using Standard Resin that cures at 405 nm, with a layer height of 0.01 mm and a light exposure time of 8 s per layer. Moulds were then washed with isopropanol to remove uncured resin. Polyurethane resin was used to cast the junction boxes. The resin was chosen because its low hardness (30A shore hardness) allows it to seal the capillaries despite surface imperfections without the need for gaskets or adhesives. The polymer and crosslinker were mixed in a 1:1 ratio according to manufacturer instructions. The moulds were sprayed with mould release (Smooth-on) and the mixed polyurethane resin was poured in. Inlet and outlet moulds were then mated and held together with rubber bands, and the resin was left to cure for 18 hours at room temperature.

Table 2.1: Capillaries used for the formation of W/O/W, O/W/O, O/O/W and binary W/O/W multicompartmental double emulsions, where ID denotes the inner diameter and OD denotes the outer diameter

	Inner
Water/Oil/Water Emulsions	Glass capillary (ID = 0.40 mm, OD = 0.55 mm)
Oil/Water/Oil Emulsions	Glass capillary (ID = 0.20 mm, OD = 0.33 mm)
Oil/Oil/Water Emulsions	Glass capillary (ID = 0.40 mm, OD = 0.55 mm)
Binary Water/Oil/Water Emulsions	PTFE tubing (ID = 0.5 mm, OD = 0.9 mm)
	Middle
Water/Oil/Water Emulsions	PTFE tubing (ID = 0.75 mm, OD = 1/16 inch)
Oil/Water/Oil Emulsions	Glass capillary (ID = 0.70 mm, OD = 0.87 mm))
Oil/Oil/Water Emulsions	Glass capillary (ID = 1.50 mm, OD = 1.80 mm)
Binary Water/Oil/Water Emulsions	PTFE tubing (ID = 1.50 mm, OD = 1.80 mm)
	Outer
Water/Oil/Water Emulsions	Glass capillary (ID = 2 mm, OD = 4 mm)
Oil/Water/Oil Emulsions	PTFE tubing (ID = 1.45 mm, OD = 1.75 mm)
Oil/Oil/Water Emulsions	Glass capillary (ID = 2 mm, OD = 4 mm)
Binary Water/Oil/Water Emulsions	Glass capillary (ID = 2 mm, OD = 4 mm)

2.2.3 Assembly of the modular microcapillary platform

Junction box 1 connected one or two inner capillaries and a middle capillary made from either glass or PTFE. The inner capillary was inserted into the inlet (or inlets) of the first junction box and exited the outlet of the second junction box. The middle capillary was inserted into the outlet of the first junction box and also exited the outlet of the second junction box. The middle phase was inserted from the top of the first junction box. Junction box 2 allowed the addition of the outer capillary (glass or PTFE). The outer capillary was inserted into the outlet of this box and the outer phase was inserted through the top of the box. The multiple emulsions were created in the outer capillary. The specific assembly varied depending on the type of emulsion formed, with the material chosen to support the relevant fluid phase. The capillaries used for the data acquired in this paper are shown in Table 2.1.

For easy connection to syringes, the capillary (glass or PTFE) used for the inner phase (or phases) was inserted into another piece of PTFE tubing with a larger ID (called the connecting tubing). The ID of the connecting tubing was 0.25 mm when using a glass capillary for the inner phase, and 0.75 mm when using PTFE tubing for the inner

phases. In both cases the OD was 1/16 inch. By heating the connecting tubing with a flame it was possible to insert the end of the inner capillary into the now-flexible connecting tubing. Upon cooling, a seal formed between the inner capillary and the connecting tubing. This connecting tubing was then inserted all the way through the inlet of the first junction box until it reached the edge of the box itself. It is also possible to cut the inlets and outlets of the junction boxes so that they are smaller, and it is hence easier to insert the smaller and more fragile capillaries. Two other pieces of connecting PTFE tubing (ID = 0.75 mm, OD = 1/16 inch) were heated and connected to 20 gauge blunt needles detached from their luer fittings. These were then inserted into the top of both junction boxes to introduce the middle and outer phase reagents. The other ends of these three pieces of connecting tubing were heated and connected to syringes using 30 gauge blunt needles. For stable multicompartmental double emulsion generation in this outer capillary, the inner capillary should be about 1-2 inches shorter than the middle capillary, which should be a minimum of 1-2 inches shorter than the outer capillary.

2.2.4 Generation of multicompartmental double emulsions

Nemesys syringe pumps (Cetoni) and glass gas-tight syringes (25 mL, Hamilton) were used to pump fluids into the modular microcapillary platform. O/O/W emulsions were formed using FC-40 as the inner phase, mineral oil as the middle phase and reverse osmosis (RO) water with 1% w/w SDS as the outer phase. O/W/O emulsions were formed using RO water with 1% w/w SDS as the inner phase, 2.5% v/v PFO in FC-40 as the middle phase, and RO water with 1% w/w SDS the outer phase. Binary W/O/W multicompartmental double emulsions were formed using RO water with 1% w/w SDS as the inner phase, 2.5% v/v PFO in FC-40 as the middle phase, and RO water with 1% w/w SDS as the outer phase. Red and blue dyes were added to the

inner phases to aid visualization of the two different types of inner droplets (0.25% v/v). Flow rates were varied to create multicompartmental double emulsions with between 1 and 10 inner droplets as described in the Results and Discussion section. Droplet formation was observed using a stereomicroscope (SMZ800N, Nikon). Videos were captured using a digital SLR camera (Canon EOS 6D Mark II) mounted on the stereomicroscope (for top view images). Videos can also easily be acquired with a phone camera instead of the stereomicroscope/camera set-up (for side view images). Images shown here are top view, representative side view images can be seen in Figure S2 in the ESI.

2.2.5 Data analysis

Videos were analyzed using ImageJ (version 1.47T). The average size was calculated for the inner and outer droplets by measuring the two-dimensional surface area of each droplet in the image. This ensures accurate and comparable measurements regardless of where the droplets are spherical or ellipsoidal. Data used to analyse the accuracy of encapsulation was calculated using three replicates of at least 10 droplets. Data used to analyse the droplet size was calculated using at least 10 droplets for the outer droplet and between 10 and 100 droplets for the inner droplets.

2.3 Results and discussion

Our modular microcapillary platform uses junction boxes made from a flexible resin using 3D printed moulds to hold and align the capillaries used for multicompartmental double emulsion formation. The platform is plug-and-play because the capillaries are off-the-shelf components that can be inserted into the junction boxes manually. Figure 2.1a shows the overall platform and how the inner, middle and outer phases

are inserted into the junction boxes through their respective capillaries. The multi-compartmental double emulsions are formed using coaxial flow of the three phases in the outlet capillary. Since the three fluid phases are all moving in the same direction, another advantage of our modular microcapillary platform is that precise alignment between capillary is not required for stable droplet formation. Depending on the composition and size of the multicompartmental double emulsions to be formed, a different set of glass or fluorocarbon capillaries are used (Table 2.1).

To put the platform together, the inner phase capillary is inserted the whole way through the platform from the inlet of the first junction box until it exits the second junction box (Figure 2.1a). The middle phase capillary is inserted into the outlet of the first junction box, and also exits the second junction box. The outer phase capillary is inserted into the outlet of the second junction box. To do this, a blunt syringe tip was physically pushed through the top portion of the soft resin material to create a small puncture. The middle and outer phases are inserted directly into the top of the first and second junction boxes respectively, thus enabling coaxial flow of the middle phase around the inner capillary, and then coaxial flow of the outer phase around the middle capillary. Precise alignment of the capillaries is not required. For stable droplet formation, the end of each capillary is generally between 1-2 inches shorter than the end of the next largest capillary. These distances can be easily adjusted if necessary by pulling the capillaries manually into position.

The junction boxes have been designed such that each component can be switched out at will, hence creating a plug-and-play modular microcapillary platform. By combining hydrophilic glass capillaries and hydrophobic PTFE tubing, multicompartmental double emulsions of various sizes and compositions can easily be generated without the need for surface modification of the capillaries. The moulds for the junction boxes

are 3D printed so that the inlets and outlets of each junction box match the outer diameter (OD) of the capillaries used, which means that flame-tipping or pulling the glass to a taper is not required to form smaller droplets. An example mould can be seen in Figure 2.1b. The flexible resin junction boxes that hold the capillaries are then manufactured by casting them in the 3D printed moulds. Figure 2.1c and d show a side view and a top view, respectively, of the junction boxes, and Figure 2.1e shows a view of the hole for capillary insertion into the junction box.

For this work, we used the Elegoo Mars, which is a low cost consumer 3D printer that can be purchased for under $200 USD. This makes the manufacturing of our platform very cheap and accessible, as no expensive equipment or laborious procedures are required. The Elegoo Mars uses masked stereolithography (MSLA) printing, which means that it exposes a photocurable resin to light layer by layer to print components. MSLA printing can print features at a much higher resolution than the more common fused deposition modelling (FDM) printing, which uses a heated nozzle to extrude and melt thermoplastic filaments and deposit them layer by layer to print components. This allowed us to manufacture junction boxes with inlet and outlet holes small enough to hold and seal capillaries with an OD as low as 0.33 mm. 3D printed parts often have imperfections and surfaces that are not smooth because they are manufactured with additive layers. These imperfections persist in components moulded from the 3D printed parts. A soft elastomeric material was thus required to create a seal between the junction boxes and the capillaries. We used Vytaflex 30 polyurethane to cast the junction boxes, which has a 30A shore hardness. This low hardness enables sealing around the capillaries despite imperfections present on the surface of the junction boxes. We were able to achieve consistent seals and no leakage around all capillaries without the need for any adhesives or machined gaskets.

Figure 2.1f shows a representative completed assembly of the modular microcapillary platform. To demonstrate the versatility of the platform, we used it to form several different types of emulsions: multicompartmental O/O/W double emulsions, multicompartmental W/O/W double emulsions, multicompartmental O/W/O double emulsions, and multicompartmental W/O/W double emulsions with two types of inner droplets (binary multicompartmental double emulsions). More complex emulsions may be formed using our platform such as ternary multicompartmental emulsions by adding more inner capillaries. However, this will increase the required size of middle and outer capillaries, which may make droplet formation unstable. Though the droplet images shown here appear 2-dimensional, the inner droplets do display a 3-dimensional configuration (see ESI for side view images). In each case, we tested a minimum of three different devices. On average we are capable of generating 1 double emulsion per second, though this number is subject to change depending on the composition of the double emulsion itself (monocompartmental double emulsions are generated more rapidly than decacompartmental double emulsions). Droplet size can also be changed by changing the flow rates with respect to each other. For example, for smaller inner phase droplets, the inner phase flow rate can either be decreased relative to the middle phase flow rate, or vice versa. For each type of double emulsion, the inner and middle flow rate ratios were kept constant.

2.3.1 Water-in-oil-in-water (W/O/W) multicompartmental double emulsion generation

As shown in Figure 2.2a, W/O/W multicompartmental double emulsions were generated using glass capillaries for the inner and outer phases, and a PTFE capillary for the middle phase (Table 2.1). The inner phase was water stabilised with sodium dodecyl sulfate (SDS), which was encapsulated in oil (FC-40 stabilised with 1H,1H,2H,2H-

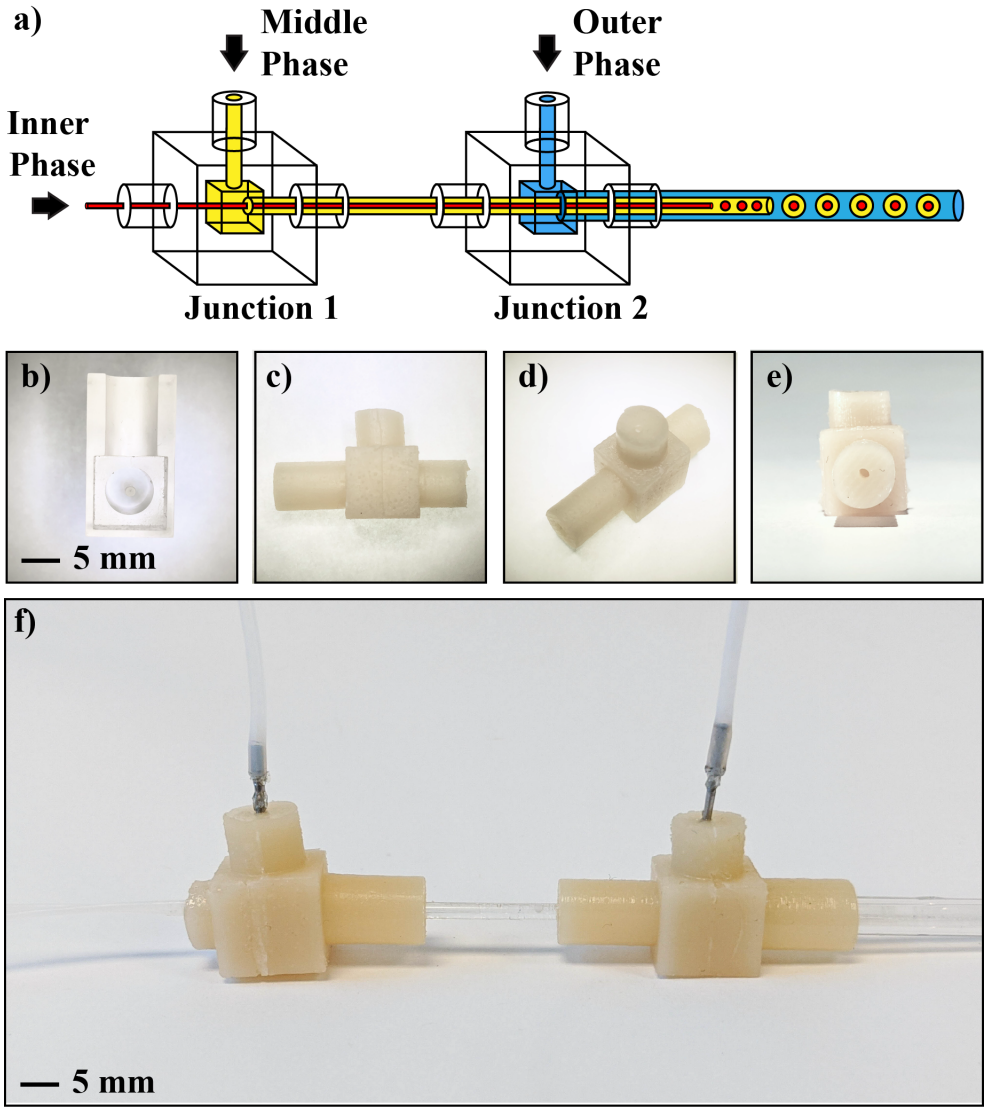

Figure 2.1: **Modular microcapillary platform for multicompartmental double emulsion formation**. a) Diagram of the assembled modular microcapillary platform for multicompartmental double emulsion formation. The platform is comprised of two junction boxes (Junction 1 and Junction 2) which are cast from a flexible resin using 3D printed moulds. They are used to link the capillaries together and seal them to prevent leakage. Junction box 1 holds the capillaries for the inner (red) and middle (yellow) phases. The inner capillary is inserted into the inlet of junction box 1, crosses both junction boxes and exits the outlet of junction box 2. The middle phase capillary is inserted into the outlet of junction box 1 and exits the outlet of junction box 2. The outer capillary (blue) is inserted into the outlet of junction box 2. The middle phase is inserted from the top of junction box 1 and the outer phase is inserted from the top of junction box 2. The three capillaries are different lengths to enable the formation of the inner droplets (red) in the middle phase (yellow), and then the outer droplets in the outer phase (blue) in the outer capillary. Diagram not to scale. b) One of the 3D printed moulds used to cast the junction boxes, which contains a projection designed to fit the required capillary. c) and d) Side and top views, respectively, of a junction box. The protrusion on the left allows the insertion of PTFE tubing or glass capillaries, and the protrusion on the top allows for the insertion of the middle and outer phases through a blunted metal syringe tip. e) Shows a front view of one of the protrusions though which a capillary is inserted into the junction box. The scale bar is constant for images b to e. f) Shows the assembled modular microcapillary platform configured for the formation of W/O/W multicompartmental double emulsions.

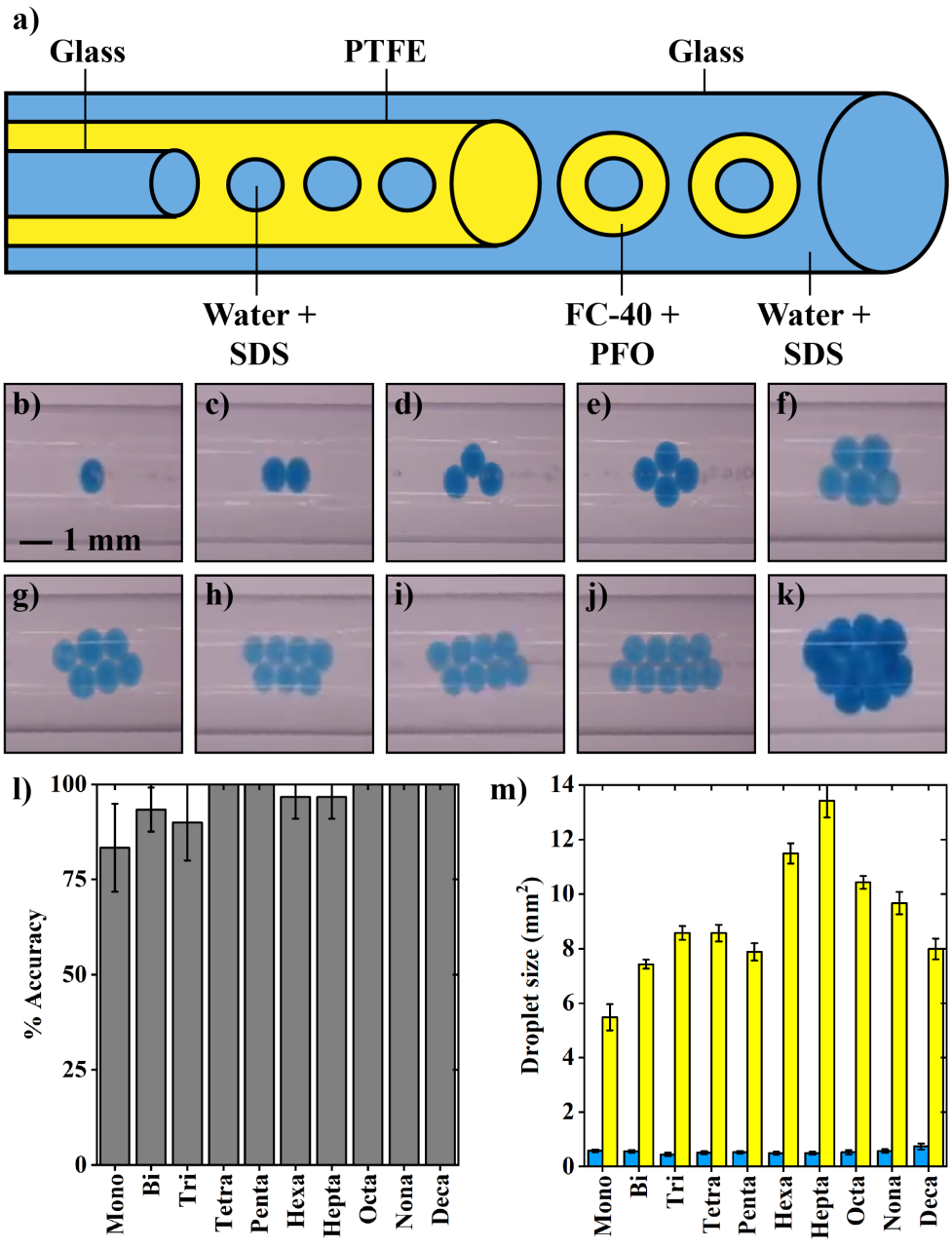

Figure 2.2: **Formation of water-in-oil-in-water (W/O/W) multicompartmental double emulsions.** a) Diagram showing the composition of the modular microcapillary platform and of the multicompartmental droplets. For W/O/W multicompartmental double emulsion formation, the inner and outer capillaries were glass and the middle capillary was PTFE. The inner phase was water with SDS and blue dye to aid visualisation (blue), the middle phase was FC-40 with PFO (yellow), and the outer phase was water with SDS (blue). b-k) Microscopy images of the W/O/W mono-, bi-, tri-, tetra-, penta-, hexa-, hepta-, octa-, nona- and deca-compartmental double emulsions generated with the modular microcapillary platform. l) Graph showing the accuracy of encapsulation as a function of the multicompartmental double emulsion composition (n = 30 for each droplet type). Error bars show the standard deviation. m) Droplet size analysis for each type of multicompartmental double emulsion. In each case, the outer droplet is shown in yellow and the inner droplets are shown in blue. (n = 10 for yellow data, n = 10-100 for blue data). Error bars show the standard deviation.

perfluoro-1-octanol, PFO), which in turn was encapsulated in water stabilised with SDS. Alteration of the flow rates allowed for precise control of multicompartmental double emulsion generation with a varying number of inner droplets. Figure 2.2b-k shows representative images of mono-, bi-, tri-, tetra-, penta-, hexa-, hepta-, octa-, nona- and deca-compartmental double emulsions generated using this configuration of the modular microcapillary platform. We found that starting with an outer flow rate of 2000 $\pm$ 100 μLmin^{-1}, a middle flow rate of 200 $\pm$ 10 μLmin^{-1}, and an inner flow rate of 20 $\pm$ 5 μLmin^{-1} we were consistently able to generate deca-compartmental double emulsions. The outer flow rate could then be sequentially increased by 250 $\pm$ 50 μLmin^{-1} to generate higher shear forces and thus multicompartmental double emulsions with progressively smaller numbers of inner droplets. A video showing W/O/W tetra-compartmental double emulsions is provided in the Electronic Supplementary Information (ESI).

Quantification of the performance of the modular microcapillary platform for the formation of W/O/W multicompartmental double emulsions was performed by analysis of both accuracy of encapsulation and droplet size. Figure 2.2l shows how often we were able to achieve the required number of inner droplets for each type of multicompartmental double emulsion. We were able to generate multicompartmental double emulsions with an accuracy of between 83-100%, depending on the number of inner droplets encapsulated. Figure 2.2m shows the size of both the inner (blue) and outer (yellow) droplets for each type of multicompartmental double emulsion. The size variation is small, with the outer droplet size generally increasing as the number of inner droplets encapsulated increases. These results suggest that our modular microcapillary platform can form a variety of W/O/W multicompartmental double emulsions with a high degree of accuracy and low size variation in both the inner and outer droplets.

2.3.2 Oil-in-water-in-oil (O/W/O) multicompartmental double emulsion generation

As shown in Figure 2.3a, O/W/O multicompartmental double emulsions were generated using glass capillaries for the inner and middle phases, and a PTFE capillary for the outer phase (Table 2.1). The inner phase was oil (FC-40 stabilised with PFO), which was encapsulated in water stabilised with SDS, which in turn was encapsulated in oil (FC-40 stabilised with PFO). As for W/O/W multicompartmental double emulsions, alteration of the flow rates allowed for precise control of multicompartmental double emulsion generation with a varying number of inner droplets. Figure 2.3b-k shows representative images of mono- to deca-compartmental double emulsions generated using this configuration of the modular microcapillary platform. We found that starting with an outer flow rate of 1000 $\pm$ 100 μLmin^{-1}, a middle flow rate of 500 $\pm$ 50 μLmin^{-1}, and an inner flow rate of 200 $\pm$ 20 μLmin^{-1}, we were consistently able to generate deca-compartmental double emulsions. The outer flow rate could then be sequentially increased by 250 $\pm$ 50 μLmin^{-1} to generate multicompartmental double emulsions with progressively smaller numbers of inner droplets. A video showing O/W/O tetra-compartmental double emulsions is provided in ESI.

Quantification of the performance of the modular microcapillary platform for the formation of O/W/O multicompartmental double emulsions was performed by analysis of both accuracy of encapsulation and droplet size. Figure 2.3l shows how often we were able to achieve the required number of inner droplets for each type of multicompartmental double emulsion. We were able to generate multicompartmental double emulsions with an accuracy of 95-100% for mono- to nona-compartmental double emulsions and 87% for the largest amount of inner droplets (deca-compartmental double emulsions). Figure 2.3m shows the size of both the inner (yellow) and outer

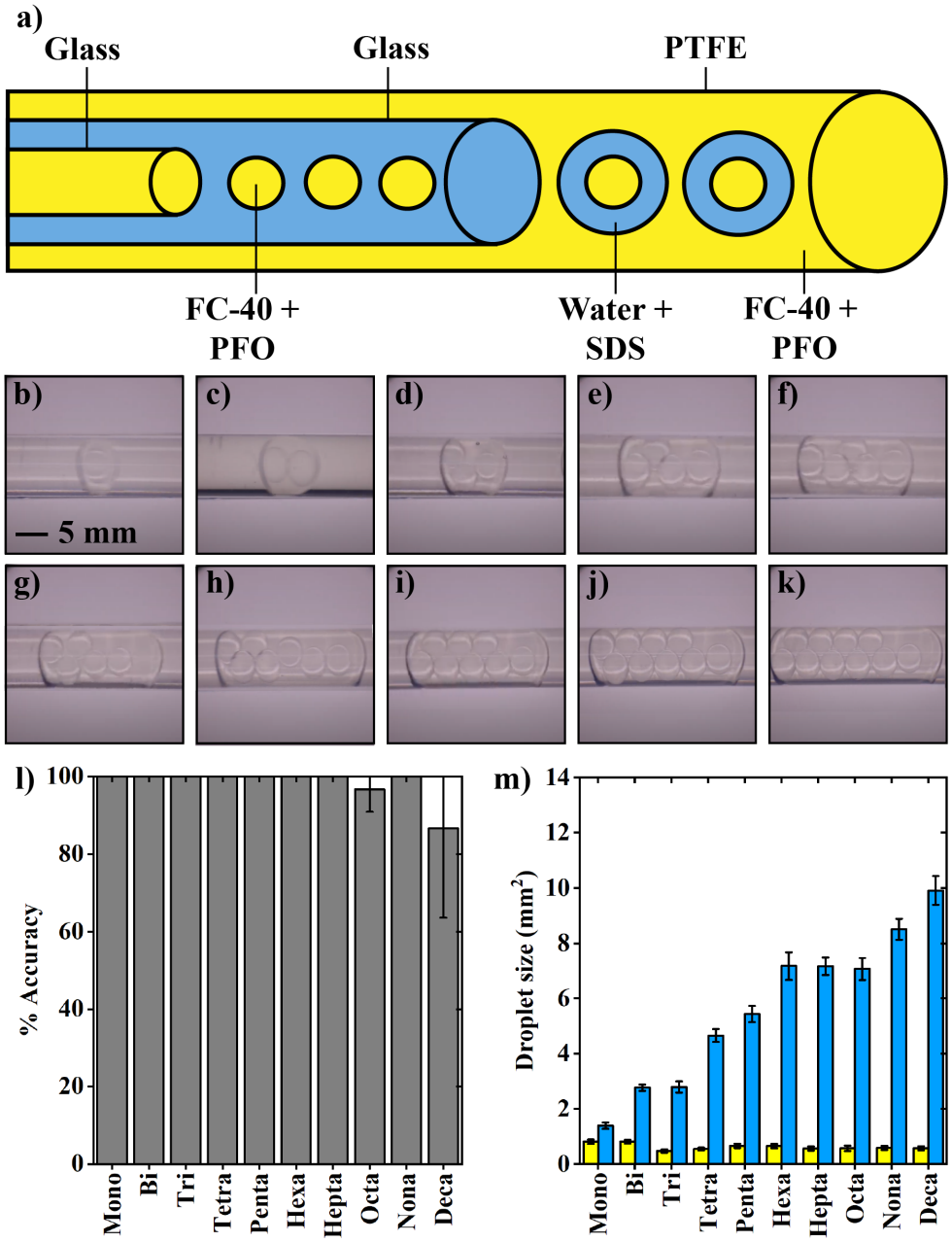

Figure 2.3: **Formation of oil-in-water-in-oil (O/W/O) multicompartmental double emulsions.** a) Diagram showing the composition of the modular microcapillary platform and of the multicompartmental droplets. For O/W/O multicompartmental double emulsion formation, the inner and middle capillaries were glass and the outer capillary was PTFE. The inner phase was FC-40 with PFO (yellow), the middle phase was water with SDS (blue), and the outer phase was FC-40 with PFO (yellow). b-k) Microscopy images of the O/W/O mono-, bi-, tri-, tetra-, penta-, hexa-, hepta-, octa-, nona- and deca-compartmental double emulsions generated with the modular microcapillary platform. l) Graph showing the accuracy of encapsulation as a function of the multicompartmental double emulsion composition (n = 30 for each droplet type). Error bars show the standard deviation. m) Droplet size analysis for each type of multicompartmental double emulsion. In each case, the outer droplet is shown in blue and the inner droplets are shown in yellow. (n = 10 for blue data, n = 10-100 for yellow data). Error bars show the standard deviation.

(blue) droplets for each type of multicompartmental double emulsion. The size variation is small, with the outer droplet size increasing as the number of inner droplets encapsulated increases. These results suggest that our modular microcapillary platform can form a variety of O/W/O multicompartmental double emulsions with a very high degree of accuracy and low size variation in both the inner and outer droplets.

2.3.3 Oil-in-oil-in-water (O/O/W) multicompartmental double emulsion generation

As shown in Figure 2.4a, O/O/W multicompartmental double emulsions were generated using three different sizes of glass capillaries (Table 2.1). The inner phase was oil (FC-40), which was encapsulated in another oil (mineral oil), which in turn was encapsulated in water stabilised with SDS. Alteration of the flow rates allowed for precise control of multicompartmental double emulsion generation with a varying number of inner droplets. Figure 2.4b-k shows representative images of mono- to deca-compartmental double emulsions generated using this configuration of the modular microcapillary platform. We found that starting with an outer flow rate of 300 $\pm$ 30 μLmin^{-1}, a middle flow rate of 200 $\pm$ 20 μLmin^{-1} and an inner flow rate of 80 $\pm$ 10 μLmin^{-1} we were consistently able to generate deca-compartmental double emulsions. The outer flow rate could then be sequentially increased by 100 $\pm$ 20 μLmin^{-1} to generate multicompartmental double emulsions with progressively smaller numbers of inner droplets. A video showing O/O/W tetra-compartmental double emulsions is provided in ESI.

Quantification of the performance of the modular microcapillary platform for the formation of O/O/W multicompartmental double emulsions was performed by analysis of both accuracy of encapsulation and droplet size. Figure 2.4l shows how often we

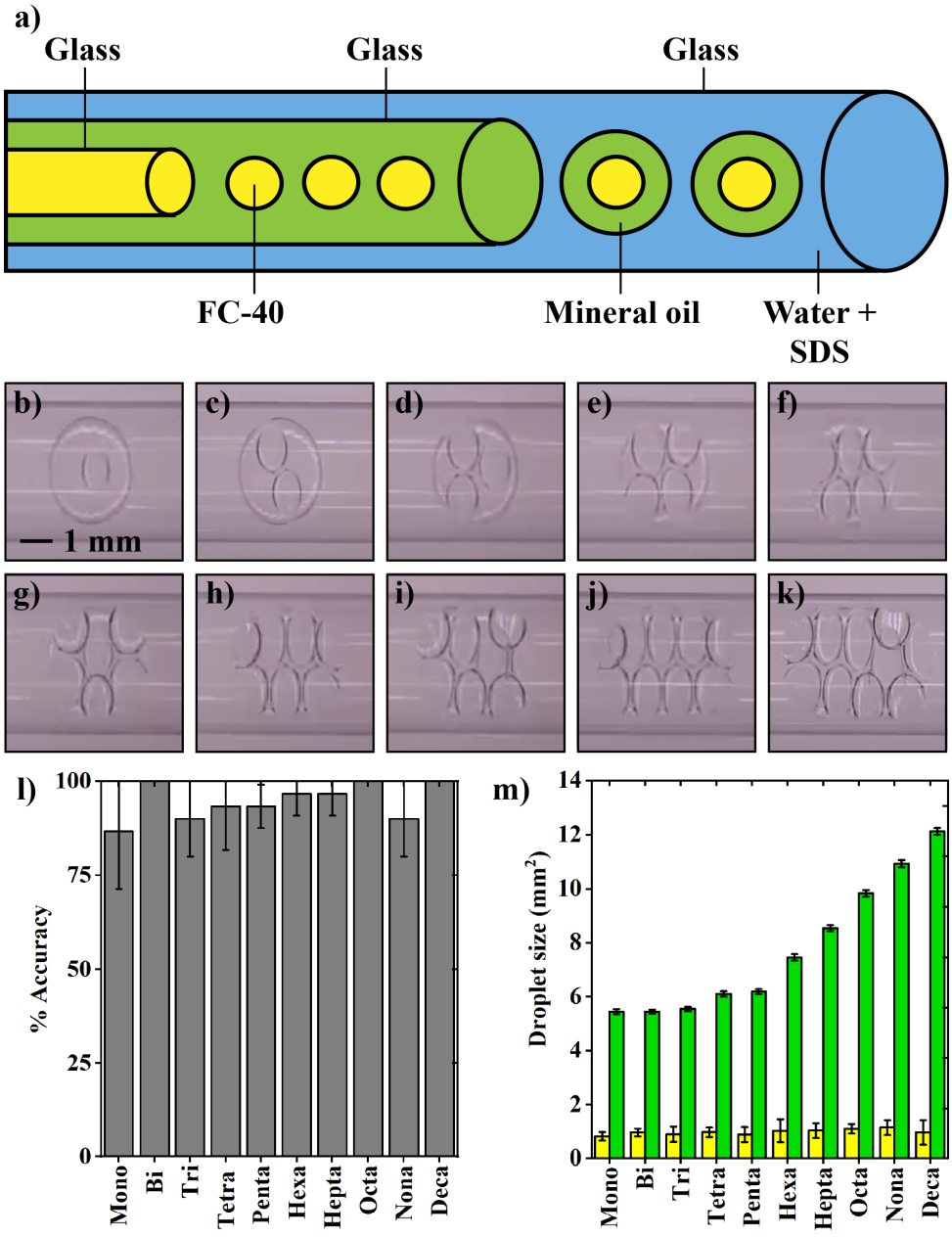

Figure 2.4: **Formation of oil-in-oil-in-water (O/O/W) multicompartmental double emulsions.** a) Diagram showing the composition of the modular microcapillary platform and of the multicompartmental droplets. For O/O/W multicompartmental double emulsion formation, all capillaries were glass. The inner phase was FC-40 (yellow), the middle phase was mineral oil (green) and the outer phase was water with SDS (blue). b-k) Microscopy images of the O/O/W mono-, bi-, tri-, tetra-, penta-, hexa-, hepta-, octa-, nona- and deca-compartmental double emulsions generated with the modular microcapillary platform. l) Graph showing the accuracy of encapsulation as a function of the multicompartmental double emulsion composition (n = 30 for each droplet type). Error bars show the standard deviation. m) Droplet size analysis for each type of multicompartmental double emulsion. In each case, the outer droplet is shown in green and the inner droplets are shown in yellow. (n = 10 for green data, n = 10-100 for yellow data). Error bars show the standard deviation.

were able to achieve the required number of inner droplets for each type of multicompartmental double emulsion. We were able to generate multicompartmental double emulsions with an accuracy of between 87-100%, depending on the number of inner droplets encapsulated. Figure 2.4m shows the size of both the inner (yellow) and outer (green) droplets for each type of multicompartmental double emulsion. The size variation is small, with the outer droplet size increasing as the number of inner droplets encapsulated increases. These results suggest that our modular microcapillary platform can form a variety of O/O/W multicompartmental double emulsions with a high degree of accuracy and low size variation in both the inner and outer droplets.

2.3.4 Binary water-in-oil-in-water (W/O/W) multicompartmental double emulsion generation

Figure 2.5a shows the overall platform for the formation of binary W/O/W multicompartmental double emulsions, where two different inner phases are used to generate droplets of different compositions. The binary multicompartmental double emulsions are still formed using coaxial flow of the four phases in the outlet capillary. However, in this case, two inner phase capillaries are inserted the whole way through the platform from the inlet of the first junction box until they exit the second junction box.

As shown in Figure 2.5b, binary W/O/W multicompartmental double emulsions were generated using PTFE capillaries for both of the inner and the middle phases, and a glass capillary for the outer phase (Table 2.1). The inner phases were water stabilised with SDS and dyes were added to enable visualisation of each type of inner phase droplet. These inner droplets were encapsulated in oil (FC-40 stabilised with PFO),

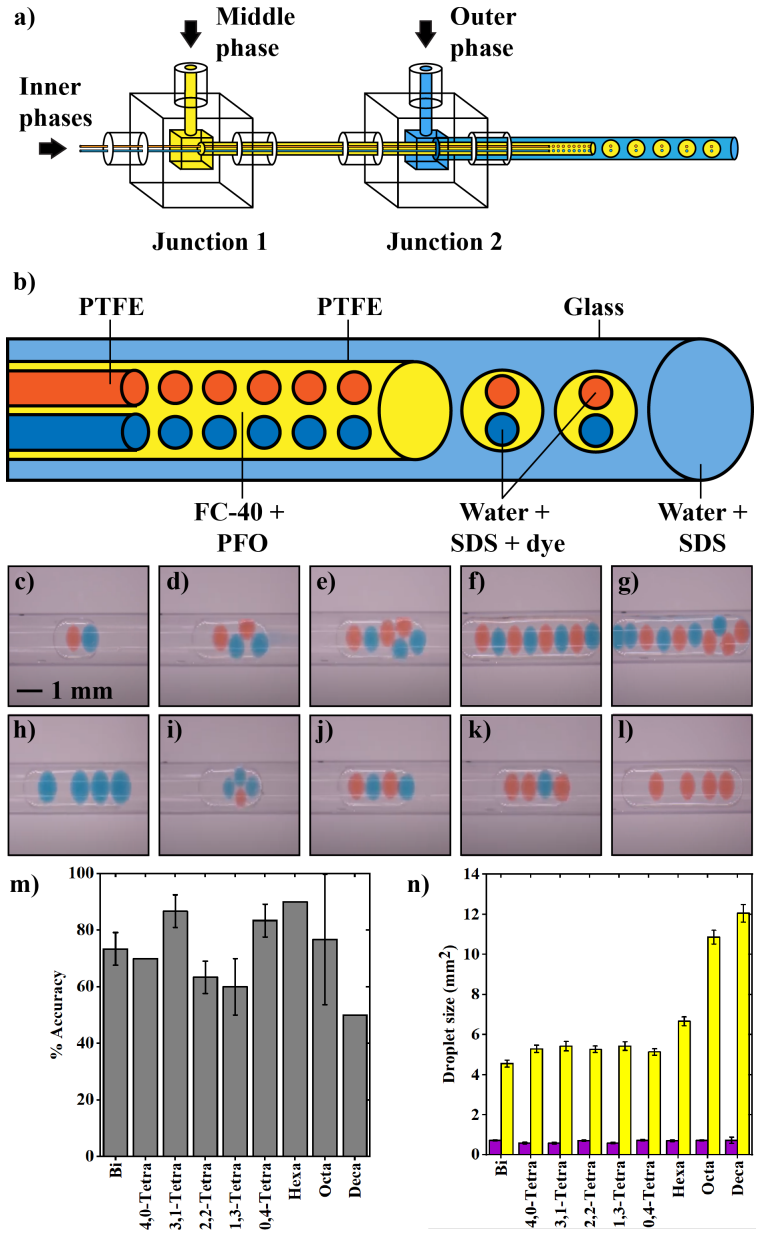

Figure 2.5: **Modular microcapillary platform for binary W/O/W multicompartmental double emulsion formation**. a) Diagram of the assembled modular microcapillary platform for binary W/O/W multicompartmental double emulsion formation. The platform is the same as in Figure 2.1a, except that two inner capillaries are inserted into each of the two holes in the inlet of Junction 1 to form the two types of inner droplets. Diagram not to scale. b) Diagram showing the composition of the modular microcapillary platform and of the binary multicompartmental droplets. For binary W/O/W multicompartmental double emulsion formation, the inner and middle capillaries were PTFE and the outer capillary was glass. The inner phases were water with SDS, the middle phase was FC-40 with PFO, and the outer phase was water with SDS. The inner phases were dyed for ease of visualisation. c-g) Microscopy images of the binary population of W/O/W bi-, tetra-, hexa-, octa- and deca-compartmental double emulsions generated with the modular microcapillary platform, where half of the inner droplets are red, and half are blue. h-l) Microscopy images of binary W/O/W tetra-compartmental double emulsions showing all possible combinations of inner droplets (4,0-, 3,1-, 2,2-, 1,3-, and 0,4-tetra-compartmental double emulsions respectively) generated with the modular microcapillary platform, where the number on the left denotes the number of blue droplets and the number on the right denotes the number of red droplets. m) Graph showing the accuracy of encapsulation as a function of the multicompartmental double emulsion composition (n = 30 for each droplet type). Error bars show the standard deviation. n) Droplet size analysis for each type of multicompartmental double emulsion. In each case, the outer droplet is shown in yellow and the inner droplets are shown in purple. (n = 10 for yellow data, n = 10-100 for purple data). Error bars show the standard deviation.

which in turn were encapsulated in water stabilised with SDS. Alteration of the flow rates allowed for precise control of multicompartmental double emulsion generation with a varying number of inner droplets. Figure 2.5c-g shows representative images of bi-, tetra-, hexa-, octa- and deca-compartmental W/O/W double emulsions with equal numbers of each type of inner droplet generated using this configuration of the modular microcapillary platform. In the same manner as we generated W/O/W multicompartmental double emulsions, we found that starting with an outer flow rate of 2000 ± 200 μLmin^{-1}, a middle flow rate of 200 ± 20 μLmin^{-1}, and inner flow rates for each inner phases of 50 ± 10 μLmin^{-1}, we were consistently able to generate deca-compartmental double emulsions with equal numbers of each type of inner droplet. The outer flow rate could then be sequentially increased by 200 ± 50 μLmin^{-1} to generate binary W/O/W multicompartmental double emulsions with progressively smaller numbers of inner droplets.

Figure 2.5h-l shows representative images of all types of binary W/O/W tetra-compartmental double emulsions it is possible to form. As shown previously[126], in order to specify the droplet type for each of the inner droplets two numerical prefixes are added: the first number denotes the number of blue inner droplets and the second number denotes the number of red inner droplets. For example, a tetra-compartmental double emulsion with one blue droplet and three red inner droplets is a 1,3-tetra-compartmental double emulsion. Hence, Figure 2.5h-l shows W/O/W 4,0-, 3,1-, 2,2-, 1,3- and 0,4-tetra-compartmental double emulsions respectively. In order to vary the ratio of blue to red inner droplets the inner phase flow rates were varied with respect to each other. Starting with the flow rates described above for an equal ratio of red to blue inner droplets, the total flow rate for the inner phases is kept the same, but the ratio between the flow rates is set to match the required ratio between the inner droplets. For example, if we start with a flow rate of 50 μLmin^{-1} for both

the inner phases (100 μLmin^{-1} total flow rate), increasing the flow rate of the blue inner phase to 75 μLmin^{-1} and decreasing the flow rate of the red inner phase to 25 μLmin^{-1} would generate a 3,1-tetra-compartmental double emulsion. A video showing W/O/W 3,1-tetra-compartmental double emulsions is provided in ESI.

Quantification of the performance of the modular microcapillary platform for the formation of binary W/O/W multicompartmental double emulsions was performed by analysis of both accuracy of encapsulation and droplet size. In each case, data are provided for W/O/W 1,1-bi-, 3,3-hexa-, 4,4-octa- and 5,5-deca-compartmental double emulsions and for all combinations of W/O/W tetra-compartmental double emulsions (4,0-, 3,1-, 2,2-, 1,3- and 0,4-). Figure 2.5m shows how often we were able to achieve the required number of inner droplets for each type of binary multicompartmental double emulsion. We were able to generate binary multicompartmental double emulsions with an accuracy of between 60-90%, depending on the number and type of inner droplets. We have found that as the complexity of the system increases (i.e. more types of inner droplets are used), the accuracy decreases. In single inner capillary systems, there are errors associated with the number of inner droplets, but in the double inner capillary system, there are errors associated with the number of inner droplets but also with type of the inner droplets. Hence the "accuracy" of this system is lower. Figure 2.5n shows the size of both of the inner (purple) droplets and the outer (yellow) droplets for each type of binary multicompartmental double emulsion. The size variation is small, with the outer droplet size increasing as the number of inner droplets encapsulated increases, and constant for all combinations of tetra-compartmental double emulsions. These results suggest that our modular microcapillary platform can form a variety of binary W/O/W multicompartmental double emulsions with a good degree of accuracy and low size variation in both the inner and outer droplets.

2.4 Conclusions

We have developed a simple and modular plug-and-play microcapillary platform for the formation of multicompartmental double emulsions with between 1 and 10 inner droplets of the same or different composition. We use a low-cost 3D printer to generate junction boxes from a flexible resin that provide quick manual alignment of the capillaries without leaking. We can use any type of glass or PTFE capillary, which means that no surface treatment is required. These capillaries can be swapped out of the reusable junction boxes to form W/O/W, O/W/O, O/O/W or binary W/O/W multicompartmental double emulsions. Our device poses several notable advantages over the current state of the art: it does not require any expensive equipment or laborious procedures to manufacture, the co-flow regime eliminates the need for capillary alignment, the unique combination of hydrophilic glass and hydrophobic PTFE capillaries negates the need to perform surface modification, and the use of a flexible polyurethane resin to form junction boxes for the capillaries removes the need for gaskets or adhesives to create a seal. This means that our modular microcapillary platform is able to be used by anyone with access to a benchtop 3D printer and syringe pumps, regardless of microfluidic expertise.

Chapter 3

Development of a microfluidic platform for the generation of proteinosome synthetic cells

Here I show the methodological development of a microfluidic platform for the creation of polymeric proteinosomes from double emulsions as a step towards the generation of prototissues (shown in Chapter 5).

Aside from the design shown in Figure 3.2a, which was initially worked on by undergraduate student Janel Gaube, all of the data, analysis and writing in this chapter are my own. Dr Gobbo (University of Bristol, UK) provided the BSA nanoconjugate.

3.1 Introduction

Proteinosomes are a type of synthetic cell which are defined by their semi-permeable, enzymatically active, stimulus-responsive, elastic membrane that is made of a closely

packed monolayer of interconnected protein–polymer building blocks. The applications of these proteinosomes are not limited to evolutionary biology;[41,127–129] they also have applications in biochemical catalytic reactions,[24,25] protein synthesis,[26,27] and medicine (for drug delivery and development).[10,21–23]

Our collaborator, Dr Pierangelo Gobbo (University of Bristol, UK), recently published a procedure[78] which allowed for the interconnection of individual proteinosomes to form prototissues. As shown in Figure 3.1a, they synthesized a new bovine serum albumin (BSA)/poly(N-isopropylacrylamide)-co-methacrylic acid (BSA/PNIPAM-co-MAA) nanoconjugate and functionalised it with either pendant azide or bicyclononyne (BCN) moieties (Figure 3.1b). The amphiphilic bio-orthogonally reactive protein-polymer nanoconjugates were then used to prepare two separate populations of azide- or BCN-functionalised proteinosomes as water-in-oil (W/O) droplets where the protein-polymer nanoconjugate particles were adsorbed at the interface between the two phases (Figure 3.1c, d and e). The proteinosome structures were stabilised *via* chemical crosslinking with PEG-diNHS. The crosslinked azide- and BCN-functionalised proteinosomes were then spatially confined as water-in-oil-in-water (W/O/W) Pickering emulsions (Figure 3.1c). Removal of the oil phase *vi*a dialysis triggered the interfacial strain-promoted alkyne-azide cycloaddition (I-SPAAC) between the complementary reactive proteinosomes (i.e. click chemistry between the alkyne and azide elements) with consequent generation of an interlinked synthetic tissue (prototissues). However, the initial proteinosome populations were highly polydisperse (of unequal size and composition) which posed a significant problem when analyzing their functionality without confounding variables. Work by Ugrinic *et al.* has shown that PDMS microfluidic devices can be used to support a monodisperse double emulsification technique with the same biological components (i.e proteins such as BSA).[41] Hence, we presumed that the issues that arose in the work by Gobbo *et al.* could be

addressed using microfluidic techniques.

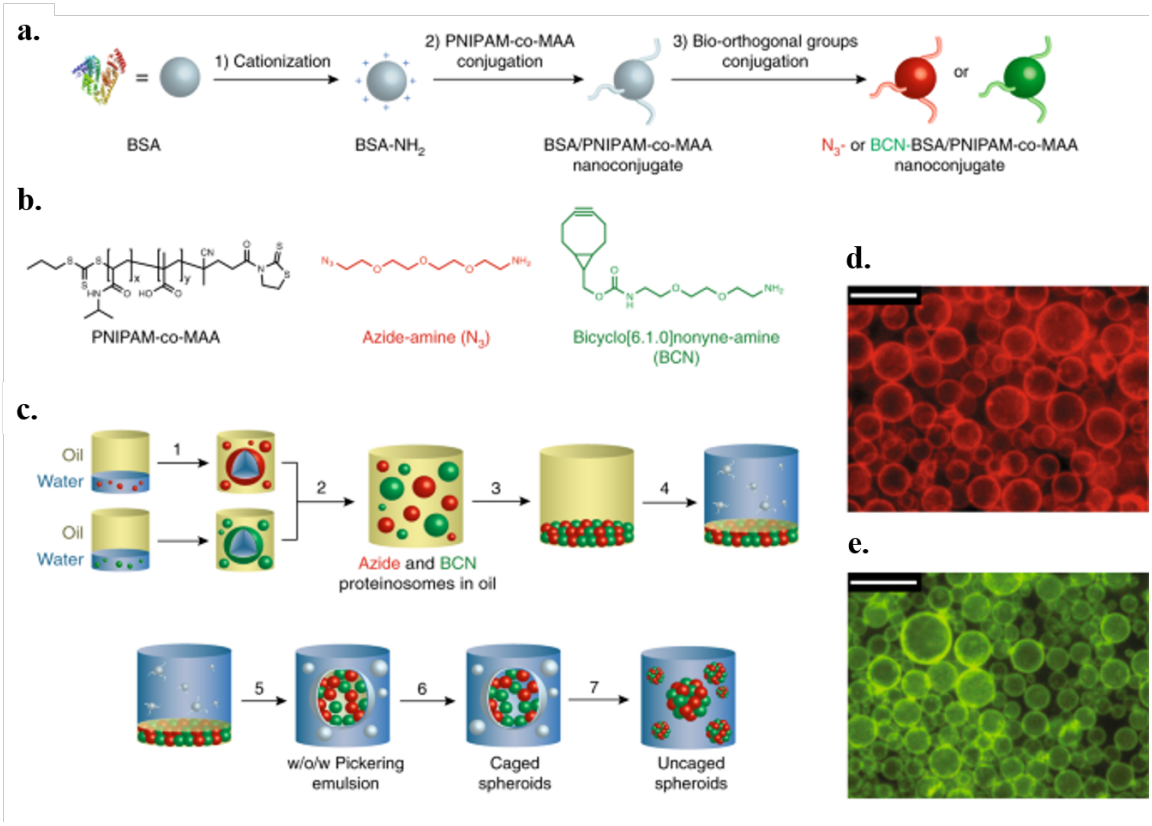

Figure 3.1: **Programmed assembly of proteinosomes into synthetic prototissues.** a, Synthetic pathway for the preparation of protein–polymer nanoconjugates with bio-orthogonal functionalities. b, Molecular structures of the activated copolymer and bio-orthogonal prosthetic groups (azide-amine (N_3); bicyclo[6.1.0]nonyne-amine (BCN)). c, Scheme showing experimental procedure for the preparation of proteinosome-based prototissues. d-e, Fluorescence optical microscopy images showing single populations of rhodamine isothiocyanate (RITC)- and fluorescein isothiocyanate (FITC)-labelled azide- and alkyne-functionalized proteinosomes in oil. Scale bars = 50 μm. Image reproduced from Gobbo *et al.*[78] with permission.

The following chapter details the development of a double emulsion polydimethylsiloxane (PDMS) microfluidic platform for use in generating mono- and bi-populations of proteinosomes using double emulsions. Here I show the evolution in the design of my microfluidic devices, as well as their surface treatment. I also quantify the statistical performance of my final device and show the formation of interconnected proteinosomes. Lastly, I demonstrate how my microfluidic platform development carries over into a microfluidic platform for the creation of more complex prototissue (Chapter 5).

3.2 Results and discussion

3.2.1 Platform fabrication and optimization

The first step in the microfluidic generation of these bio-engineered proteinosomes involved the development of a simple PDMS microfluidic device which supported biological material without contamination. Despite a wide variety of different multi-compartmental double emulsion platforms described in the literature, there is no consensus on an optimal design for stable droplet formation[130]. Moreover, double emulsions generated *via* microfluidic devices are not often statistically quantified; this brings to question the validity of the results reported in the literature. As a result, I found that significant iterative redesign was required in order to generate an accurate, reproducible, and reliable device. Figure 3.2 illustrates the evolution of designs for my proteinosome generation device. I tested all of these devices using a W/O/W mixture prior to testing with biological materials. The inner aqueous phase contained only water, the middle phase contained 2.5% Pico-Surf (surfactant) in FC-40 (oil), and the outer phase contained a mixture of water and 0.5 % sodium dodecyl sulfate (SDS, surfactant).

My microfluidic device underwent several design iterations before I was able to produce a functional double emulsion device (Figure 3.2). All devices contained at least 3 inlets (where the inner [rightmost inlet], middle [middle inlet] and outer [leftmost inlet] solutions went into the device) and at least one outlet (where the double emulsion droplets exited). All devices also contained two junctions; both junctions are where the channels meet in a cross-like shape and where the continuous phase breaks up the disperse phase into droplets. Junction 1 is on the left and is where the inner phase droplets are formed by the middle phase and Junction 2 is on the right and is where the middle phase droplets (containing inner phase droplets) are formed (junctions

depicted in Figure 3.2b). Design **a**, was modelled on the simplest platform that could be found in the literature.[131] It consisted of three inlets and one outlet. All of the channel dimensions are 50 μm across the design. There are also no meanders (curved channels), which are generally used for additional stabilization and visualization. The meanders make the droplets take more time to leave the microfluidic device which gives more time to see them. I found that this design produced unstable droplets with a limited visualization time for droplet formation. Design **b** attempted to mitigate these issues by extending the channel lengths by 10000 μm and adding a wide chamber that would slow down the droplet speed. The increased width of the chamber (by 5000 μm) slowed the droplet velocity in accordance with the Hagen–Poiseuille flow equation. Though visualization was easier due to the decreased droplet velocity, the droplets formed were still unstable and the chamber caused the droplets to merge together. This is because the decrease in droplet speed causes them to touch before allowing them enough time to become stable. Design **c** incorporated progressively increasing channel sizes. The inner phase channels were 25 μm, the middle phase channels were 50 μm and the outer phase channels were 100 μm. Meanders were also incorporated in order to increase the time that droplets were on the device; this facilitated droplet visualization. This design additionally used optional exit outlets; the first is situated before the double emulsion formation junction and was designed to remove excess oil in an attempt to stabilize the click-chemistry detailed by Gobbo *et al.*[78]; a feature which we may have later needed. The second optional exit outlet was placed prior to the teardrop-shaped chamber and could potentially be used to remove excess droplets from the device in case of droplet merging. By design **d**, I eschewed the use of a chamber. I found that the chamber, though it slowed the droplets down for visualization, often resulted in unwanted droplet merging. Instead, the focus of this design was on the progressive increase in channel dimensions. Moreover, a me-

ander could be used to increase visualization time on-chip in the place of a chamber and was not subject to the same slowing which results in merging. Ultimately, the final increase in channel width by a factor of four (to 400 μm) in the second meander was deemed unnecessary as the first meander was sufficient for droplet visualization. Design **e** scaled up the overall channel widths by a factor of ten (250 μm for the inner phase channels, 500 μm for the the middle phase channels and 1000 μm for the outer phase channels) in an attempt to create multi-compartmental double emulsions containing a greater number of inner droplets. Ultimately, the channel widths were not deemed to be as important to the size of the emulsions as the flow rate ratios. For example, in order to make a deca-compartmental double emulsion one simply needed to decrease the outer flow rate relative to the middle flow rate rather than using larger channels. Design **f** contained a slight increase in channel dimensions by a factor of two (50 μm for the inner phase channels, 100 μm for the middle phase channels and 200 μm for the outer phase channels), to increase the flow velocity and minimize these droplet sticking to the channels. These changes were not shown to make any perceivable difference. Design **g** involved the addition of a 45°angle to streamline and stabilise multi-compartmental double emulsion formation. The angle did not help with droplet formation as expected. Design **h** is the final design which was used for proteinosome generation. The final channel dimensions were 25 μm for the inner phase channels, 50 μm for the middle phase channels and 100 μm for the outer phase channels.

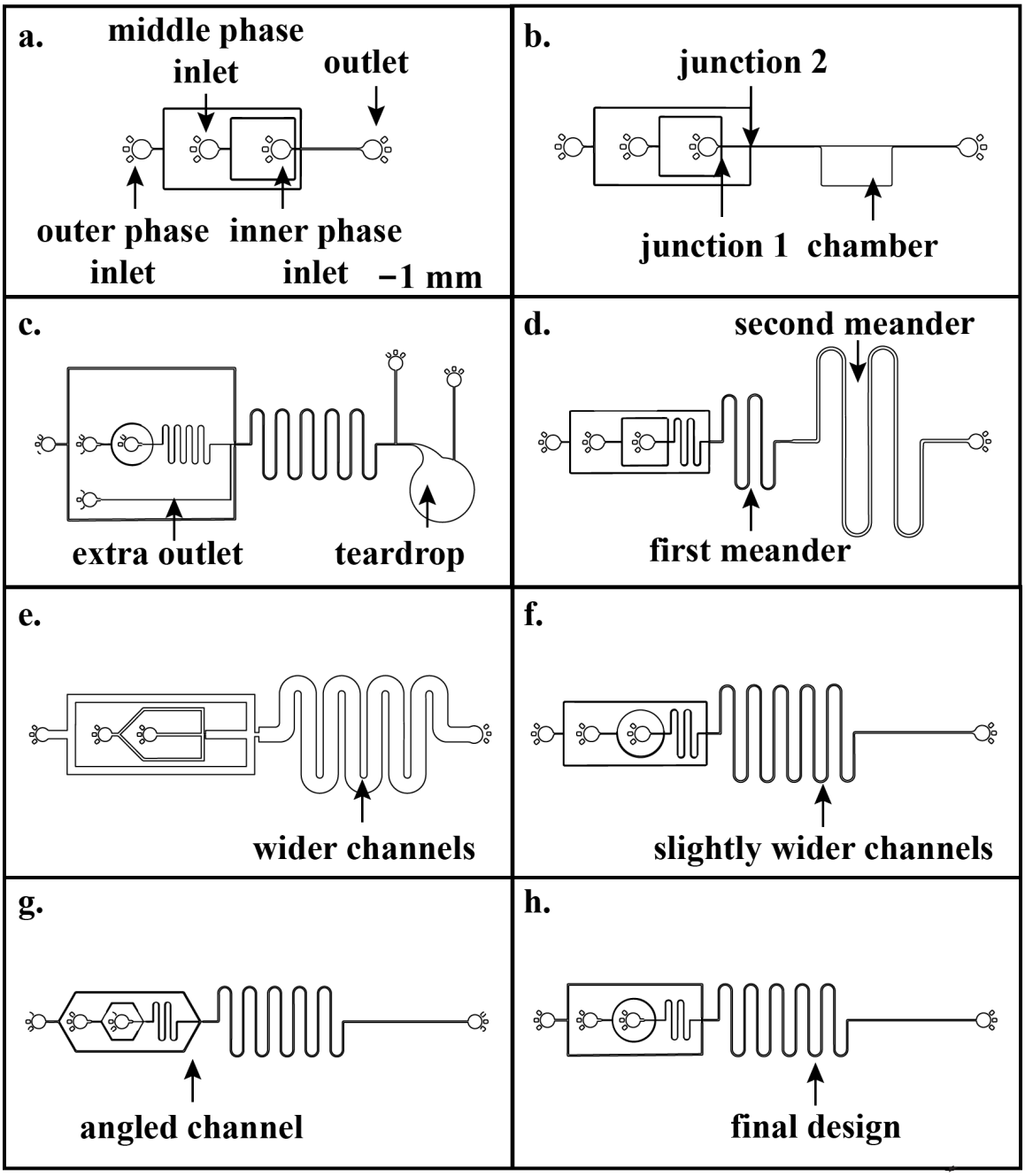

Figure 3.2: **Microfluidic device design evolution for the generation of proteinosomes.** Design **a** consisted of the most simplistic elements found in the literature for the generation of double emulsions. Design **b** added additional length after the second junction as well as a chamber in order to slow down the droplets. Design **c** employed a meander, in addition to the teardrop-shaped chamber. It also has an additional optional exit outlet added just prior to junction 2, the purpose of outlet is to remove excess oil. Design **d** involved the removal of the chambers and, instead, added an additional meander for additional visualization time. Design **e** involved the removal of the extra meander from **d** and the size of the channels were significantly increased in order to allow for an a greater encapsulation capacity. Design **f** combined elements of both d and e, in order to maximize double emulsion stability and encapsulation capacity. Design **g** was made in order to study the effects of different channel angles on the shear of the flow focusing junction. In the end, design **h** was deemed to be the most effective. Scale is 1 mm for all images.

3.2.2 Double emulsion generation

The most effective double emulsion generation device (design **h**) is pictured again in Figure 3.3. This design was deemed to be the most effective with its 90° flow focusing junction, two meanders, and channel dimensions increasing from 25 μm, to 50 μm, to 100 μm. In Figure 3.3b, the red-colored inlet denotes the inner water phase (MilliQ). The yellow colored inlet indicates the middle oil phase which consists of 2.5% PicoSurf (surfactant) w/w in FC-40. The blue-colored inlet indicates the outer water phase with an added 0.5 % w/w SDS as a surfactant. All device tests were done using these reagents as they are often used in the literature as a proof of concept for design functionality.[132] These solutions were pumped through the microfluidic device using 1 mL gastight glass syringes. These syringes were inserted into Aladdin syringe pumps. The syringes were then attached to the microfluidic device using PTFE tubing. The outer phase was set to 20 μL min^{-1}, the middle phase was set to 3 μLmin^{-1} and the inner phase was set to 1 μLmin^{-1}. As shown in Figure 3.3d, the results obtained using W/O/W solutions showed that this device can reliably produce mono-compartmental double emulsions. However, the middle phase of the double emulsions was unstable, which can be visualized by the darkened middle phase in Figure 3.3d. This foamy blackness indicated that there is some stickiness occurring when the hydrophillic phase was interacting with the hydrophobic PDMS surface. Hence, I began looking into different surface treatment options (described in detail in Appendix D) before I started device testing using biological materials which are stickier than our current system.

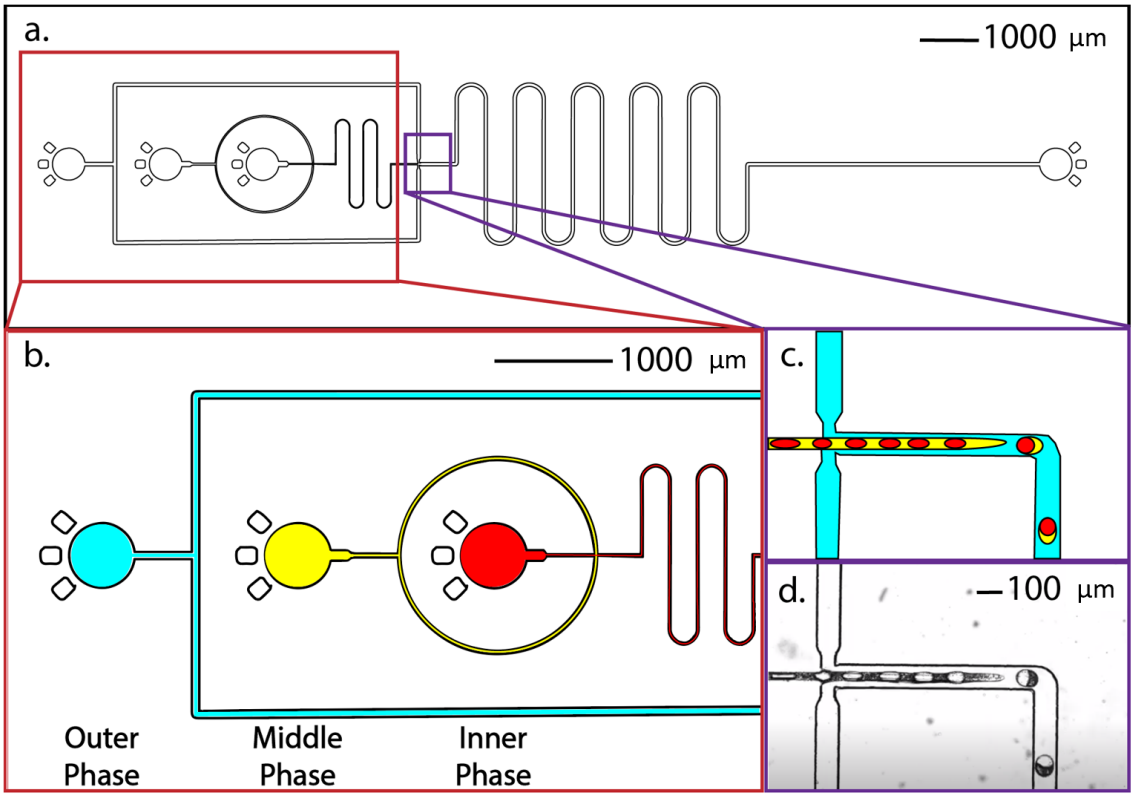

Figure 3.3: **Double emulsion generation.** a, The double emulsion device design which was generated using AutoCAD. b, Shows the zoomed-in region for droplet formation on the device. Blue denotes the outer aqueous phase, yellow denotes the middle oil phase and red denotes the inner aqueous phase. c, Depicts the formation of the double emulsions at the second junction with each color referring to the inlet from where the solution originated. d, Representative image of double emulsion formation on the device using a inner phase of water, a middle phase of a 2.5% PicoSurf w/w in FC-40 and an outer phase of water with added 0.5 w/w of SDS.

3.2.3 Double emulsion stabilization through surface treatment

Surface treatment of my PDMS microfluidic devices proved to be essential to generate protocells and prototissues. A significant amount of time was spent troubleshooting the procedure. For more detailed information on surface treatment development, please refer to Appendix D. The final iteration of my surface treatment procedure was based loosely on work from both Bauer *et al.*[132] and Trantidou *et al.*[133] and differed with respect to flow rates and device geometry. The polyvinyl alcohol (PVA) solution

was always prepared the day prior in order to give enough time for it's preparation. After having fabricated the PDMS devices, they were subjected to plasma treatment. After this they were bonded to spin coated PDMS coated glass slides. A 25 mL plastic syringe was filled with air and a 1 mL glass gastight glass syringe was filled with PVA solution. Two sealed PTFE plugs were placed into the two inner inlets (indicated by yellow and red colors in Figure 3.3). An exit tubing was placed at the first inlet (indicated in blue in Figure 3.3), the tube connecting the air-filled syringe was connected to the second inlet and lastly the PVA tube was connected to the outlet. The desired hydrophillic and hydrophobic regions of the device are indicated in light blue and light brown respectively in Figure 3.4a. As can be seen by the arrows in Figure 3.4b, the syringe pumps were used to push the air through the blue inlet and the PVA was manually pushed through the desired channels for approximately 10 min. The device was then dried using a filtered air gun and was placed on a hot plate for drying. The process was repeated twice more. The device was then placed in the oven overnight at 65°C. More details on this procedure are described in the Materials and Methods section.

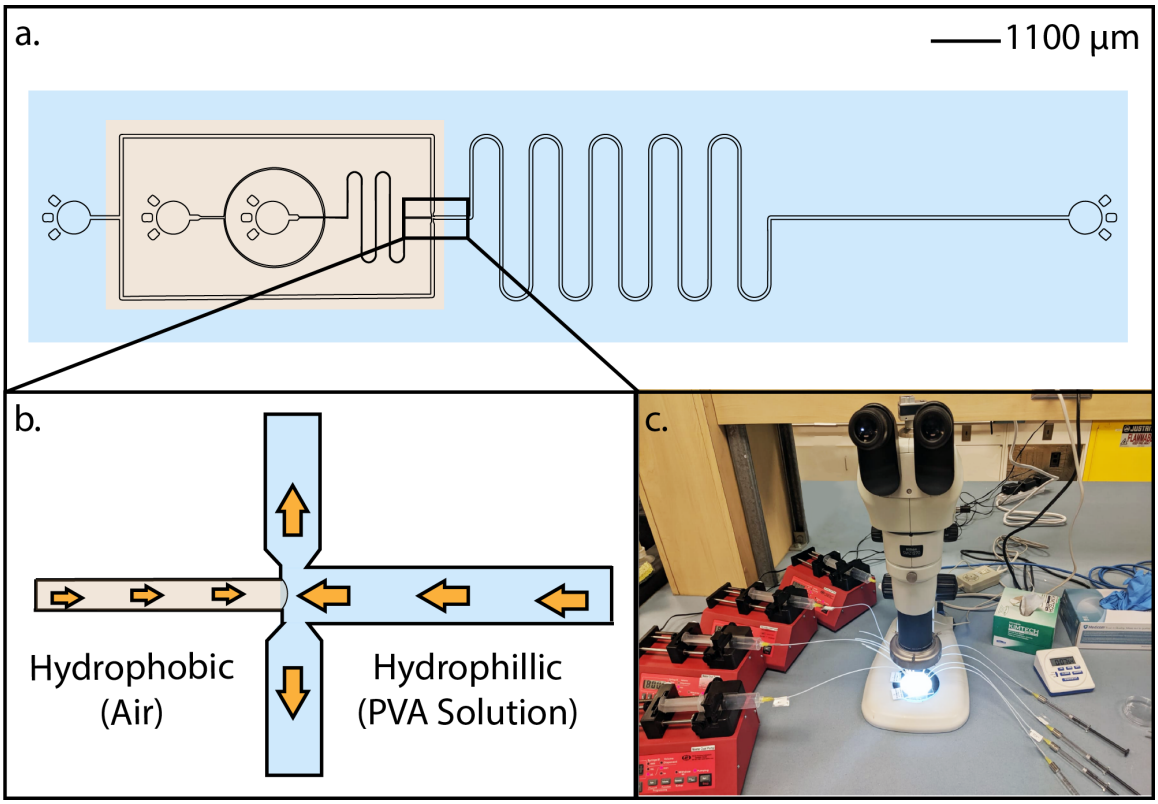

Figure 3.4: **Surface treatment.** a, The proteinosome generation device with hydrophobic and hydrophillic regions highlighted in brown and blue, respectively. b, Interface directionality between the air and PVA solution at Junction 2 of the proteinosome generation device. c, An image showing the overall surface treatment set-up. On the far left of the image are the red syringe pumps holding 25 mL plastic syringes filled with air. The flow rate of all of these syringes was set to 800 μLmin^{-1}.

3.2.4 Proteinosome generation

After having developed a reliable platform for multi-compartmental double emulsion formation and a surface treatment protocol, I developed a method for proteinosome generation using BSA nanoconjugates.[78] For proteinosome generation, the outer phase consisted of a crosslinked BSA/PNIPAM-co-MAA membrane. The middle phase consisted of 2-ethyl-1-hexanol (2EH). The inner phase consisted of rhodamine B (RITC)-labelled azide-functionalized proteinosomes (red). Using the proteinosome generation device, I could produce multi-compartmental double emulsions on a PDMS device. These proteinosomes contained azide-functional groups which have been shown to

interconnect (*via* click-chemistry) upon removal of the 2EH oil phase via dialysis. These same experiments were also replicated using a bicyclo[6.1.0]nonyne (BCN)-functionalized BSA nanoconjugate. These proteinosomes were stable off of the device for up to three months (at -4C) and could be viewed using confocal microscopy.

The platform allowed me to generate mono-, bi-, tri-, tetra-, penta- and hexa-compartmental double emulsions (Figure 3.5). Figure 3.5a shows images of these proteinosomes. The brightfield images on the left were taken using a Dalsa camera attached to a Nikon Ti microscope, the fluorescent images on the right were taken post dialysis using a Zeiss confocal microscope. The red fluorescence is attributed to the RITC tag. Figure 3.5b shows the percent accuracy of encapsulation for (n=30) droplets. This means the number of droplets that were composed as expected when the flow rates were set to those values which we had determined generate multicompartmental double emulsions of a certain composition. For example, if we set the flow rates to 90 μLmin^{-1} for the outer phase, 5 μLmin^{-1} for the middle phase and 1 μLmin^{-1} for the inner phase we would expect bi-compartmental double emulsions. Figure 3.5b shows that the accuracy of encapsulation decreases as the number of inner droplets increases. This could be for several reasons, one of which is that these systems became more unstable (break up into smaller droplets) as they got larger. Another reason could be that small outer channel width results in high shear forces that breaks up the double emulsion droplets at a certain size. This hypothesis is supported by the data in Figure 3.6 which shows that the middle phase droplet area (the total size of the outer droplet of the double emulsion) reached a plateau after the tetra-compartmental double emulsions. The area of the droplets was calculated using ImageJ as described in the Materials and Methods section. These results indicate that there is a maximum size that our platform allows for the outer droplet size, which explains why encapsulation becomes less accurate at larger sizes.

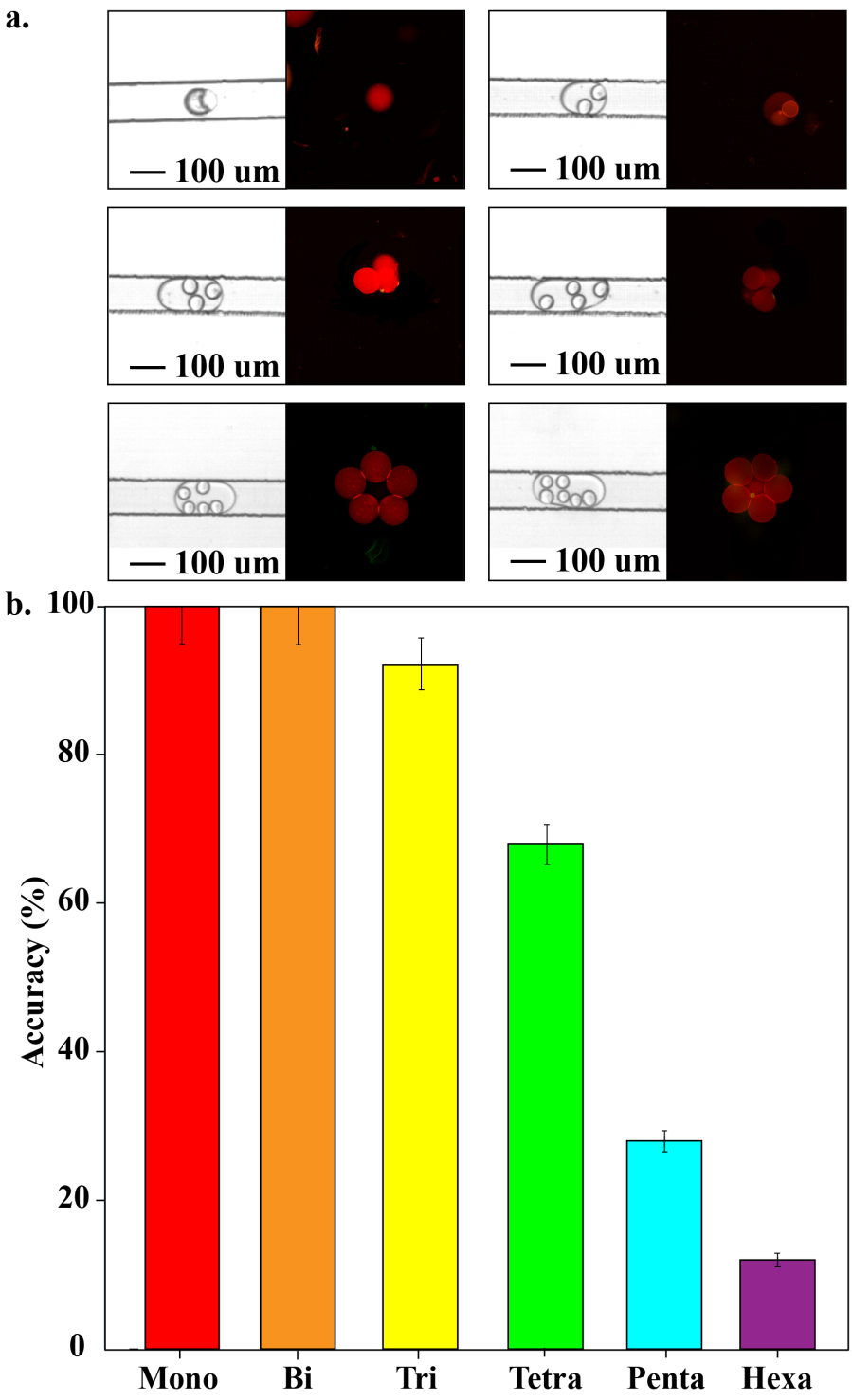

Figure 3.5: **Proteinosome generation** a, Images (from left to right and top to bottom) show mono-, bi-, tri-, tetra-, penta- and hexa-compartmental double emulsions. The images on the left were taken using a Dalsa camera attached to a Nikon Ti microscope (pre-dialysis). The images on the right were taken using a Zeiss confocal microscope post-dialysis. The red fluorescence is due to a RITC fluorescent tag. b, The accuracy of encapsulation for mono- to hexa-compartmental double emulsions (n=30). The error bars represent the standard error.

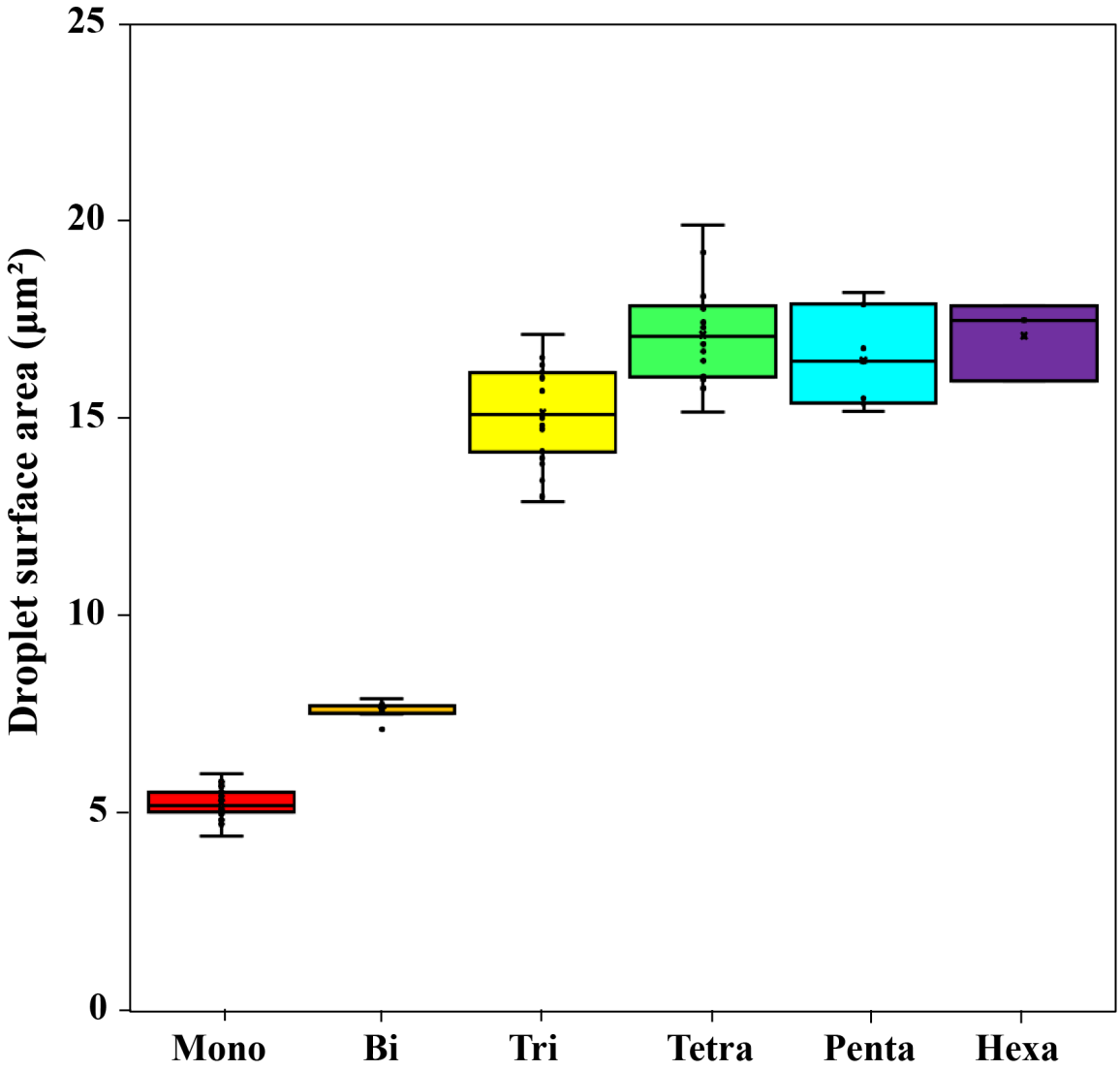

Figure 3.6: **Box and whiskers droplet area graph.** The graph shows the outer area of double emulsions as a function of their composition. The red denotes mono-compartmental double emulsions, brown indicates bi-compartmental double emulsions, yellow indicates tri-compartmental double emulsions, green indicates tetra-compartmental double emulsions, blue indicates penta-compartmental double emulsions and purple indicates hexa-compartmental double emulsions. Error bars show the standard deviation (n=30).

3.2.5 Development of a microfluidic platform for prototissue formation

After having developed a stable proteinosome platform, the next stage was to generate a platform which would allow for the insertion of two different types of proteinosome

populations simultaneously. There was very little precedent in the literature for PDMS devices with this capability as binary (population with two different phenotypes) multicompartmental double emulsions are most often generated using glass microcapillary devices.[111,134] Regardless, I needed to be able to generate droplets that were smaller that our microfluidic device outlined in Chapter 2 is capable of generating redbecause these proteinosomes were not capable of stable click-chemistry interconnection at larger sizes. The PDMS device designs are shown in Figure 3.7. Design **a** is essentially identical to the final proteinosome generation design except that it has two separate inner phase inlets instead of one. The two inner channels were 25 μm, the middle channels were 50 μm and the outer channels were 100 μm. Designs **b** and **d** were more creative approaches which were reverse engineered from some of the design concepts seen in the literature.[135] Design **b** involved a split Y-junction where the middle inlet was for the oil phase and the upper and bottom inlets are for the two inner phases. Design **d** involved a modified co-flowing junction to generate the inner aqueous droplets. Design **c** was inspired by the work of Nisisako *et al.*[136] who made alternating droplets using a modified T-junction. Design **c** also incorporated an additional flow focusing element which branched off from the upper and lower flow focusing channels in an attempt to increase shear force. Of these designs, designs **a** and **b** were found to be able to form double emulsions (albeit without control over size and composition). The T-junction in design **c** often resulted in inner droplet merging or unequal sizing. Device **d** did not generate double emulsions at all. Designs **e** and **f** are evolved from designs **a** and **b**, respectively. Design **e** incorporated larger channels as we wanted to be able to encapsulate up to ten inner droplets. Design **f** also involved larger channels for the same reasons, as well as an additional constricted flow focusing channel to increase shear force. Ultimately, of these two designs, design **e** was found to work the most reliably. However, the first meander (leftmost meander) was

observed to result in inner droplet merging and sticking. Designs, **g**, **h**, **i** and **j** were all created as design e iterations without the first meander. Designs **g** and **i** involved meanders with slightly smaller dimensions (200 μm rather than 400 μm in diameter). Design **i** also included two additional oil outlets placed near junction 2, which allowed for the removal of excess oil from the prototissue (which had been shown to affect proteinosome cross-linking[78]). Ultimately, these smaller junctions were shown to generate greater shear forces than were necessary and limited the number of inner aqueous droplets which could be encapsulated in the oil phase. Design **h** involved the separation of the W/O proteinosome aqueous droplets right up until the second junction, where they were meant to merge together to form W/O/W double emulsions. Unfortunately this did not turn out to be the case as the droplets did not tend to merge at junction 2 which resulted in separate double emulsions rather than the intended binary multicompartmental double emulsions. Design **j** was shown to work the best of all the aforementioned designs. The two inner channels were 100 μm, the middle channels were 200 μm and the outer channels were 400 μm in diameter. Additional details on the work done with this device will be elaborated upon in Chapter 5.

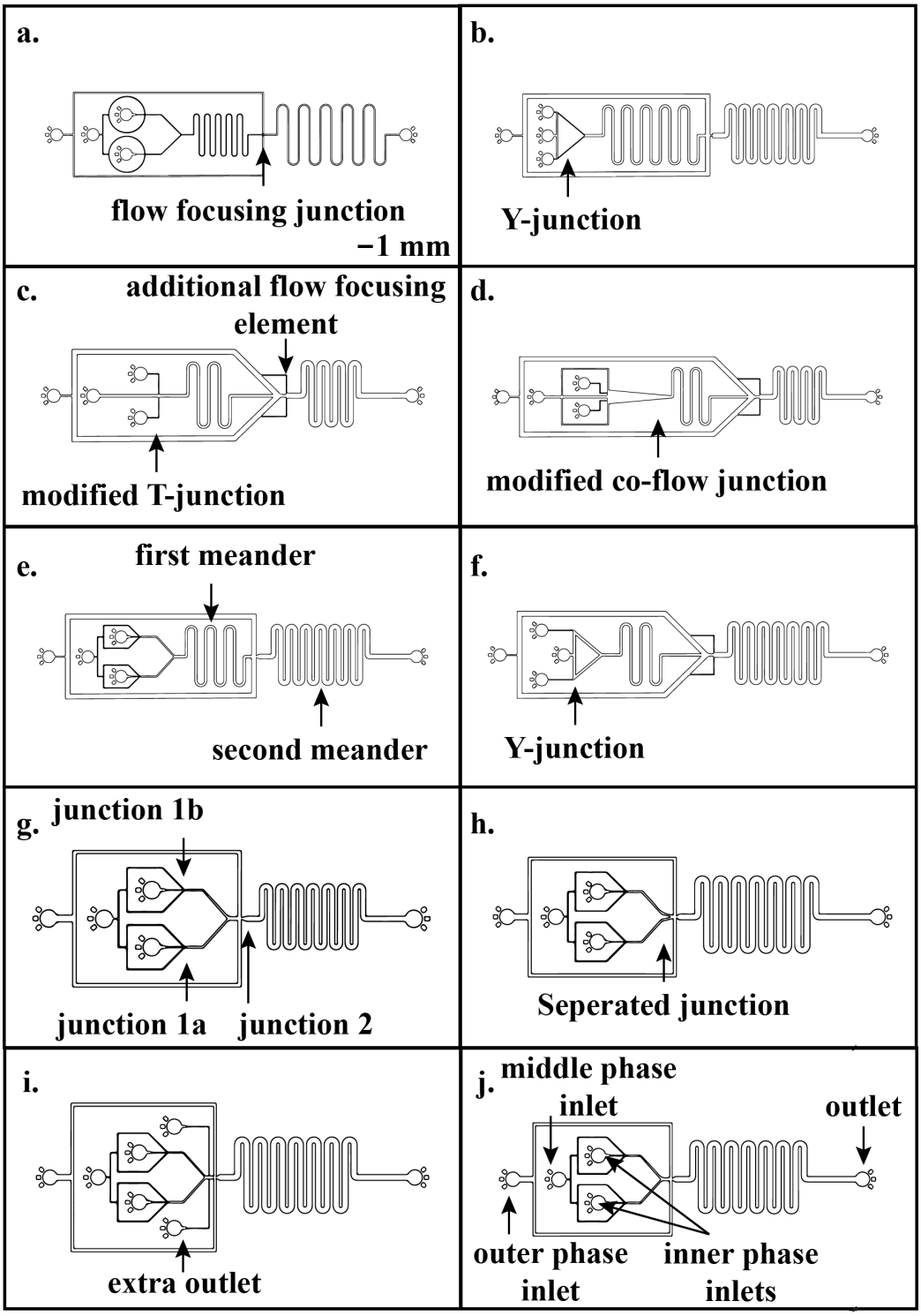

Figure 3.7: **Microfluidic device design evolution for the generation of prototissues.** Design **a** is based on with the proteinosome generation device. Designs **b** and **d** were reverse engineered from some of the design concepts in the literature[135]. Design **b** involved a split Y-junction where the middle inlet was for the oil phase and the upper and bottom inlets are for the two inner phases. Design **c** made alternating droplets using a modified T-junction. Design **c** also incorporated an additional flow focusing element which branched off from the upper and lower flow focusing channels. Design **d** involved a flow focusing chamber to generate the inner aqueous droplets. Design **e** incorporated larger channels. Design **f** also involved larger channels, as well as an additional flow focusing channel to increase shear force. Designs, **g**, **h**, **i** and **j** were all created as design **e** iterations without the first meander. Designs **g** and **i** involved meanders with slightly smaller dimensions. Design **i** also included two additional oil outlets placed near junction 2. Design **h** involved the separation of the W/O proteinosome aqueous droplets right up until the second junction, where they were meant to merge together to form W/O/W double emulsions. Design **j** was shown to work the best. Scale is the same for all images.

3.3 Conclusions

Using a novel microfluidic device design and surface treatment, I was able to demonstrate the creation of proteinosomes as a step towards the generation of prototissues. This work represents the first example of microfluidic proteinosomes that are capable of interconnecting and lays the groundwork for more complex tissue-like structures. I also demonstrated the troubleshooting processes involved in platform development and surface treatment. The device produced statistically reliable multicompartmental double emulsions which can be dialyzed as a step towards prototissue generation which will be explored in Chapter 5.

3.4 Materials and methods

With the exception of the sections detailed below, the materials and methods section for this chapter are the same as those detailed in Chapter 5.

3.4.1 Surface treatment of microfluidic devices for the generation of proteinosomes

The following surface treatment protocol was modified from the work of Bauer *et al.*[132] and Trantidou *et al.*[133] The first step involves making the PVA solution, which must be done the day prior to usage. 0.01 mg mL^{-1} of 87-90 % hydrolyzed PVA (89-90 % Hydrolyzed, Sigma Aldich) was added to water. The solution was mixed at room temperature at 1200 rpm for 45 minutes, at 100°C at 1200 rpm for 45 minutes and, finally, at 65°C at 1200 rpm overnight. The following day, the PDMS devices and PDMS coated slides were placed in a Diener Electronic Zepto ONE plasma bonder (1 min, 100 W, 0.64 mbar) in order to activate the surfaces. After activation, the device and slide were pressed together to bond their surfaces. These devices were left

to sit for 2 minutes. The set-up is shown Figure 3.4. Aladdin Single-Syringe Infusion Pumps (World Precision Instruments) were used at 800 μL/min. A 25 mL plastic syringe filled with air was connected to a 30 G syringe tip that had been heat-ligated to 10 inches of 1/16 inch outer diameter (OD) x 750 μm inner diameter (ID) PTFE tubing. A second 1 mL syringe was filled with the freshly made PVA solution and was connected to another 30 G syringe tip that has been connected to another 10 inches of PTFE tubing. The left inlet was attached to a 5 inch length of PTFE tubing as an outlet. The middle inlet was plugged. Lastly, the device outlet was attached to the PVA solution-filled syringe. To begin the treatment procedure, the pump was turned on and air was allowed to flow through the device for at least 1 minute. After air had filled the device, the PVA solution was manually pushed through until it met the second junction of the device (see Figure 3.4. This interface was held for 10 minutes. After 10 minutes, the inlet attached to the air-filled syringe was reattached to the end of a filtered air gun. The PVA solution was blown out of the device. The device was then placed on a hot plate for 15 minutes at 110°C. The microfluidic devices were stored in an oven at 65°C for 72 hours to allow for full PDMS hydrophobic recovery of the hydrophobic region.

3.4.2 Double emulsion generation

Referring to Figure 3.3, the red-colored inlet denotes the inner water phase inlet which consists of MilliQ water, the yellow colored inlet indicates the middle oil phase which consists of 2.5% PicoSurf w/w in FC-40 and the blue-colored inlet indicates the MilliQ water with an added 0.5 % w/w of SDS. All initial tests of the device design were done with these reagents to verify the design with solutions that were shown in the literature to function reliably. Solutions were pumped using 1 mL gastight glass syringes (Hamilton) that had been loaded onto Aladdin syringe pumps. These

syringes were attached to the microfluidic device using 1/16 inch OD x 750 μm ID PTFE tubing. The outer phase was set to 20 μLmin^{-1}, the inner phase was set to 3 μLmin^{-1} and the inner phase was set to 1 μLmin^{-1}. Videos were captured using a Dalsa camera (Nanotech) on a Nikon Ti-U microscope at 100 fps.

3.4.3 Proteinosome generation

The azide- and BCN-BSA-conjugated nanoconjugate was synthesized by Dr Gobbo using a previously described methodology.[78] The nanoconjugates were kept in the freezer. 8 mg mL^{-1} solutions were made in MilliQ water in a 1 mL glass screw-top vial. Next, crosslinker (O,O '-b[2-(N-Succinimidyl-succinylamino)ethyl]polyethylene glycol) (Sigma Aldrich) was added at a concentration of 160 mg mL^{-1} in Na_2CO_3 solution (pH 8.5, 100 mM). 0.5 mL of the above solution was added to 0.5 mL of Na_2CO_3 buffer in a 1 mL glass vial. Next, 1mL of the "proteinosome oil" (2-ethyl-1-hexanol) was drawn up into another 1 mL glass gastight syringe. The outer solution consists of 250 μL of 8 mg mL^{-1} of aqueous solution of a BSA/PNIPAM-co-MAA nanoconjugate in 25 mL of 1 M Na_2CO_3. In order to generate mono-compartmental double emulsions the outer phase was set to 100 μLmin^{-1}, the middle phase was set to 5 μLmin^{-1} and the inner phase was set to 1 μLmin^{-1}. These flow rates were subject to a slight fluctuation of $\pm 5\mu$Lmin^{-1} device to device. Generating multicompartmental double emulsions with more inner droplets requires that the outer phase be methodically decreased by approximately 10 μLmin^{-1} for progressively larger proteinosomes. For example, bi-compartmental double emulsions require an outer phase of approximately 90 μLmin^{-1}, a middle phase of approximately 5 μLmin^{-1} and an inner phase of approximately 1 μLmin^{-1}. For videos of the different multicompartmental double emulsions is shown in Appendix B, Figures B.5 to B.8. After collection from the microfluidic device, the excess aqueous solution was removed and was replaced with

approximately 250 μL (or a 1:1 ratio to the collected sample) of a 160 mg mL^{-1} solution of crosslinker in water. Then, these proteinosomes were left to sit for 72 hours. The click-chemistry between proteinosomes occurred after dialysis, during which the oil was removed. To transfer the proteinosomes into water, the proteinosomes were dialyzed (10 KDa - 14 KDa, Millipore Dialysis Bags) against water/70% ethanol for 3-4 h, then water/30% ethanol for 3-4 h, and finally 100% water for 18 h, in order to produce our final proteinosome spheroids.

3.4.4 Proteinosome visualization

Approximately 250 μL of proteinosomes were inserted (using a P1000 pipette) into a fabricated glass slide holder described in detail in the Materials and Methods of Chapter 5. This slide was placed onto a Zeiss confocal laser scanning microscope mobile stage. The prototissues were visualized using either the 488 nm or the 555 nm laser lines to excite the FITC and RITC tags, respectively. Replicates were conducted three times on different proteinosome samples. All images were taken at either 20x or 50x wide-angle magnification.

Chapter 4

Bespoke asymmetric liposomes to model passive malarial drug transport across red blood cells

In this chapter I show the methodological generation of lipid-based synthetic cells using a microcapillary microfludic platform. I also improved upon the biomimicry of these synthetic cells through the use of a novel combination of mammalian lipids and membrane asymmetry, to mimic red blood cells. Lastly I propose ways in which these artificial red blood cells can be improved, quantified and used for passive drug development assays.

All of the data, analysis and writing in this chapter are my own.

4.1 Introduction

The focus of the following chapter is on the more biomimetic lipid-based synthetic cells, rather than the polymeric-based cells shown in Chapter 3. One of the simplest and most reproducible ways to make liposomes is highlighted in recent work by Deng *et al.*[9,137] which reported a surfactant-assisted microfluidic strategy for assembling liposomes from double emulsions (Figure 4.1). The researchers use a triblock co-polymer surfactant, Pluronic F-68, in order to adjust interfacial energies in the W/O/W emulsion system which results in complete de-wetting (occurs at the O/W interface and describes the process of the fluid retraction from an energetically unfavorable surface).[9,137]

Despite recent advances in liposomal generation many (including the work by Deng *et al.*) are made up of symmetric lipid bilayers. *In vivo*, all cells have inner and outer leaflets which differ one to the other. Membrane asymmetry is known to affect various bilayer properties including, but not limited to, membrane potential, permeability, shape, surface charge and stability.[138] Loss of asymmetry has numerous physiological consequences.[138] For example, the externalization of phosphatidylserine (PS), a lipid which is primarily contained in the inner red blood cell leaflet, to the outer leaflet has been linked to blood coagulation and erythrocyte adhesion.[138]

In part due to their complexity, there are only a handful of publications which create asymmetric lipid bilayers using microfludic technology. The most common approach is a layer-by-layer technique which is used by Hu *et al.*, Romanov *et al.* and Matosevic *et al.* (Figure 4.2a).[58,139,140] In this technique, a lipid monolayer is formed at each of the water-oil interfaces. The benefits are that this technique is relatively simple and reliable. Nevertheless, the layer-by-layer method involves the use of droplet capture posts which are difficult to use in a high throughput manner. Air is also

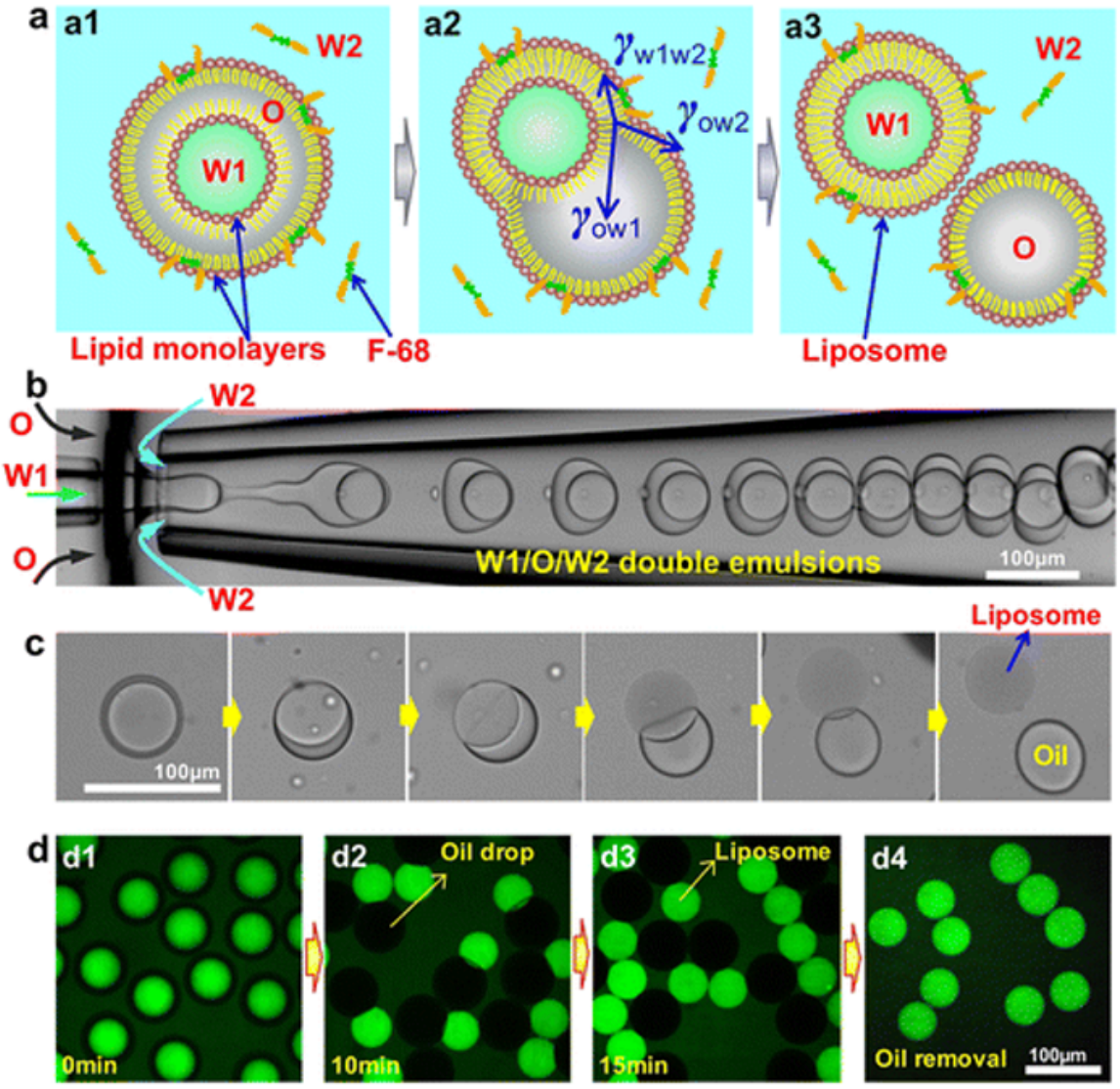

Figure 4.1: **De-wetting microfluidic method for monodisperse generation.** a, Schematic for the surfactant-assisted assembly of liposome from the de-wetting of a mono-compartmental double emulsion. b, Preparation of the W/O/W double emulsions in a microcapillary device. Time-series optical c, and confocal d, images of the de-wetting process (d1–d3) with the liposomes separating from the residual oil droplets (d4). W1, W2 and O indicate the inner water phase, outer water phase and oil phases, respectively. Scale bars are 100 μm. Image reproduced from Deng *et al.*[9] with permission.

easily captured in these regions and droplets can fall apart when higher flow rates are required. These liposomes can also contain residual oil within the lipid membranes which limits their applicability as synthetic cells or drug delivery vessels. The pulsed-jet flow method involves the use of a pulsed jet flow against two parallel planar asymmetric lipid bilayers to form liposomes (Figure 4.2b).[141,142] The advantage of this method is that it allows for the construction of complex, higher level, synthetic cells. The downside is that the pulse jet-flow method require highly precise alignment as well as complex engineering to generate a functional platform. The final approach, by Lu *et al.*, made use of a PDMS platform with a triangular post region and two flow focusing regions (Figure 4.2c).[143] The main steps involved in the liposome fabrication process were: 1) the formation of monodisperse water emulsions in an oil/inner-leaflet-lipid solution, 2) the replacement of the inner-leaflet-lipid solution with an outer-leaflet-lipid solution, 3) the formation of W/O/W double emulsions, and 4) the extraction of the excess oil/outer-leaflet-lipid solution.[143] This approach is particularly advantageous when one considers the versatility of PDMS platforms. That said, the micro-fabrication techniques required to design these platforms is highly complex and subject to variability.

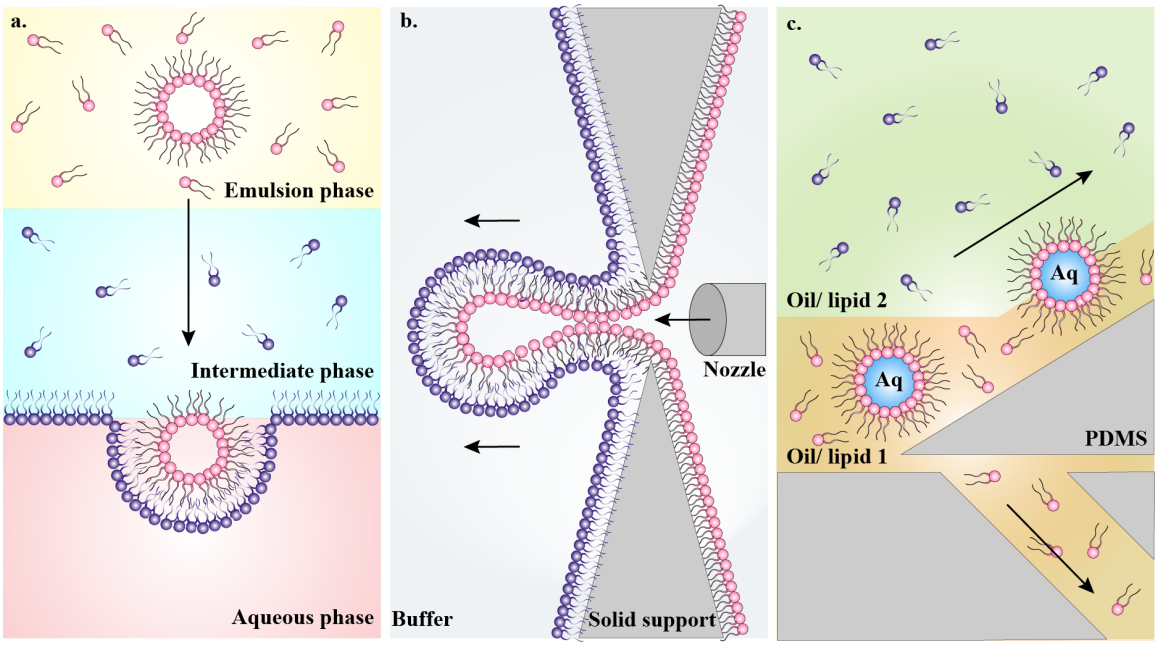

Figure 4.2: **Methods for the generation of asymmetric liposomes using microfludic devices.** a, Schematic of layer-by-layer asymmetric liposomal formation. b, Schematic of pulse jet flow. c, Schematic of PDMS platform with a triangular post region for oil/lipid 1 removal. Second flow focusing junction, where bilayer formation occurs, is not shown. Arrows show direction of flow.

The aim of the following work was to combine the simple liposomal formation methods outlined by Deng *et al.* with a versatile PDMS microfludic platform capable of asymmetry similar to Lu *et al.* in order to generate simple, reproducible asymmetric liposomes which are capable of red blood cell-like biomimeticity. That said, there are several challenges associated with this goal. The first is that the precedence for the microfluidic formation of liposomes using double emulsions in the literature involved putting the lipids in the oil phase.[111,137,144,145] In order to generate asymmetric liposomes using the methodology outline by Deng *et al.*, different lipids would have to be inserted into the two separate aqueous phases. This may be a challenge because lipids more readily dissolve in the solvent phase (chloroform:hexanes), and putting them in the aqueous phase is comparatively labor intensive. I hypothesized that it could be possible however, as work done with DIBs[88] have shown that lipids can successfully form bilayers when inserted in the aqueous phase. The second challenge

involves the use of PDMS platforms with the solvents used for liposome formation. As required, the microcapillary platform outlined in Chapter 2 could be re-purposed for the generation of these lipid-based synthetic cells. The following chapter also contains a proposal which outlines how these asymmetric liposomes can be tailored to model red blood cells which can, in turn, be used to study the passive transport of anti-malarial drugs.

4.2 Results and discussion

4.2.1 Lipid-based double emulsion formation

As I had a significant amount of experience working on synthetic cells using PDMS microfluidic devices (Chapters 3), I opted to start my work with liposomes using devices that were already available. Lu *et al.* have also shown that a PDMS platform is capable of supporting liposomal formation.[143] I started my work with the proteinosome generation device outlined in Chapter 3, which is shown again in Figure 4.3a. The devices were fabricated and surface treated as described in chapters 3 and 5. To test my design, I made three separate solutions (an inner, middle and outer phase) as outlined by Deng *et al.*[9] In brief, the outer phase consisted of an aqueous solution containing polyvinyl alcohol (PVA) and Pluronic F-68 (a surfactant which stabilizes liposomal de-wetting), the middle phase consisted of 50:50 chloroform and hexanes, and the inner phase consisted of an aqueous solution containing PVA and polyethylene glycol (PEG) (both serve to stabilize droplet formation). The outer phase was set to 20 μLmin^{-1}, the middle phase was set to 3 μLmin^{-1} and the inner phase was set to 1 μLmin^{-1}, though flow rates were subject to small changes device-to-device. The results obtained using these solutions showed that this device was capable of producing double emulsions. That said, the volatile nature of the chloroform:hexanes

solution caused the channels on the device to swell shut after approximately 3-5 minutes.[146] To mitigate this swelling, I then performed thermal treatment as described by Lee *et al.*, which has been shown to decrease the porosity of the PDMS[147]. In brief, after the microfluidic devices were surface treated they were placed in a glass petri dish for 24 hours at 150°C. I found that the thermal treatment increased the time that the device was able to function by about 5 minutes. In an attempt to further increase the time in which the PDMS device could be used, I decided to try using a microfluidic device with larger channel sizes (Figure 4.3b).

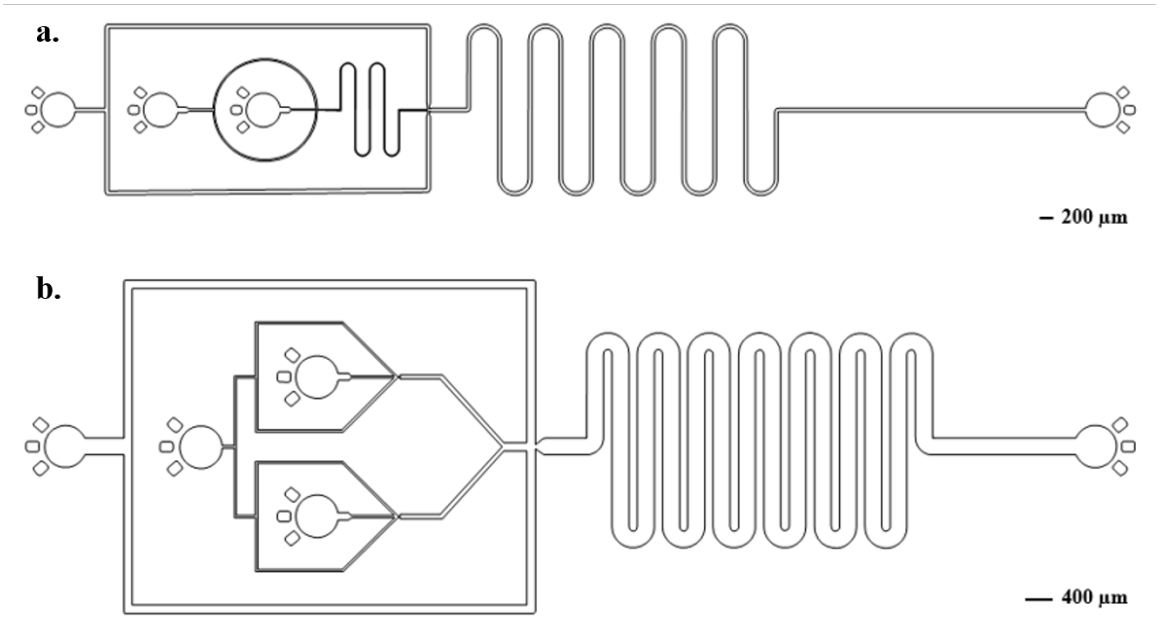

Figure 4.3: **PDMS microfluidic devices for asymmetric liposome formation.** a, Illustrates the double emulsion device design which was developed in Chapter 3. b, Shows the multicompartmental double emulsion device design which was developed in Chapter 5.

The larger PDMS device was the same as that described in Chapter 5. The same surface and thermal treatment protocols were employed as described previously. The solutions, syringes, and device set-up was also analogous to that described previously, with the exception that the second, inner inlet, was plugged closed. As expected, the larger channels did not swell completely shut, which allowed for the continued

pumping of the solutions. That said, the chloroform:hexanes middle phase was seen to adhere to the channels of the device preferentially over the aqueous phases despite the hydrophilic surface treatment. This could be for several reasons, the foremost of which is that the porosity of the PDMS material created enough space through which volatile solvents could vaporize. As a result, I could not generate the requisite mono-disperse droplet populations. Rather than continue to troubleshoot surface treatment protocols for these PDMS devices, I opted to test the glass microcapillary device outlined in Chapter 2. Though less flexible than PDMS platforms in terms of device configuration, this microcapillary device would allow for the use of glass capillaries which have been shown to make liposomes in the literature.[9,148]

4.2.2 Microcapillary device, surface treatment and oil-phase liposome generation

I modified the microcapillary device described in Chapter 2 by using differently sized capillaries (described in the Materials and Methods). As can be seen in Figure 4.4a, this device consisted of 2 separate junction boxes. The inner phase capillary (dark purple) was glass, the middle phase capillary (brown) was PTFE tubing, and the outer phase capillary (light blue) was glass (Figure 4.4b). The inner and middle capillaries were used as purchased, and were found not to require additional surface treatment. Early studies showed that additional surface treatment would be required for the outer capillary.

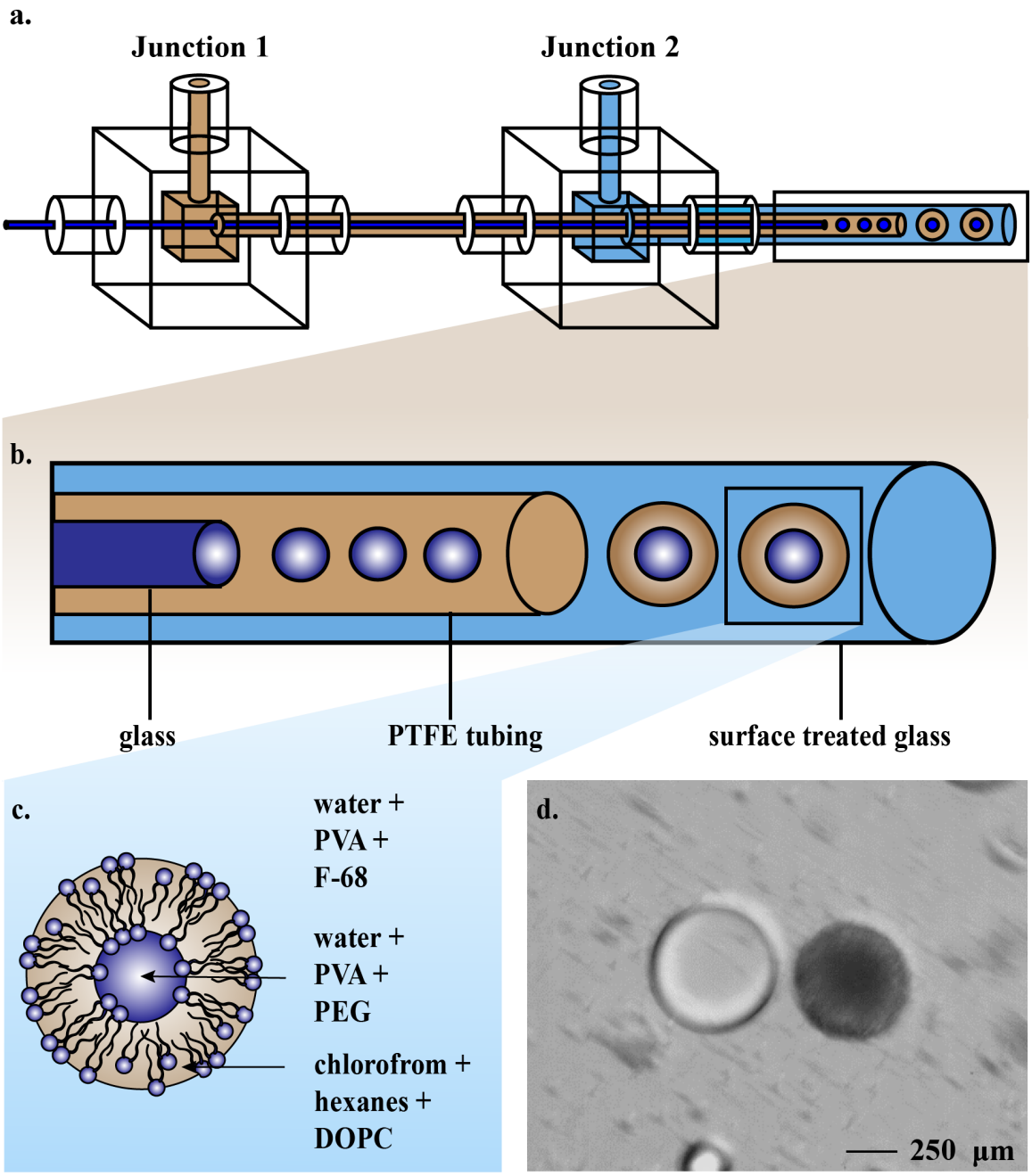

Figure 4.4: **Liposome generation using a glass microcapillary device.** a, Schematic of the microcapillary device used to generate liposomes. Dark blue indicates the inner aqueous phase, brown indicates the middle solvent phase and light blue indicates the outer aqueous phase. b, Zoomed in schematic of the microcapillaries and their droplet formation. The inner capillary was a glass capillary, the middle capillary was PTFE tubing and the outer capillary was of a glass capillary which had been surface treated. c, Schematic showing the double emulsion composition. The inner phase was water, 2% w/w PVA and 8% w/w PEG, the middle phase was 12.5 mg mL^{-1} DOPC lipid 50:50 chloroform and hexanes and the outer phase was 10% w/w PVA and 0.5% w/w F-68 Pluronic surfactant. d, De-wetting process, the light droplet on the left is the middle solvent phase and the darker colored droplet on the right is the liposome.

As can be seen in Figure 4.5, the middle-phase droplet formation did not occur. In-

stead, there were unstable multicompartmental "plugs" (compartments which touch the channels on all sides, a spherical droplet is not formed) which burst upon exiting the outer capillary. Neither glass nor PTFE tubing (material shown in Figure 4.5a) proved able to stabilize the second droplet formation sufficiently. In order to address these issues, I developed a surface treatment protocol which is described below in the Materials and Methods section. In brief, I plasma activated the outer capillary followed by hydrophilic surface treatment with 2-[methoxy(polyethyleneoxy)6-9 propyl]trimethoxysilane. This process rendered the glass hydrophilic enough to form mono-disperse double emulsions, as shown in the schematic in Figure 4.5b. The final step to prove the functionality of my microcapillary platform for the generation of liposomes was to successfully reproduce the work published by Deng *et al.*[111] Using my microcapillary platform, I was able to easily generate a population of monodisperse, mono-compartmental double emulsions. In order to accomplish this I set the outer phase flow rate to 200 μLmin^{-1}, the middle phase flow rate to 40 μLmin^{-1} and the inner phase flow rate to 20 μLmin^{-1}. I found that these liposomes de-wetted in under 5 minutes and produced liposomes reliably, as shown in Figure 4.4d.

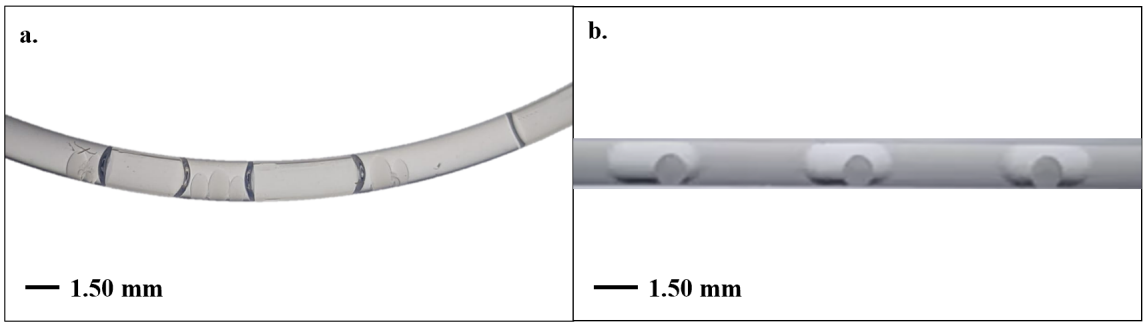

Figure 4.5: **Preliminary double emulsion formation.** Images of the outlet tubing of the device and the double emulsions formed. a, Unstable plug formation in PTFE tubing. b, Stable mono-compartmental double emulsion formation in hydrophilic surface treated glass.

4.2.3 Aqueous-phase liposome generation

As mentioned in the introduction, all liposomes to date formed from double emulsions have put the lipids in the middle solvent phase. Starting with lipids in the aqueous phases theoretically allows for the same self-assembly of the hydrophilic heads of the phospholipids at the aqueous phases and the hydrophobic tails towards the solvent phases that causes bilayer formation upon the de-wetting of the solvent phase. That said, several notable methodological changes had to be conducted in order for this to be possible. The first is that it has been shown in DIBs research that lipid extrusion is a necessary step in the formation of the bilayer between two lipid-filled aqueous droplets.[149] Lipids are less soluble in aqueous solutions and extrusion allows them to be better solubilised.[9] The second new methodological approach involved the preparation of the lipid and surfactant/stabilizer halves of the aqueous solutions separately (described fully in methods section below). 1,2-Dioleoyl-sn-glycero-3-phosphocholine (DOPC) was the synthetic lipid used as it has been shown to reliably generate bilayers.[111] The lipid solution was prepared initially at 10 mg mL^{-1} and was added to the solvent/stabilizer solutions (described in the methods section) at a 1:1 ratio to result in a final concentration of 5 mg mL^{-1} of lipids. For the outer phase solution, the Pluronic F-68 surfactant was added directly prior to solution use. The schematic for these liposomes is shown in Figure 4.6a. Figure 4.6b shows the schematic for the fully formed liposome after the de-wetting of the middle phase. The generation of the double emulsions (Figure 4.6c), was analogous to the procedure for the oil-phase liposomes described above. I found that these double emulsions de-wetted in approximately 15 minutes and produced liposomes reliably, as shown by the liposome depicted in Figure 4.6d. A video showing liposome de-wetting is shown in Appendix B, Figures B.9. Statistical analysis is pending further data collection.

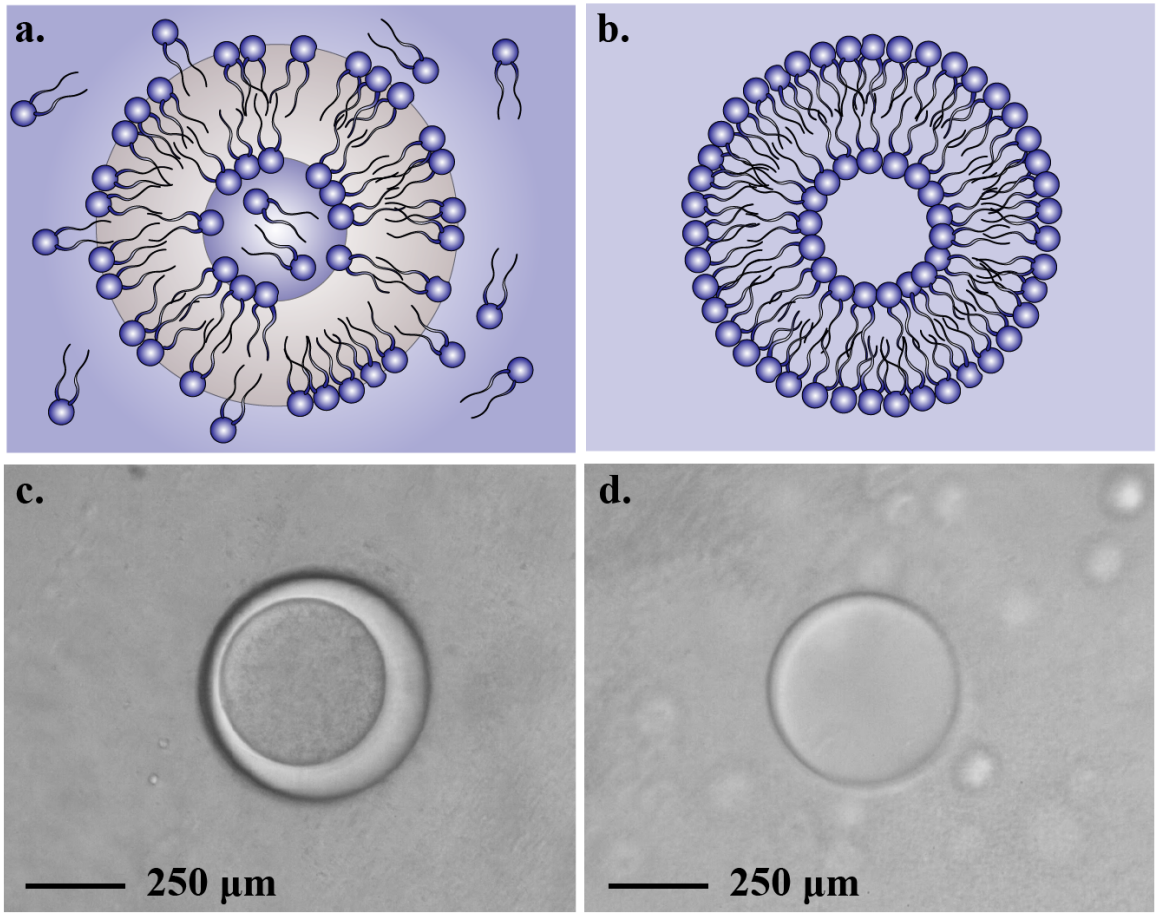

Figure 4.6: **Aqueous-phase liposomes.** Purple denotes the identical outer and inner aqueous solutions and brown denotes the middle solvent phase. a, Schematic for the double emulsion formation with the DOPC lipids contained in the inner and outer aqueous phases. b, Schematic for the liposome formation after de-wetting of the solvent phase. c, Monodisperse double emulsions prior to de-wetting. d, Liposome after de-wetting of the solvent phase.

4.2.4 Asymmetric aqueous-phase liposome generation

The next step was to demonstrate that this technique could be extended for use in the generation of asymmetric liposomes. The preparation of the solutions was analogous to that described above but in the place of synthetic lipids (such as DOPC), eukaroytic lipids were used in order to make these liposomes more biomimetic. For these liposomes, the inner phase contained phosphatidylethanolamine (PE) and the outer phase contained phosphatidylcholine (PC). PE and PC were selected as they are common eukaroytic lipids which are found in many different cells, in particular

the inner and outer leaflets of red blood cells, respectively.[150] The schematic for these asymmetric double emulsion is shown in Figure 4.7a and the schematic for the asymmetric liposome is shown in 4.7b. The generation of the double emulsions (Figure 4.7c), was analogous to the procedure for the oil-phase liposomes described above. I found that these double emulsions de-wetted in approximately 15 minutes and produced liposomes reliably, as shown by the liposome depicted in Figure 4.7d. A video showing asymmetric liposome de-wetting is shown in Appendix B, Figure B.10. Statistical analysis is pending further data collection.

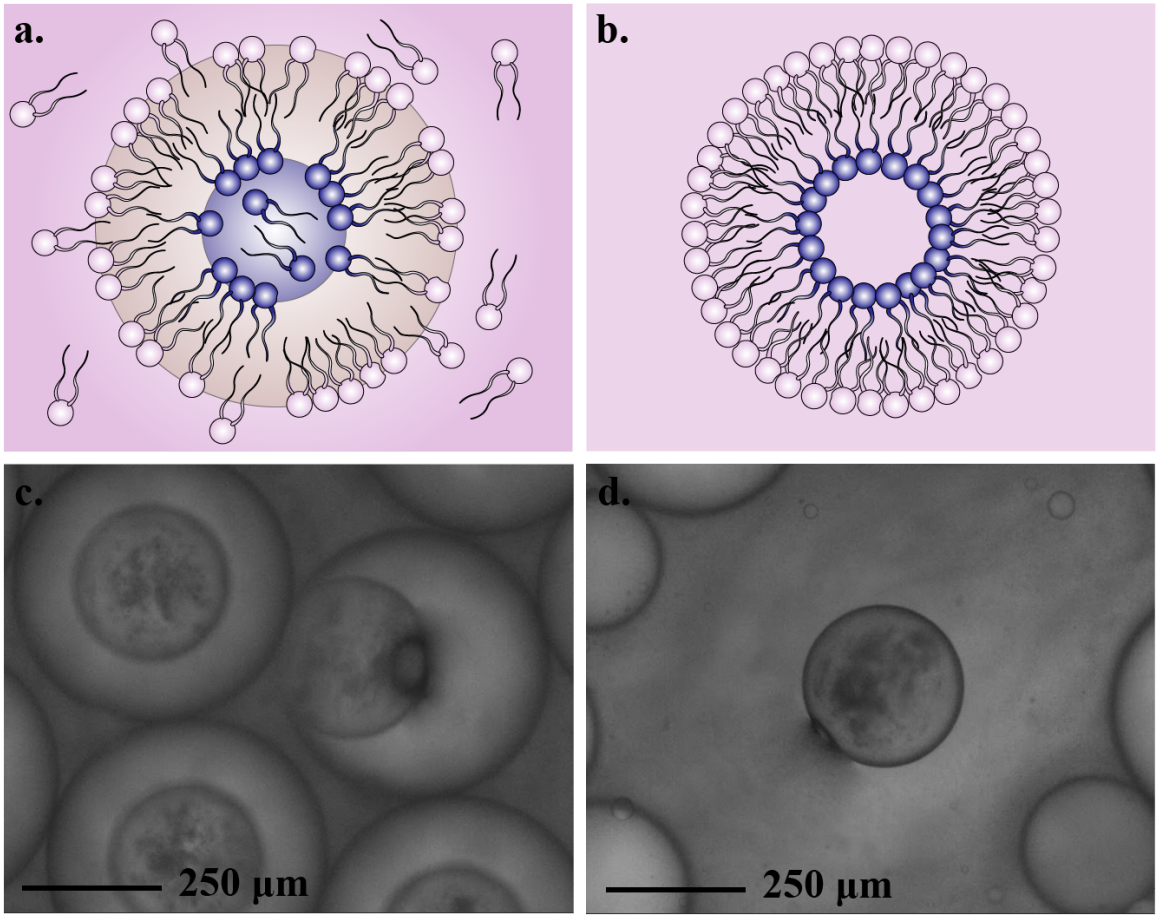

Figure 4.7: **Asymmetric aqueous-phase liposomes.** Pink denotes the outer aqueous solution, brown denotes the middle solvent phase and purple denotes the inner aqueous phase. a, Schematic for the double emulsion formation with the asymmetric PE and PC mammalian lipids contained in the inner and outer aqueous phases, respectively. b, Schematic for the asymmetric liposome formation after de-wetting of the solvent phase. c, Monodisperse double emulsions prior to de-wetting. d, Liposome after de-wetting of the solvent phase.

4.3 Proposed future work

4.3.1 Membrane characterisation

Now that I have developed a functioning platform and observed asymmetric liposomes formation, the first point that needs confirmation is the level of asymmetry in these membranes. Work by Lu *et al.* has already established reliable methodology to accomplish this.[143] I propose using a similar approach to provide proof of concept for our asymmetric bilayers. The content of the synthetic liposome membrane was first examined using fluorescence microscopy. Figure 4.8a-d shows a synthetic lipid liposome with 1-palmitoyl-2-6-[(7-nitro-2-1,3-benzoxadiazol-4-yl)amino]hexanoyl-sn-glycero-3-phospho-choline (NBD-PC) labeled 1,2-dioleoyl-sn-glycero-3-phosphocholine (DOPC) in the outer-leaflet and n-(Texas Red sulfonyl)-1,2-dihexadecanoyl-sn-glycero-3-phosphoethanolamine (TR-PE) labeled 1,2-dioleoyl-sn-glycero-3-phosphoethanolamine (DOPE) in the inner-leaflet. The presence of both green and red fluorescence surrounding the liposome qualitatively confirmed the presence of both lipids in the bilayer membrane.

In order to quantitatively assess the asymmetric lipid distribution of their membrane, the researchers conducted a quenching assay by using fluorescently labeled tracer lipids (Figure 4.8e).[143] They made use of two different configurations of asymmetric liposomes for this assay. The first configuration contained an outer-leaflet of DOPC labeled with NBD-PC and an inner-leaflet with DOPE. The second configuration contained an outer-leaflet with DOPC and an inner-leaflet with DOPE labeled with n-(7-nitrobenz-2-oxa-1,3-diazol-4-yl)-1,2-dihexadecanoyl-sn-glycero-3-phosphoethanolamine (NBD-PE). The NBD quencher is unable to diffuse across the lipid bilayers which means that it cannot quench the fluorophore when the NBD is deposited within the inner-leaflet. As a result, only the accessible outer-leaflet fluorophore will be quenched. The results showed that when the outer-leaflet was labeled with NBD,

95% of the fluorescence was quenched and when only the inner-leaflet was labeled with NBD, 90% of the fluorescence was unquenched. They confirmed the asymmetry of the membrane by showing that the addition of a detergent to the liposomes with an NBD labeled inner-leaflet extinguished all fluorescence.

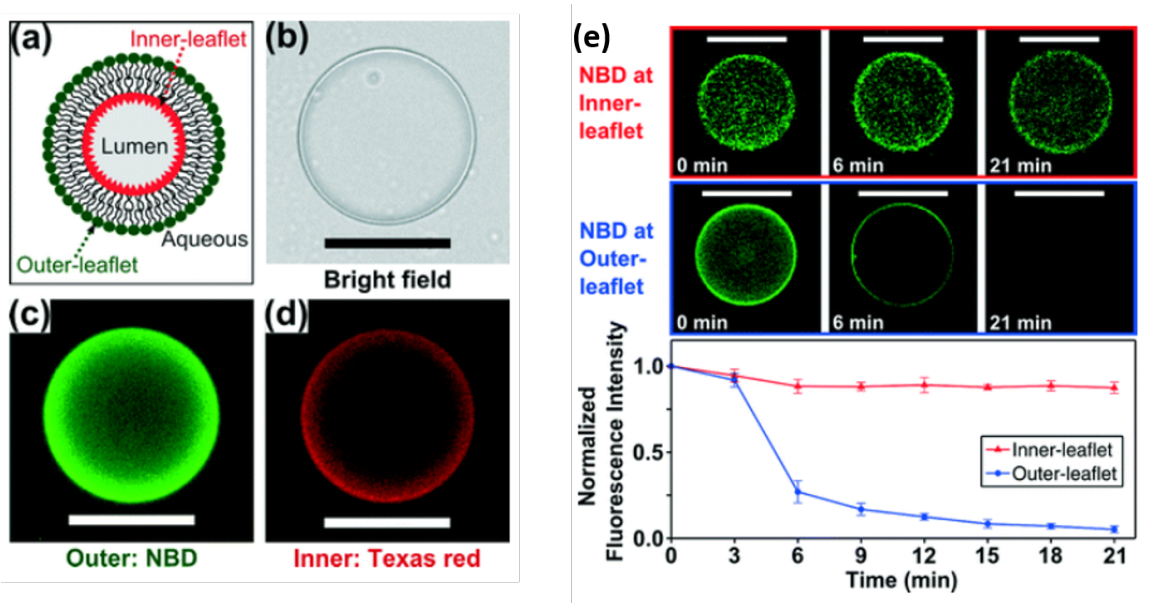

Figure 4.8: **Qualitative measurement of asymmetry.** a, Schematic depiction of asymmetric liposome. b, Shows bright field image of asymmetric liposome. c, Green NBD fluorescence liposome in asymmetric liposome. d, Red Texas Red fluorescence in asymmetric liposome. Scale bars 50 m. e, Shows the quantitative comparison of the fluorescence intensities for two liposome types both before and after the quenching assay. The red boxed images show that 90% of the NBD fluorescence remained unquenched when the inner-leaflet (DOPE) was labeled with NBD-PE. The blue boxed images show that 95% of the NBD fluorescence was quenched when only the outer-leaflet (DOPC) was labeled with NBD-PC. The below graph shows the time-lapse for these fluorescent images. Scale bars 50 μm. Images taken from *Lu et al.*[143] with permission.

Another important aspect of our asymmetric liposomes that we may wish to consider is membrane unilamellarity (indicating that there is only a single lipid bilayer). Without unilamellarity, our liposomes cannot be defined as such, and will likely not mimic the passive diffusion behaviors seen in red blood cells *in vivo*. Red blood cells themselves have been shown to be unilamellar.[151] Lu *et al.* assessed membrane unilamellarity by conducting a protein insertion assay.[143] They reconstituted the membrane protein α-hemolysin (α-HL) into the lipid bilayer. This protein is prevalent in the literature, and has been shown to reliably perforate unilamellar biomembranes.

The monomers of the protein then oligomerize in order to form water-filled transmembrane pores which permit the selective permeability to small fluorescent calcein molecules. As shown by the results in Figure 4.9, this molecular diffusion can observed as changes in the fluorescent intensity in the liposome over the span of 60 minutes. Without the α-HL protein, the fluorescence inside the liposomes decays at a significantly slower rate (photobleaching). These experiments effectively confirm that their asymmetric liposomes have unilamellar membranes and effectively disclude multisomes (multi-layer lipid bilayer spheres).

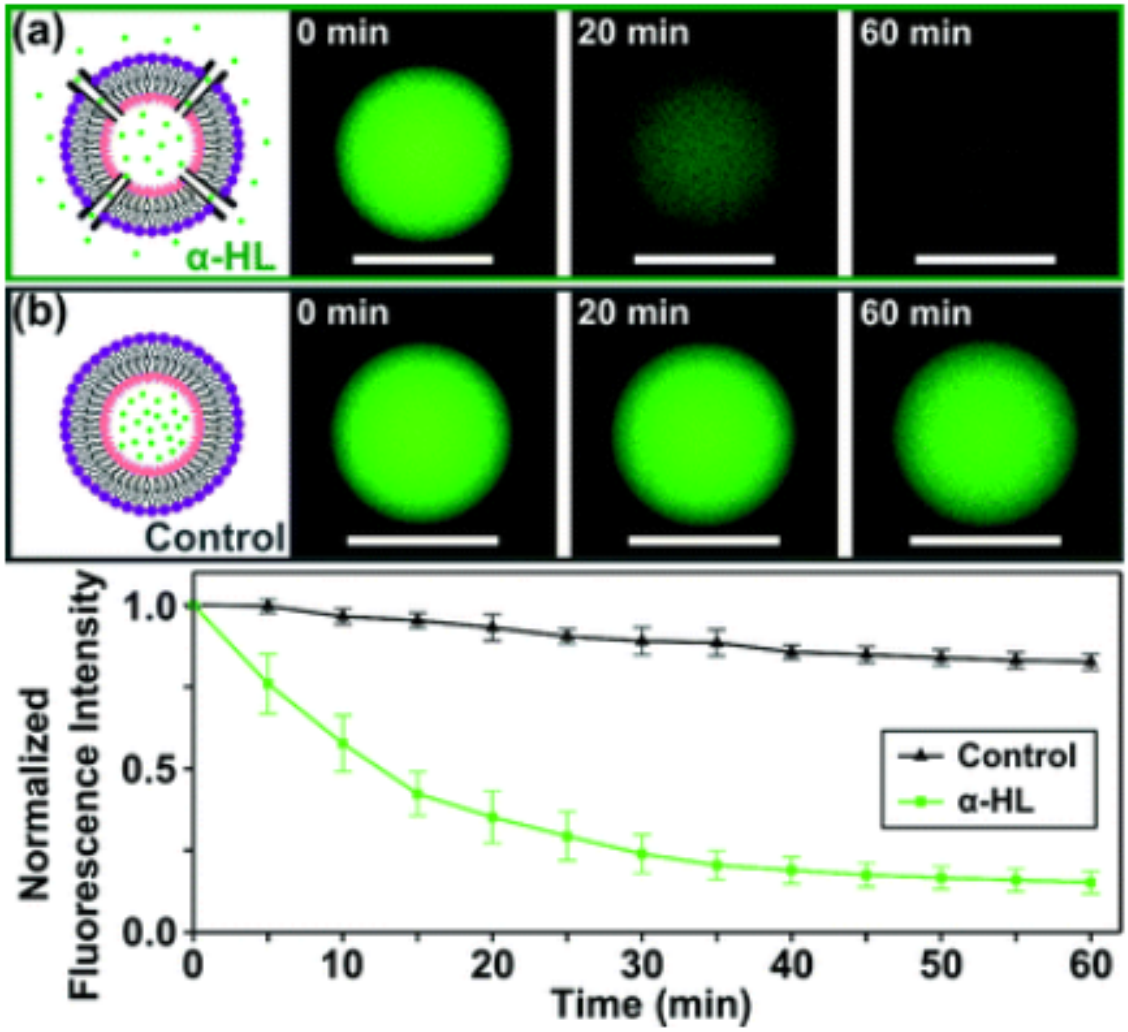

Figure 4.9: **Membrane unilamellarity characterization.** Membrane unilamellarity characterization of the asymmetric liposomes using α-HL. a, Liposomes with α-HL inserted into their membrane show a rapid decrease in calcein fluorescence. b, Liposomes without α-HL inserted into their membrane display a slow decrease in calcein fluorescence. Scale bars 50 m. Images taken from Lu *et al.*[143] with permission.

4.3.2 Asymmetric liposome generation to model red blood cells

The next step in this project will be to attempt to successfully model the phospholipid membranes of red blood cells (RBCs). As can be seen from Figure 4.10, there is a distinct difference between the phospholipid composition of the inner and outer leaflets

of red blood cells.[152,153] If I tailor the phospholipid composition to match that of RBCs determined in the literature it is possible that we could model passive drug malarial drug diffusion using synthetic cells. Verkleij *et al.* showed that sphyngomyelin (SM) and PC make up more than 85% of the outer leaflet, with the rest being PE.[150] In contrast, the inner leaflet has a total of less than 25% SM and PC, 45% PE, and 25% PS. It is worth mentioning that the reported bar graphs of Verkleij *et al.* (shown in Figure 4.10) do not add up to 100%. This is because the methods used in the original study were not capable of reporting the composition of other lipids which are known to reside in the membrane (lyso lipids). That said, I believe that these numbers are a good starting point in my pursuit of a artificial RBC model. Afterwards, I will continue to tweak the composition to match more recent research such as the work by Vahedi *et al.*[153] For all of my future experiments with asymmetric liposomes I will be using surfactants and stabilizers at the same concentrations detailed prior. The only difference will be that the asymmetry will be designed to mimic that of red blood cells with 5 mg mL^{-1} of lipids at the concentrations detailed above in the inner and outer phases.

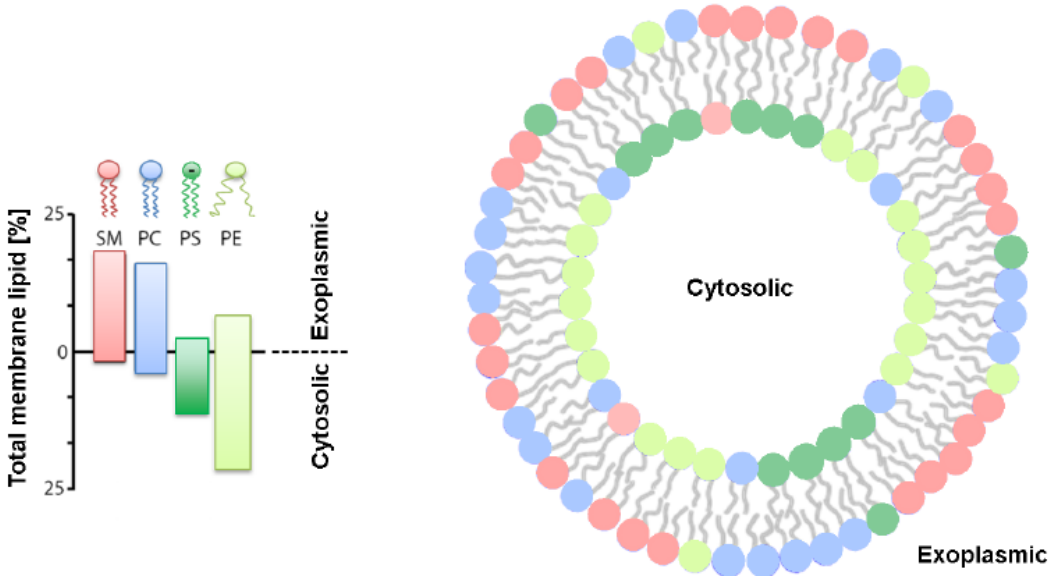

Figure 4.10: **Red blood cell asymmetric phospholipid membrane composition.** Proposed distribution of phospholipids in human red blood cell membranes put forward by Verkleij *et al.*[150] Image reproduced from Marquardt *et al.*[152] with permission.

4.3.3 Model for malarial drug transport

I propose that we could then study the passive diffusion of a widely-used anti-malarial drug such as quinine in order to see if these liposomes are a comparable model for the disease. Quinine is due to its toxicity to the malarial pathogen and acts by interfering with the parasite's ability to metabolize hemoglobin.[154] We can quantify the passive diffusion of quinine molecules from the cytosolic milieu of the droplets into the exoplasmic region. The UV absorption of quinine peaks around 350 nm and fluorescent emission peaks at around 460 nm. Due to the small size of the droplets, the passive diffusion of quinine can be over the course of an hour.[152,155] These results will then be compared to the results in true red blood cells.[156]

4.4 Conclusions

Here I outlined a functional microfluidic platform and surface treatment regime for the formation of liposomes made with lipids in either the oil phase (as is the precedent in the literature) and in the aqueous phases. I also showed that this platform can be used for the generation of asymmetric liposomes as a step towards the modelling of artificial red blood cells using microfluidic techniques. I then provided a detailed outline of the work which I aspire to complete, and publish, in the following months. More specifically, I expect to determine a functional and biomimetic lipid solution for the formation of artificial red blood cells using asymmetric liposomes. I hope to apply these artificial red blood cells to study malarial drugs such as quinine. Overall, my methodology has the potential to open up a route to the fabrication of synthetic cells capable of modelling the passive diffusion of clinically relevant drugs. This work also has the potential to be used as an additional screening process and cut down on the high costs associated with drug development.

4.5 Materials and methods

The microcapillary device outlined in this chapter was assembled in an identical manner to those described in Chapter 3 and Chapter 5 of this dissertation. The fabrication of the silicon wafer moulds and the PDMS devices, as well as the surface treatment of the PDMS devices.

4.5.1 Materials

All reagents were used as received unless otherwise stated. Poly(vinyl alcohol) (PVA, MW = 13 000–23 000 g/mol^{-1}, 87–88% hydrolyzed), 1,2-dioleoyl-sn-glycero-3-phosphocholine, 1l-α-phosphatidylcholine (egg), and phosphatidylethanolamine (egg) were

purchase from Sigma Aldrich. Integra Miltex Standard Biopsy Punches and Pluoronic F-68 were purchased from Thermo Fisher Scientific. PTFE tubing (1/16 inch outer diameter, 750 μm inner diameter) was purchased from Chromatographic Specialties Inc. Jensen global 20 and 30 gauge IT series blunt stainless steel needles were purchased from Howard Electronics. 1 mL glass gas-tight syringes (model 1001 TLL, PTFE Luer Lock) were purchased from Hamilton. Polyethylene glycol (PEG, MW = 6000 g/mol^{-1}) was purchased from VWR. 2-[methoxy(polyethyleneoxy)6-9 propyl]trimethoxysilane was purchased from Gelest. Polyurethane resin (Vytaflex 30) and release spray were purchased from Smooth-on. Iroshizuku Fountain Pen Ink (Vermillion Red and Light Blue) was purchased from Amazon. Glass capillaries were purchased from Vitrocom. 100 nm polycarbonate filters and Avanti Mini Extruder were purchased from Avanti Lipids.

4.5.2 Surface treatment of glass microcapillaries

First, the outer capillaries were cleaned with soapy deionized (DI) water, DI water, isopropanol, ethanol and acetone. The capillaries were then dried with a filtered air gun and placed in a glass petri dish on a hot plate at 95°C for 30 minutes. The capillaries were then plasma treated at 100 W with air plasma for one minute. Capillaries were chemically modified immediately after plasma treatment. The glass capillaries were submerged fully in 2-[methoxy(polyethyleneoxy)6-9 propyl]trimethoxysilane for approximately 15 minutes to generate a hydrophilic surface. Afterwards, the excess silane was dabbed off with Kim wipes and dried using a filtered air gun.

4.5.3 Lipid solution preparation

The lipids were extruded into an aqueous 4-(2-hydroxyethyl)-1-piper azineethanesulfonic acid (HEPES) buffer. HEPES is a commonly used buffer in cells culture as it

is a high efficient buffer.[157] It is also commonly used for DIBs droplet formation.[158] First, lipids re-suspended in chloroform were pipetted into a glass a 10 mL round bottom flask. The excess $CHCl_3$ is removed via evaporation using a steady stream of filtered air with the air gun. The flask is the placed in a glass desiccator and is placed under vaccum for 1 hour. Afterwards, 1 mL of HEPES buffer was added to the flask and the solution was vortexed for 30 s. The solution was then subjected to 5 freeze-thaw cycles in liquid nitogen and warm water, respectively. Next, the lipids are extruded 21 times in order to create unilamellar liposomes. All lipids were prepared at 10 mg mL^{-1}. The surfactant aqueous solutions were prepared separately. For the inner phase and outer phase solutions, 8 wt% PEG/ 2 wt% PVA and 10 wt% PVA, respectively, were added to deionized water in glass vials. A magnetic stir bar was added and the solutions were mixed together at 95 °C for 30 minutes until the surfactants/stabilizers were fully dissolved. Afterwards, 10 mg mL^{-1} of lipid solution was added to the mixture at a 1:1 ratio to result in a 5 mg mL^{-1} inner and outer lipid solutions with added surfactants.

For the control liposomes with lipids in the middle solvent phase, the inner phase consisted of 8 wt% polyethylene glycol and 2 wt% poly(vinyl alcohol). The middle phase consisted of a mixture of chloroform and hexane (50:50 v/v) with added 12.5 mg mL^{-1} 1,2-Dioleoyl-sn-glycero-3-phosphocholine (DOPC). DOPC was at a high concentration as we have observed in our group that these concentrations of synthetic lipids will more robustly produce bilayers.[158] The outer phase consisted of 10 wt% PVA with 0.5 wt% Pluronic F-68. For the liposomes with lipids in the inner and outer aqeuous phases the inner phase consisted of 8 wt% polyethylene glycol (PEG), 2 wt% poly(vinyl alcohol) (PVA) with 5 mg mL^{-1} of DOPC (pruple lipids). The middle phase consisted of a mixture of chloroform and hexane (50:50 v/v) (light brown middle). The outer phase consisted of 10 wt% PVA, 0.5 wt% Pluronic F-68

and 5 mg mL^{-1} of DOPC (purple lipids). For the asymmetric liposomes with lipids in the inner and otuer aqeuous phases, the inner phase consisted of 8 wt% polyethylene glycol (PEG), 2 wt% poly(vinyl alcohol) (PVA) with 5 mg mL^{-1} of PE (purple lipids). The middle phase consisted of a mixture of chloroform and hexane (50:50 v/v) (light brown middle). The outer phase consisted of 10 wt% PVA, 0.5 wt% Pluronic F-68 and 5 mg mL^{-1} of PC pink lipids). Figure 4.7b shows the schematic for the fully formed liposome after the de-wetting of the middle phase. Solutions can be stored ready for use in the fridge for up to a week. Mixing together the lipid and surfactant stabilizer solutions must be done directly prior to use.

4.5.4 Assembly of the modular microcapillary platform for liposome generation

The microcapillary device for the liposomal generation was assembled using distinct glass capillary sizes than those outlined in Chapter 2. A 0.20 mm ID glass capillary was used for the inner phase. It was heat ligated to 0.25 mm ID PTFE tubing. 0.75 mm ID PTFE tubing was used for the middle phase. 1.5 mm ID surface treated glass microcapillary was used for the outer phase.

4.5.5 Liposome formation and visualization

Liposomes were formed in the same way for all experiments. First, the three solutions (outer aqueous, middle solvent and inner aqueous) were inserted into three separate 1 mL gastight glass syringes (Hamilton). These syringes were connected to the syringe tips which linked to the microcapillary device as highlighted in Figure 4.4a. The flow rate was controlled using neMESYS low pressure syringe pumps (Cetoni). I set the outer phase flow rate to 200 μL^{-1}, the middle phase flow rate to 40 μL^{-1} and the inner phase flow rate to 20 μL^{-1}. Droplet formation on the microcapillary was visualized

using a stereomicroscope (SMZ800N, Nikon). Double emulsions were collected in a clean glass watch, which contained 1 mL of water, glass directly from the device. Special care must be taken during double emulsion collection from the microcapillary device so as to not accidentally shear the double emulsions prior to de-wetting. The double emulsion de-wetting process was visualized by mounting the glass watch glass on a Ti-U microscope (Nikon). Images and videos were captured using a Phantom high-speed camera.

Chapter 5

Programmed assembly of bespoke prototissue spheroids on a microfluidic platform

While important breakthroughs in prototissue engineering have recently been achieved, the precise assembly of protocell building blocks into prototissues that are stable in water, are capable of sensing the external environment, and display collective behaviours still remains a considerable challenge. In this work we explore the use of microfluidic technologies for the programmed assembly of bio-orthogonally reactive protein-polymer protocells into prototissue spheroids of precise size and composition. We found that these prototissues, when generated using microfluidics, take on unique Janus-like configurations. We then showed that by controlling the number and phenotype of the protocells that compose the prototissue spheroids it is possible to modulate both the amplitude of the thermally induced contractions of the material, as well as its collective endogenous biochemical reactivity. Our results showed that microfluidic

technologies enable a new route for the precise and high-throughput fabrication of synthetic tissues with programmable collective properties that can be tuned through the careful assembly of protocell building blocks of different phenotypes.

I performed all of the experimental work. Jae Levy (an undergraduate student in the group) assisted with the enzyme experiments. Dr Gobbo provided the BSA nanoconjugates and consulted on experimental details. Dr Elvira and I analysed the data. Dr Elvira, Dr Gobbo and I wrote the manuscript. More specifically, I wrote the first draft in its entirety. Dr Elvira and I then heavily edited the first draft together. Then, the more chemistry-heavy sections were edited by Dr Gobbo. All authors reviewed the manuscript. This work was submitted to Chemical Science on 02/03/21 and is currently under review.

5.1 Introduction

This past decade has shown a surge of work in the field of bottom-up synthetic biology. The majority of the work seeks to address the gap between biology and chemistry in order to better understand how non-living building blocks become life. To do this, attempts have been made to construct what are called non-typical protocells. These are non-living cell-like entities are created from scratch using only a limited toolbox of molecules, materials, and chemical reactions.[70,159,160]

To date, researchers in bottom-up synthetic biology have engineered a range of different non-typical protocells based on lipid vesicles,[161,162] polymersomes,[163–165] polypeptide capsules,[30] dendrimersomes,[166] inorganic colloidosomes,[167,168] and coacervate microdroplets.[169–171] Among these, proteinosomes are an emerging non-typical protocell model, which, similarly to colloidosomes, are generated as Pickering emulsions. Pro-

teinosomes have a semi-permeable and elastic membrane which consists of a closely packed single layer of conjugated bovine serum albumin/poly(N-isopropylacrylamide) (BSA/PNIPAM) amphiphilic nanoparticles. The BSA/PNIPAM membrane is then chemically crosslinked with PEG-bis(N-succinimidyl succinate) (PEG-diNHS) and the proteinosomes can then be transferred into a water media. Most importantly, proteinosomes can be engineered to display protocellular properties such as selective permeability,[167,168,172] gene-directed protein, synthesis[26,27] internalized enzyme catalysis,[24,25] predatory behaviours,[127] and reversible contractility.[173]

In recent years there has been increasing interest in devising methodologies to assemble protocells into tissue-like materials called prototissues that are capable of communicating both internally and with the external environment and display rudimental collective behaviours. Li *et al.* used magnetic fields to manipulate diamagnetic giant unilamellar lipid vesicles (GUVs) into coded configurations on a scale of micrometers.[86] Wang et al. showed that micro-arrays of hemi-fused GUVs could be patterned *via* acoustic standing waves. Their work contributed significantly towards the fabrication of prototissues with controlled geometries and lattice dimensions.[174] Alcinesio *et al.* developed a 3D printing technique to pattern water-in-oil droplets connected *via* interface bilayers (DIBs) into synthetic tissues.[93] They were also able to demonstrate that DIBs were capable of membrane protein-mediated electrical communication, deformation, and light-induced gene expression.[93]

While these different approaches have provided important breakthroughs in prototissue design and synthetic construction, they are not without their drawbacks. The diamagnetic GUVs require aqueous media containing high levels of toxic $MnCl_2$ and a constant magnetic field to maintain the patterns. They are not stable in *in vivo* conditions and, as such, are not indicative of true life-like structures. In the same

vein, the work by Wang *et al.* requires the standing waves to be constantly applied to avoid a rapid re-dispersal of the GUVs into the bulk solution. Lastly, the 3D-printing of DIBs requires the presence of an external bulk oil phase, which hinders potential applications, and limits the shelf-life of these prototissues.

An important breakthrough towards the generation of free-standing prototissues that are stable in water and capable of communicating both internally and with the external environment was made by Gobbo *et al.*[78] They developed a synthetic approach to the programmed assembly of small prototissue spheroids ($\sim$75–200 μm in diameter) based on the interfacial bio-orthogonal adhesion (alkyne-azide click-chemistry) of two populations of reactive proteinosomes. They then showed that the thermoresponsive properties of the interlinked proteinosomes could be used collectively to generate prototissue spheroids capable of reversible contractions, which could be enzymatically modulated and exploited for mechanochemical transduction. However, the bulk emulsification method they used was based on the manual shaking of a vial and did not allow control over the number of proteinosomes that composed the prototissue spheroids nor their spatial organisation. This severely limited their ability to further investigate and modulate this interesting collective property of the material.

Driven by these observations, in this work we explore the use of microfluidic techniques for the programmed assembly of bio-orthogonally reactive proteinosomes into prototissue spheroids of bespoke size and composition. Microfluidic tools have been largely used for the bottom-up synthesis of non-typical protocells,[175–177] including proteinosomes.[41] However, they are yet to be exploited for the generation of tissue-like materials. Herein we report the first example of a microfluidic platform for the simultaneous fabrication of two bio-orthogonally reactive protocell populations with high throughput and narrow size distribution, and their assembly into proto-

tissue spheroids with high control over their composition and 3D architecture. Our microfluidic platform allowed us to systematically vary the number of constituent azide- and BCN-functionalised protocells from 1 to 10 as well as their ratio within each prototissue. Importantly, this was instrumental to elucidate the key role of bio-orthogonal adhesions in the mechanism of the thermally induced collective contractility of the prototissue spheroids, and fine tune the amplitude of the reversible contractions. Moreover, we also show that by controlling the number and phenotype of the protocells that compose the prototissue spheroids, it was also possible to modulate the collective endogenous biochemical reactivity of the overall tissue-like material.

Our results show that microfluidic techniques provide otherwise unattainable opportunities and insight into prototissue engineering. Our microfluidic platform opens up a route to the fabrication of robust prototissue spheroids, whose emergent bio-inspired capabilities can be carefully programmed and modulated by precisely assembling together protocell building blocks of different phenotype.

5.2 Results and discussion

5.2.1 A microfluidic platform for the creation of bespoke prototissue spheroids

The microfluidic platform for the formation of bespoke prototissue spheroids was fabricated from polydimethylsiloxane (PDMS) using conventional soft lithography techniques. The platform consists of three flow focusing junctions, each of which had an inlet channel, two carrier phase channels that created the shear forces necessary to generate droplets, and an exit channel (Figure 5.1a). Initially, two identical flow

focusing junctions placed in parallel were used for the formation of proteinosomes, which are W/O Pickering emulsion droplets stabilised by either RITC-labelled azide-functionalised BSA/PNIPAM-co-MAA nanoconjugates (red fluorescence) or FITC-labelled BCN-functionalised BSA/PNIPAM-co-MAA nanoconjugates (green fluorescence) and chemically crosslinked with a PEG-diNHS crosslinker. Each of these flow focusing junctions was composed of a 50 μm wide inlet channel which fed a solution of bio-orthogonally reactive protein-polymer nanoconjugate (8 mg mL^{-1}) and PEG-diNHS (160 mg mL^{-1}) in Na_2CO_3 buffer (100 mM, pH 8.5) to the junction, two 50 μm wide carrier phase channels through which the oil phase flowed, and a 100 μm wide exit channel with a pinched entrance section that was 25 μm wide (Figure 5.1a).

A third flow focusing junction was placed in series and was used for the encapsulation of the azide- and BCN-functionalised proteinosomes in oil to form W/O/W Pickering emulsion droplets stabilised by an unlabelled BSA/PNIPAM-co-MAA outer membrane. This flow focusing junction was composed of a 200 μm wide inlet channel (from the combination of the two 100 μm wide channels carrying the W/O droplets), two 200 μm wide channels for the aqueous carrier phase (a solution of non-bio-orthogonally reactive unlabelled BSA/PNIPAM-co-MAA nanoconjugate at a concentration of 8 mg mL^{-1}), and a 400 μm wide exit channel with a pinched 200 μm wide entrance (Figure 5.1a). The large width of the exit channel allowed for the encapsulation of up to 10 proteinosomes within one outer membrane. In contrast to the first two flow focusing junctions, in this flow focusing junction the inlet channel (which carries the proteinosomes) and the carrier phase channels (which carry the oil phase) were specifically designed to be perpendicular to each other to generate high enough shear forces for the creation of the W/O/W droplets.

In all three flow focusing junctions, an increase in the diameter of the exit channels

was required to slow down the flow rate in accordance with Poiseuille's equation. Moreover, the region between the two sets of flow focusing junctions could not contain a meander, so as to avoid unnecessary sticking of W/O emulsion droplets to the channel, and had to be long enough to allow the stabilisation of the proteinosome droplets. At all flow focusing junctions, the combination of the slower flow rate and the shear forces created by the pinching flows of the carrier phases allowed for the formation of single W/O or multiple W/O/W emulsion droplets stabilised by different types of BSA/PNIPAM-co-MAA nanoconjugates. The final notable feature of the microfluidic platform was a meander, which was used to image the W/O/W droplets. Additionally, the curves in the meander increased shear forces and enabled droplet creation for large prototissue spheroids.

Surface treatment of the microfluidic channels was key for the generation of stable proteinosomes and prototissue spheroids. The section of the microfluidic platform used for the creation of proteinosomes was kept hydrophobic, whereas the section of the platform used for the creation of prototissue spheroids was made hydrophilic through surface treatment with polyvinyl alcohol (PVA, 0.01 mg mL^{-1}). Additionally, it was important to prime the hydrophilic channels with the unlabelled BSA/PNIPAM-co-MAA nanoconjugate solution (8 mg mL^{-1}) prior to inserting the oil phase so as to stabilise the formation of prototissue spheroids.

The azide- and BCN-functionalised proteinosomes produced by the two first flow focusing junctions had a very narrow size distribution and a diameter of 45.07 $\pm$ 1.89 μm and 45.66 $\pm$ 1.90 μm, respectively (Figure 5.1b, c). Comparison of these results with those obtained for proteinosomes produced using a bulk methodology, as expected, showed a significant decrease of the relative standard deviation of the size distributions from 72.71% and 69.50% to 4.20% and 4.17%, respectively. These

results compare well with data reported from a microfluidic platform used to fabricate one type of non-bio-orthogonally reactive proteinosomes from a BSA/PNIPAM nanoconjugate (27.1±1.0 μm in diameter, relative standard deviation 3.7%).[41]

The design of the third flow focusing junction allowed us to create W/O/W emulsion droplets that encapsulated a pre-determined number of azide- or/and BCN-functionalised proteinosomes that could be varied from 1 to 10 (Appendix B, Figures B.12-B.17). This level of control was achieved by systematically decreasing the flow rate of the outer aqueous phase. For example, a mono-compartmental W/O/W droplet containing a single azide- or BCN-functionalised proteinosome enclosed within an unlabelled BSA/PNIPAM-co-MAA outer membrane could be formed by setting the flow rate of the outer aqueous phase to 330 μLmin^{-}1, the flow rate of the oil phase to 6 μLmin^{-}1, and the flow rates of the two inner aqueous phases to 1 μLmin^{-}1 each. Multicompartmental W/O/W droplets with increasing numbers of azide- and/or BCN-functionalised proteinosomes could be generated by sequentially decreasing the flow rate of the outer aqueous phase by 20 μLmin^{-}1 and keeping the flow rates of the oil phase and of the inner aqueous phases the same (6 μLmin^{-}1 and 1 μLmin^{-}1 each, respectively). Figure 5.1d shows brightfield (left) and fluorescence microscopy images (right) of six different W/O/W emulsion droplets generated using this methodology. The number of enclosed proteinosomes was systematically varied from 1 to 2, 4, 6, 8 and 10, and the proteinosome fraction of the multicompartmental W/O/W droplets, defined as the ratio between enclosed azide-functionalised proteinosomes and the total number of enclosed proteinosomes, was kept at 0.5. We called these emulsion droplets mono-, 1a,1b bi-, 2a,2b tetra-, 3a,3b hexa-, 4a,4b octa-, and 5a,5b deca-compartmental W/O/W droplets, respectively. The nomenclature is as follows: the number of azide-functionalised proteinosomes "a") and BCN-functionalised proteinosomes ("b") is specified at the beginning of the name. This is followed by the

suffix (bi-, tri-, tetra-, penta-, etc.), which indicates the total number of proteinosomes enclosed in each W/O/W droplet. The precision and accuracy with which we could enclose the desired number of proteinosomes was found to progressively decrease with the increasing target number of enclosed proteinosomes (Figure 5.1e). For example, while an individual azide- or BCN-functionalised proteinosome could be enclosed within a BSA/PNIPAM-co-MAA outer membrane with 100% accuracy and precision, a 1:1 binary population of 5 azide- and 5 BCN-functionalised proteinosomes could be enclosed with only 10% success. However, since the microfluidic platform could produce between 5 and 15 W/O/W droplets per second, we were able to generate between 9,000 and 27,000 deca-compartmental W/O/W droplets in only 30 minutes (Appendix B, Figure B.18).

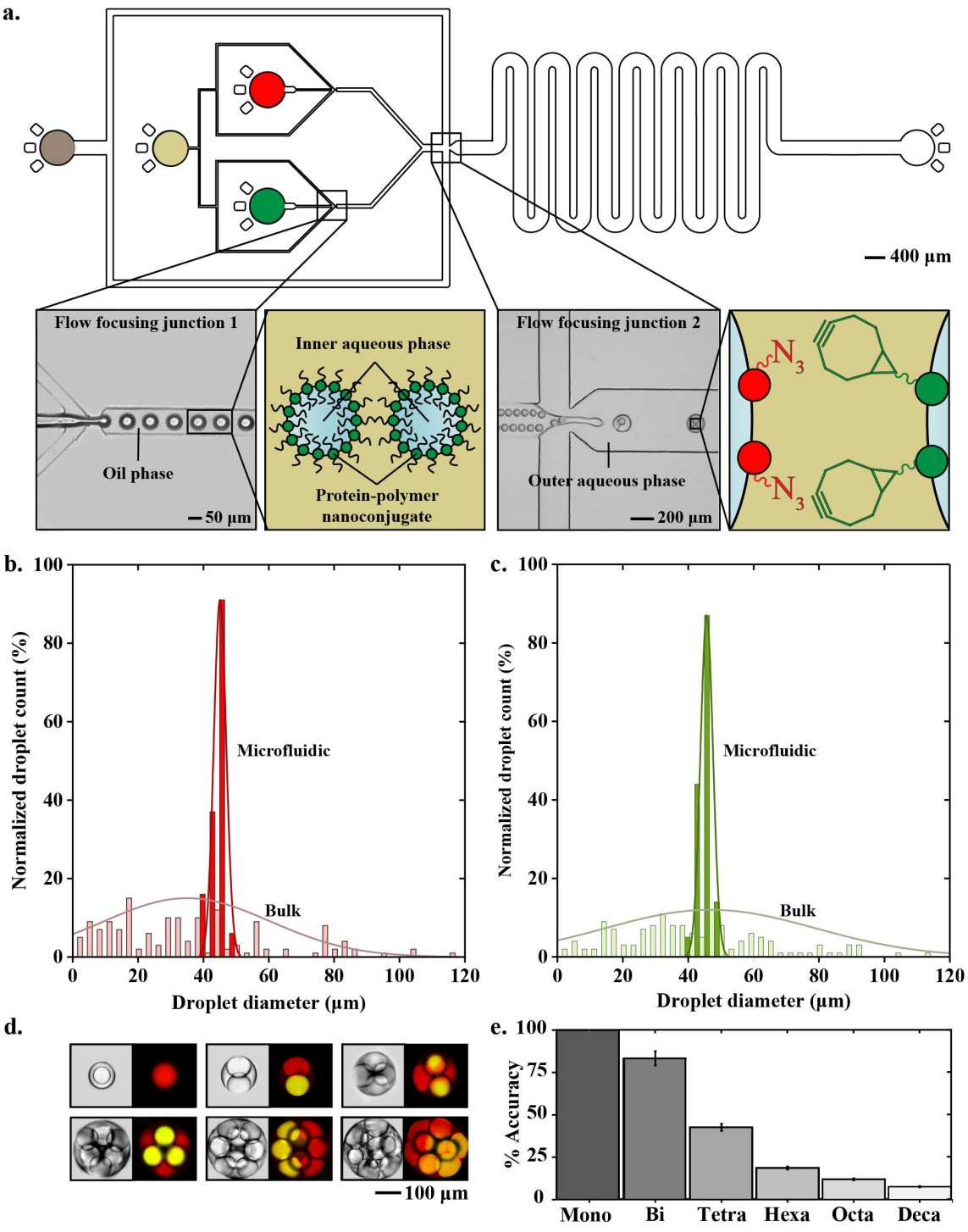
a.
400 µm
Flow focusing junction 1
Oil phase
50 µm
Inner aqueous phase
Protein-polymer nanoconjugate
Flow focusing junction 2
Outer aqueous phase
200 µm
N3
N3
b.
Normalized droplet count (%)
Microfluidic
Bulk
Droplet diameter (µm)
c.
Normalized droplet count (%)
Microfluidic
Bulk
Droplet diameter (µm)
d.
100 µm
e.
% Accuracy
Mono
Bi
Tetra
Hexa
Octa
Deca

Figure 5.1: **Microfluidic generation of prototissue spheroids** a, Scheme showing the design of our microfluidic platform. The inner phases of the two parallel flow focusing junctions at the center of the device were comprised of either an aqueous solution of RITC-tagged azide-functionalised BSA/PNIPAM-co-MAA nanoconjugate (8 mg mL^{-1}) and PEG-diNHS (160 mg mL^{-1}) (inlet highlighted with a red circle, top) or an aqueous solution of FITC-tagged BCN-functionalised BSA/PNIPAM-co-MAA nanoconjugate (8 mg mL^{-1}) and PEG-diNHS (160 mg mL^{-1}) (inlet highlighted with a green circle, bottom). The oil phase (inlet highlighted with a yellow circle) was 2-ethyl-1-hexanol. The outer aqueous phase of the third flow focusing junction (inlet highlighted with a brown circle, left) was comprised of a solution of non-tagged non-bio-orthogonally reactive BSA/PNIPAM-co-MAA nanoconjugate. Droplet formation at both types of flow focusing junctions are shown with insets containing microscopy images of the droplets on the microfluidic device and a scheme explaining the composition of the droplets. At the first two flow focusing junctions (left), proteinosomes were formed as W/O emulsion droplets with BSA nanoconjugates forming a Pickering emulsion on the droplet surface. At the third flow focusing junction (right) a 1a,1b bi-compartmental emulsion was formed, from one FITC-tagged proteinosome and one azide-tagged proteinosome. b, Graph comparing the size distributions of W/O emulsion droplets (determined using ImageJ) stabilised by azide-functionalised BSA/PNIPAM-co-MAA nanoconjugates produced in the microfluidic device (dark red) with the same droplets formed by manually shaking a vial (bulk method, light red). **c)** Graph comparing the size distributions of W/O emulsion droplets stabilised by BCN-functionalised BSA/PNIPAM-co-MAA nanoconjugates produced in the microfluidic device (dark green) with the same droplets formed using the bulk method (light green). For both graphs, each plot contains at least 150 data values which were measured using ImageJ, and the curves represent the fitted Gaussian distributions. d) Brightfield (left) and fluorescent (right) microscopy images of mono- and Multicompartmental W/O/W emulsion droplets. From top left to bottom right: W/O/W emulsion droplet containing a single RITC-labelled azide functionalised proteinosome (red fluorescence), bi-, tetra-, hexa-, octa- and deca-compartmental W/O/W emulsion droplets with equal numbers of RITC-labelled azide- (red fluorescence) and FITC-labelled BCN-functionalised proteinosomes (green fluorescence). e) Graph showing the analysis of the device performance for the generation of targeted Multicompartmental W/O/W emulsion droplets. For each type of emulsion droplet, data was acquired on three different microfluidic devices. In each case, a total of 90 W/O/W emulsion droplets were analysed using ImageJ. Error bars represent the standard deviation

The microfluidic platform allowed us to spatially divide a 1:1 binary population of bio-orthogonally reactive proteinosomes enclosed within the unlabelled BSA/PNIPAM-co-MAA outer membrane, resulting in multicompartmental W/O/W emulsion droplets with a Janus configuration (Figure 5.1d). This was achieved by designing the third flow focusing junction so that the two inlet streams containing each type of proteinosome joined together in a single inlet channel without mixing, with the RITC-labelled azide-functionalised proteinosomes lined up in the top half of the channel and the FITC-labelled BCN functionalised proteinosomes lined up in the bottom half of the channel. Appendix B, Figure B.19 shows how the proteinosomes enclosed within the outer membrane of the droplet moved according to well-known flow recirculation effects.[178] Due to the symmetry of the inner droplet flux, they did not mix; this resulted in the maintenance of the predetermined Janus-like organisation. Being able to generate Janus multicompartmental emulsion droplets by spatially assembling proteinosome building blocks with high precision is an important achievement

in bottom-up synthetic biology. This allows us to break up the symmetry of the proto-tissue spheroids, opening a route, for example, towards the generation of endogenous gradients of chemical signals.

Our microfluidic platform not only enabled us to control the total number of proteinosomes that composed the W/O/W Pickering emulsion droplets, but it also allowed us to create multicompartmental systems of tailored composition with any predetermined proteinosome fraction. This could be achieved by changing the ratio between the flow rates of the two inner aqueous phases carrying the bio-orthogonal protein-polymer nanoconjugates once the flow rate of the outer phase relative to the middle phase was set to encapsulate the desired total number of proteinosomes. For example, if the desired ratio was 3 RITC-labelled azide- and 1 FITC-labelled BCN-functionalised proteinosomes, then the flow rate of the RITC-labelled azide- inner phase needed to be 3 times greater than that of the FITC-labelled BCN- inner aqueous phase. Hence, to fabricate these 3a,1b tetra-compartmental W/O/W droplets, the flow rate of the inner aqueous phase containing the RITC-labelled azide-functionalised BSA/PNIPAM-co-MAA nanoconjugate was set to 0.75 μLmin^{-}1, whereas the flow rate of the inner aqueous phase containing the FITC-labelled BCN-functionalised BSA/PNIPAM-co-MAA nanoconjugate was set to 0.25 μLmin^{-}1. Figure 5.2 shows a library of all possible combinations of W/O/W emulsion droplets with a total number of proteinosomes between 1 to 10 that could be generated using our microfluidic platform. All combinations showed the preferential Janus-like configuration of the internal proteinosome building blocks. This figure shows representative images from highly reproducible data. Notably, due to the control offered by our microfluidic platform, the three-dimensional (3D) packing of the proteinosomes can be controlled and predicted. As all proteinosomes are generated in situ with a narrow size distribution (Figure 5.1b and c) the space between them can be assumed to be a three-

dimensional Euclidean space. As a result, the equally packed spheres represented by our proteinosomes self-organise in a lattice. As the total number of proteinosomes in the prototissue increases, we can clearly observe how the proteinosomes form a symmetric, close-packed structure and preferentially form a face-centred cubic lattice. Since our microfluidic platform enables us to form proteinosomes of equal size, we are hence able to make prototissues that are densely packed and have predictable structures as shown in Figure 5.1d and Figure 5.2.

Significantly, in all cases, removal of the encapsulated oil phase via dialysis off-chip enabled the bio-orthogonally reactive proteinosomes enclosed within the unlabelled non-reactive BSA/PNIPAM-co-MAA outer membrane to form covalent adhesion points via the interfacial strain-promoted alkyne-azide cycloaddition (I-SPAAC) reaction developed by Gobbo *et al.*[78] and produce membrane-bound prototissue spheroids that were stable in water. These results show, for the first time, that microfluidic technologies can be used to assemble bespoke prototissue spheroids at high throughput and precise sizes, compositions, and 3D architectures, enabling new possibilities in prototissue engineering.

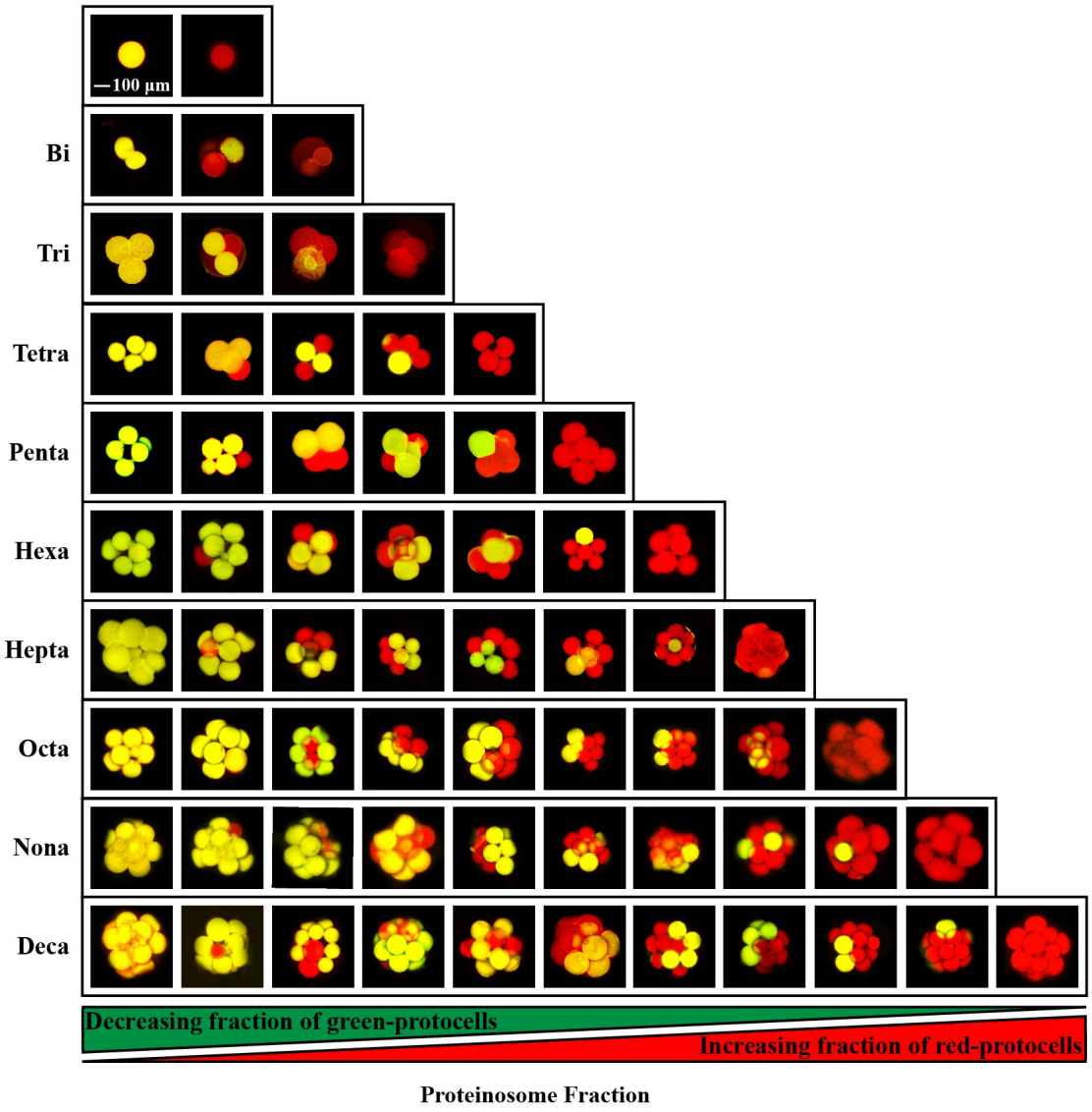

Figure 5.2: **Preferred geometric configurations of bespoke multicompartmental W/O/W emulsion droplets.** Representative fluorescence confocal microscopy images showing single azide and BCN protocells (top) to deca-compartmental W/O/W emulsion droplets (bottom) made from all possible combinations of RITC-labelled azide-functionalised proteinosomes (red fluorescence) and FITC-labelled BCN-functionalised proteinosomes (green fluorescence). On the left hand side of each row, the W/O/W emulsion droplets have the maximum number of FITC-labelled BCN-functionalised proteinosomes. Each subsequent image has a progressively increasing number of RITC-labelled azide-functionalised proteinosomes. On the right hand side of each row, W/O/W emulsion droplets have the maximum number of RITC-labelled azide-functionalised proteinosomes. Images were acquired using at least 3 different microfluidic devices. The scale bar (top left) applies to all images.

5.2.2 Influence of the composition of prototissue spheroids on thermally induced reversible contractions

It has been previously demonstrated that the thermoresponsive properties associated with the crosslinked BSA/PNIPAM-co-MAA nanoconjugate membrane could be exploited collectively to generate synthetic prototissues capable of sustained contractions.[175] Having established that our microfluidic platform allowed us to readily assemble bespoke prototissue spheroids with predetermined proteinosome fractions and with specific 3D architectures, next we explored the possibility of modulating the amplitude of the thermally induced contractions of the prototissue spheroids by varying the proteinosome composition. To achieve this, we used our microfluidic platform to fabricate 21 different samples of bi- to deca-compartmental W/O/W emulsion droplets and systematically changed their composition by changing the proteinosome fraction. Subsequently, the corresponding types of bespoke prototissue spheroids were assembled by forming proteinsome-proteinosome adhesions *via* the I-SPAAC reaction by removing the inner oil phase through dyalisis. All samples were then heated to 47°C, *i.e.* above the lower critical solution temperature (LCST) of PNIPAM-co-MAA which is around 36°C (Figure 5.3), and the temperature-dependent changes in the equilibrium size of all prototissue spheroids were analysed by fluorescence confocal microscopy. LCST tells us the point at which the polymers are solubilized (loose) in solution. Temperatures above this result in the contraction of the polymers. Figure 5.4a (and Figure 5.5, which shows the standard deviation between prototissues) summarises our findings and shows that, in general, the amplitude of the thermally induced volume contractions progressively increases from bi- to deca-prototissue spheroids. Remarkably, for each type of prototissue, when the proteinosome fraction was either 0 (*i.e.* only BCN-functionalised proteinosomes) or 1 (*i.e.* only azide-functionalised proteinosomes) the spheroids displayed the smallest

volume contractions, whereas the volume contractions progressively increased when the proteinosome fraction approached 0.5, that is when the number of constituent azide- and BCN-functionalised proteinosomes was the same. In fact, for the bi-, tetra-, and deca-compartmental prototissue spheroids assembled with a proteinosome fraction of exactly 0.5, we observed the highest volume contractions. More specifically, the amplitude of the contractions passed from *ca.* 10-15 vol% for the 0a,2b (or 2a,0b) bi-compartmental prototissue spheroids to *ca.* 42 vol% for the 1a,1b bi-compartmental prototissue spheroids (an increase of *ca.* 336%); from *ca.* 26-31 vol% for the 0,4 (or 4a,0b) tetra-compartmental prototissue spheroids to *ca.* 51 vol% for the 2a,2b tetra-compartmental prototissue spheroids (an increase of *ca.* 179%); and from *ca.* 42 vol% for the 1a,9b (or 9a,1b) deca-compartmental prototissue spheroids to *ca.* 57 vol% for the 5a,5b deca-compartmental prototissue spheroids (an increase of *ca.* 136%). In contrast, individual azide or BCN-functionalised proteinosomes caged within an outer BSA/PNIPMA-co-MAA membrane contracted only up to 5 $\pm$ 2 vol%. For a visual example of thermoresponsive contractility of these prototissues see Appendix B, Figure B.20.

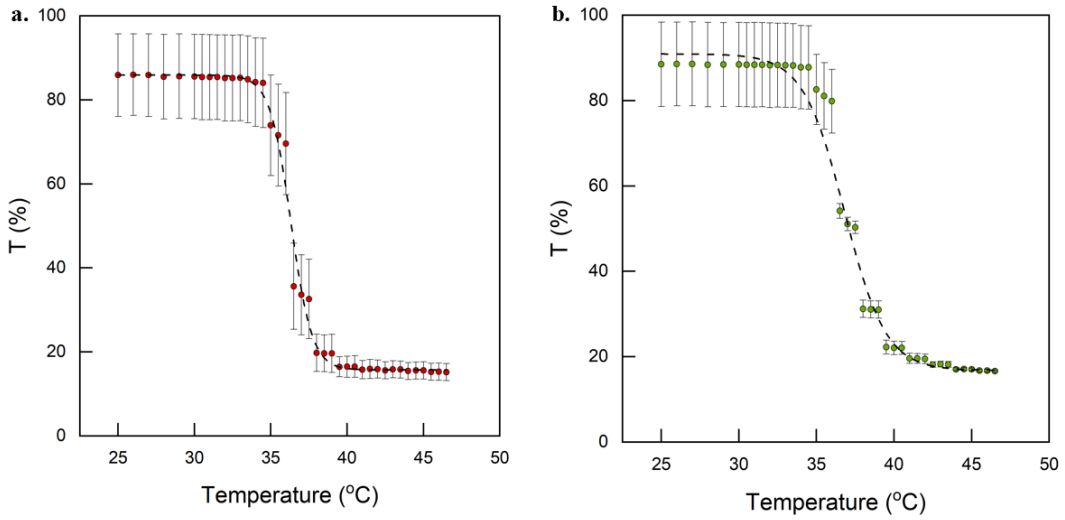

Figure 5.3: **Estimation of lower critical solution temperature (LCST) for the azide- (a) and BCN-functionalised BSA/PNIPAM-co-MAA nanoconjugates (b).** The LCST was estimated by the cloud point temperature (Tcp) of the compounds, which were determined by measuring the transmittance between 400 and 500 nm for a protein-polymer nanoconjugate solution in MilliQ water at a concentration of 1 mg mL-1. The Tcp, taken as 50% of the initial transmittance value, was determined to be 36.3 ± 0.1°C for the azide-functionalised BSA/PNIPAM-co-MAA nanoconjugate, and 36.8 ± 0.2°C for the BCN-functionalised BSA/PNIPAM-co-MAA nanoconjugate. The error bars represent standard deviation.

To further investigate the enhanced volume contractions of the prototissue spheroids assembled at a proteinosome fraction of 0.5, we used the microfluidic platform to fabricate 3a,3b hexa- and 4a,4b octa-compartmental prototissue spheroids. The samples were then heated to 47°C, and the temperature-dependent changes in the equilibrium size of the prototissue spheroids were analysed by fluorescence confocal microscopy. Figure 5.4b summarises our results and shows that the amplitude of the volume contractions rapidly increased from individual proteinosomes enclosed within an unreactive BSA/PNIPAM-co-MAA outer membrane to 1a,1b bi-compartmental prototissue spheroids. However, the amplitude of the contractions across the series reached a threshold limit of *ca.* 60 vol% despite the increasing number of bio-orthogonally reactive proteinosomes at a proteinosome fraction of 0.5. We attribute this to the Janus configuration of the prototissue spheroids, which limits the contact area be-

tween the azide- and BCN- functionalised proteinosome building blocks, especially for larger prototissue spheroids. These observations are consistent with previously reported results for prototissue spheroids of random composition fabricated using bulk methodologies[78] and clearly indicate that the amplitudes of the collective thermoresponsive contractions of the prototissue spheroids are proportional to the number of bio-orthogonal adhesions between azide- and BCN-functionalised proteinosomes. The larger the contact area between the azide- and BCN-functionalised proteinosomes that compose the prototissue, the more enhanced the volume contraction. We attribute this to increased interactions between the PNIPAM-co-MAA chains of bio-orthogonally bound proteinosome membranes, which make the expulsion of water molecules from the material at temperatures above the LCST more effective, with a consequent enhanced contraction of the proteinosome assembly. From a more general perspective, for the first time our microfluidic platform has allowed us to systematically assemble prototissue spheroids with increasing numbers of bio-orthogonal proteinosomes as well as vary the proteinosome fraction to control the amplitude of the prototissue thermally induced collective contractions. Most importantly, this allowed us to provide important experimental results in support of the initial hypothesis of Gobbo *et al.* that the bio-orthogonal adhesions formed through the I-SPAAC reaction between the proteinosome building blocks are primarily responsible for the collective thermoresponsive contractility of the prototissue spheroids.[78]

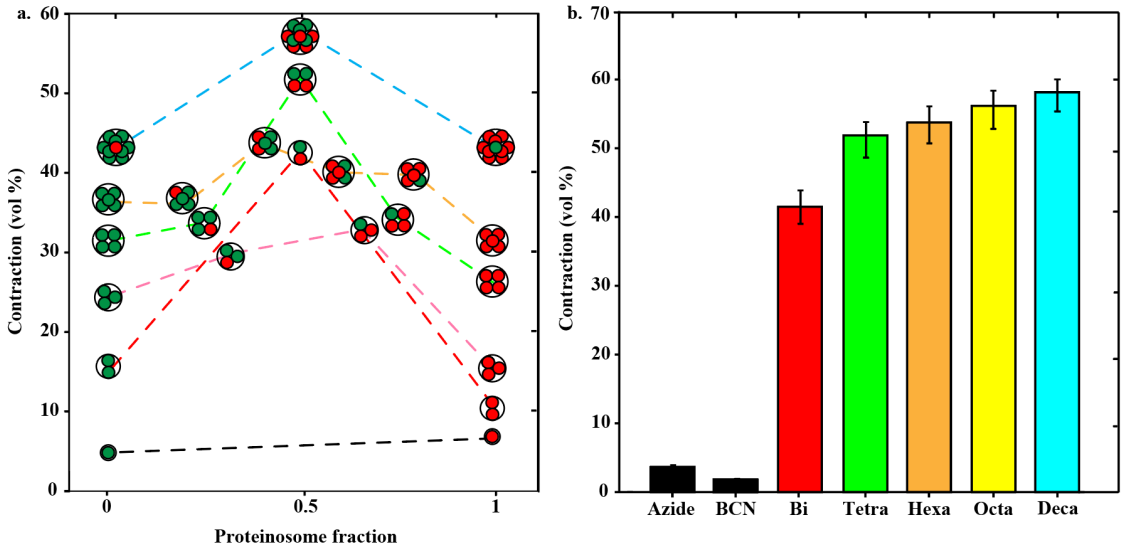

Figure 5.4: **Collective thermoresponsive reversible contractile behaviour of bespoke prototissue spheroids.** a, Graph showing the percent volume contraction of prototissue spheroids of different composition when the temperature is varied from 26°C to 47°C. The x-axis shows the proteinosome fraction, defined as the ratio between the number of azide-functionalised proteinosomes and the total number of proteinosomes in the prototissue spheroid. For clarity, each data point is represented with a cartoon representing the composition of the prototissue spheroid that was measured. Raw data and error analysis are reported in Figure 5.5. b, Graph showing the percent volume contraction for 1a,1b bi-, 2a,2b tetra-, 3a,3b hexa-, 4a,4b octa-, 5a,5b deca-compartmental prototissue spheroids when the temperature is varied from 26°C to 47°C. The "Azide" label refers to a single azide-functionalised proteinosome enclosed within a BSA/PNIPAM-co-MAA outer membrane. The "BCN" label refers instead to a single BCN-functionalised proteinosome enclosed within a BSA/PNIPAM-co-MAA outer membrane. Values are the average of measurements from 3 different prototissue spheroids. Error bars represent the standard deviation.

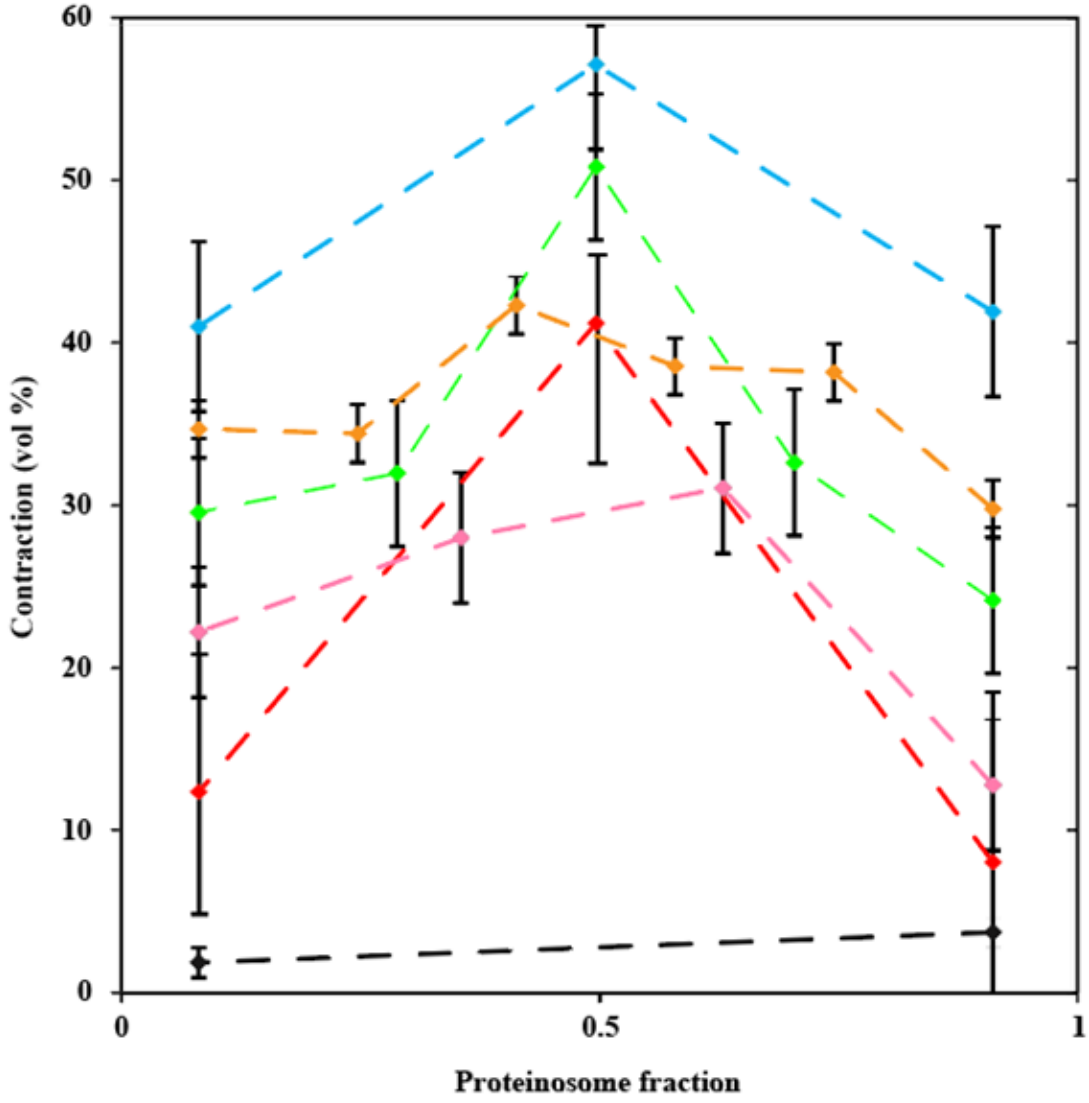

Figure 5.5: **Statistical analysis of thermoresponsive reversible contractile behaviour of bespoke prototissue spheroids.** Graph showing the percent volume contraction in prototissue spheroids of different composition when the temperature is varied from 26°C to 47°C. Black plot: individual azide- and BCN-functionalised proteinosomes enclosed in an BSA/PNIPAM-co-MAA outer membrane; red plot: bi-compartmental prototissue spheroids; pink plot: tri-compartmental prototissue spheroids; green plot: tetra-compartmental prototissue spheroids; yellow plot: penta-compartmental prototissue spheroids; and blue plot deca-compartmental spheroids. Error bars show the standard deviation. The same data are reported in Figure 5.4a.

5.2.3 Modulation of the endogenous biochemical reactivity of prototissue spheroids

Inspired by the above observations, we explored the possibility of exploiting the high control over the prototissue composition provided by our microfluidic platform to regulate the endogenous biochemical reactivity of the prototissue spheroids. To achieve this, we prepared deca-compartmental prototissue spheroids comprising of 5 azide-functionalised BSA/PNIPAM-co-MAA proteinosomes and 5 BCN-functionalised BSA/PNIPAM-co-MAA proteinosomes that were pre-loaded with entrapped glucose oxidase (GOx) or horseradish peroxidase (HRP), respectively. We then added the prototissue spheroids to an aqueous solution containing the proteinosome-permeable molecular substrates glucose (14 mM) and Amplex Red (0.5 mM) to initiate an internalised and spatially coupled GOx/HRP enzyme cascade reaction. In this reaction, glucose and Amplex Red freely diffused through the system and were transformed into gluconic acid and resorufin, respectively (Figure 5.6a). We used UV-vis spectroscopy to monitor the onset of endogenous production of the red resorufin product caused by the completion of the hosted enzyme cascade. Figure 5.6b shows that the onset of red absorbance took place immediately with an initial velocity $v_0 = 200\ \mu M\ s^{-1}$, and reached maximum absorbance after around 30 min. In contrast, control experiments carried out by removing either glucose or Amplex Red showed no increase in absorbance due to the inability of the prototissue spheroids to internally produce the signalling molecule H_2O_2 or to produce a fluorescent output signal, respectively (Figure 5.7). Next, we used our microfluidic platform to create two additional samples of different deca-compartmental prototissue spheroids. The first sample contained prototissue spheroids made from 1 HRP-containing azide-functionalised BSA/PNIPAM-co-MAA proteinosome and 9 GOx-containing BCN-functionalised BSA/PNIPAM-co-MAA proteinosomes, also called an enzymatically

active 1a,9b deca-prototissue spheroid. The second sample contained prototissue spheroids made from 9 HRP-containing azide-functionalised BSA/PNIPAM-co-MAA proteinosomes and 1 GOx-containing BCN-functionalised BSA/PNIPAM-co-MAA proteinosome (enzymatically active 9a,1b deca-prototissue spheroid). Both samples were perfused in an aqueous solution of glucose (14 mM) and Amplex Red (0.5 mM) to initiate the same spatially coupled internalised GOx/HRP enzyme cascade reaction described above. However, this time, due to the different protocellular composition, the initial velocities of the 2 samples were much lower. The enzymatically active 9a,1b, deca-compartmental prototissue spheroid sample had a v_0 of 30 μM s-1, whereas the enzymatically active 1a,9b deca-compartmental prototissue spheroid sample had a v_0 of 100 μM s^{-1} (Figure 5.6b with extra control data in Figure 5.8 and Figure 5.9, respectively). These results show that our microfluidic platform allows us to effectively regulate the endogenous catalytic reactivity of prototissue spheroids by controlling with high precision the number and type of proteinosomes.

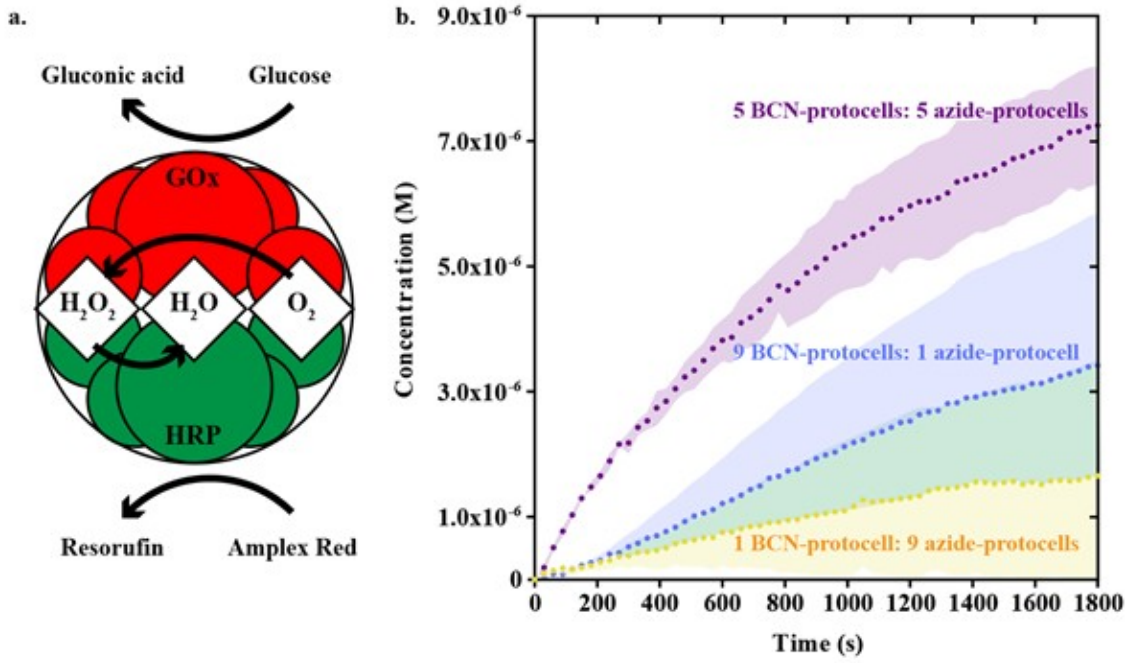

Figure 5.6: **Modulation of the endogenous biochemical reactivity of prototissue spheroids.** a, Scheme showing the GOx/HRP enzyme cascade reaction in a 5a,5b deca-compartmental prototissue spheroid consisting of 5 HRP-containing azide-functionalized proteinosomes (red circles) and 5 GOx-containing BCN-functionalized proteinosomes (green circles). The substrates glucose and Amplex Red freely diffuse through the membranes of the prototissue spheroid. The GOx-containing protocells oxidise glucose to gluconic acid and H_2O_2. This initiates radial diffusion of H_2O_2 from the GOx-containing protocells, which is then used by the HRP-containing protocells to oxidise the non-fluorescent molecules Amplex Red to red fluorescent resorufin. H_2O_2 can therefore be considered as a signalling molecule between the two interlinked protocell communities. b, Graph showing time-dependent changes in the concentration of the final resorufin product for the enzyme cascade described in, a, for a sample of 5a,5b deca-compartmental prototissue spheroids consisting of 5 HRP-containing azide-functionalized proteinosomes and 5 GOx-containing BCN-functionalized proteinosomes (purple plot), a sample of 1a,9b deca-compartmental prototissue spheroids consisting of 1 HRP-containing azide-functionalized proteinosomes and 9 GOx-containing BCN-functionalized proteinosomes (blue plot), and a sample of 9a,1b deca-compartmental prototissue spheroids consisting of 9 HRP-containing azide-functionalized proteinosomes and 1 GOx-containing BCN-functionalized proteinosomes (yellow plot). Data were acquired by UV-vis spectroscopy by measuring the time-dependent changes in absorbance at 560 nm. Experiments were repeated in triplicate. Statistical variation in the data are shown as coloured bands and represent the standard deviation of the data.

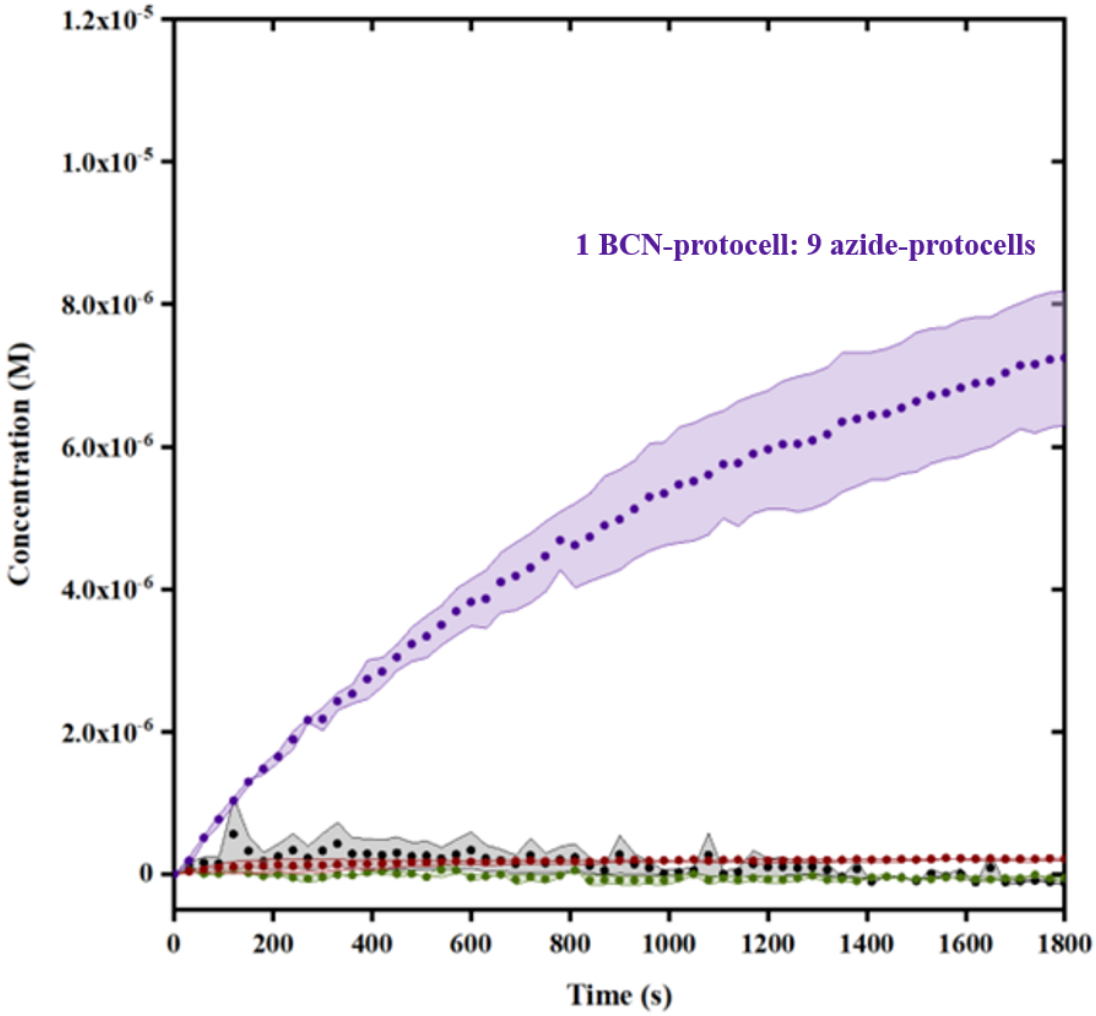

Figure 5.7: **Control data for the GOx/HRP enzyme cascade reaction hosted within a 5a,5b deca-compartmental prototissue spheroid.** The red plot represents a control experiment where only Amplex Red was used (no glucose), the green plot represents a control experiment where only glucose was used (no Amplex Red), the black plot (obscured behind the green data) represents a control experiment in the absence of substrates, and the blue plot reports the experiment where both substrates were present (as shown in Figure 5.6b).

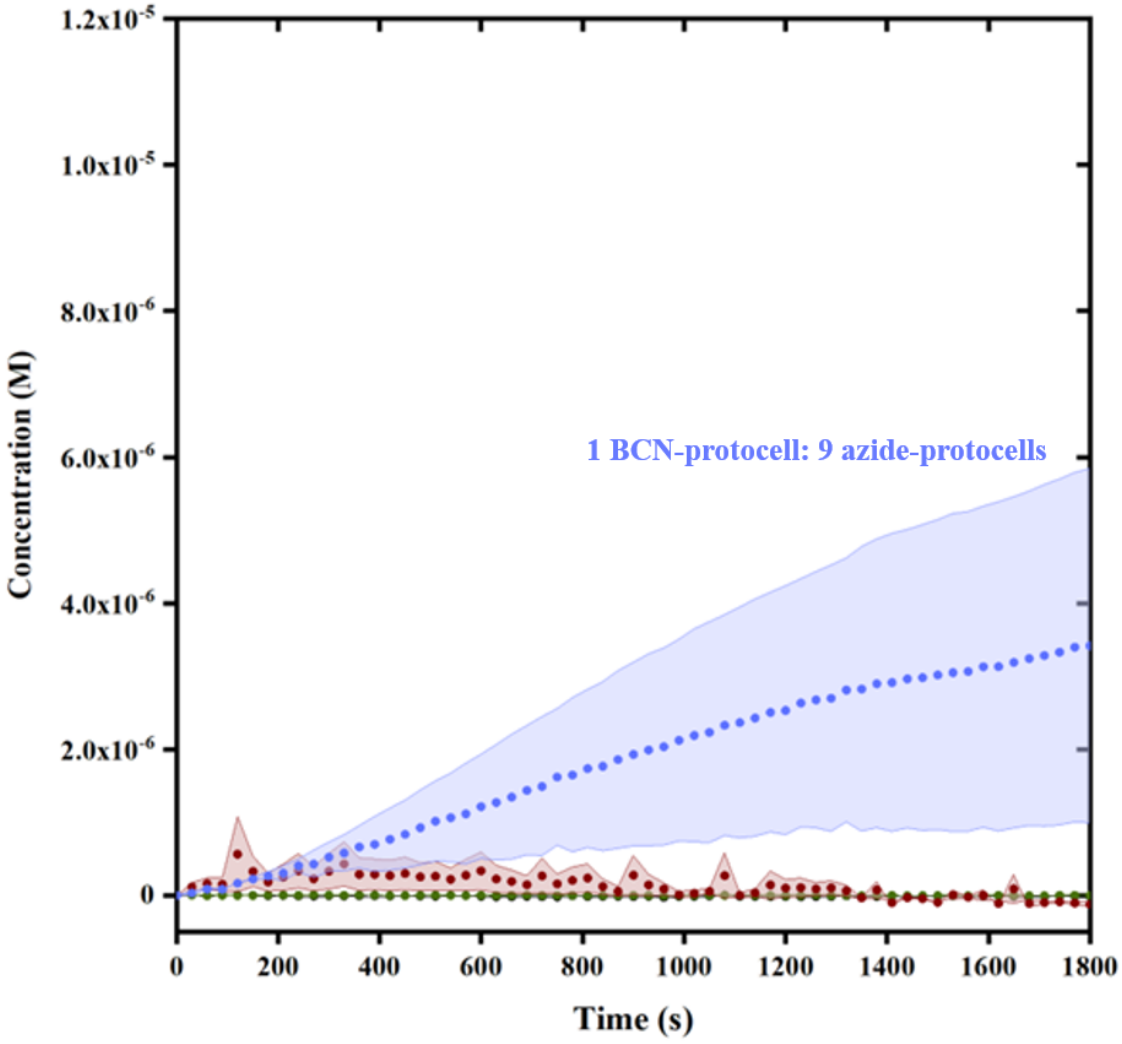

Figure 5.8: **Control data for the GOx/HRP enzyme cascade reaction hosted within a 1a,9b deca-compartmental prototissue spheroid.** The red plot represents a control experiment where only Amplex Red was used (no glucose), the green plot represents a control experiment where only glucose was used (no Amplex Red), the black plot represents a control experiment in the absence of substrates, and the purple plot reports the experiment where both substrates were present (as shown in Figure 5.6b).

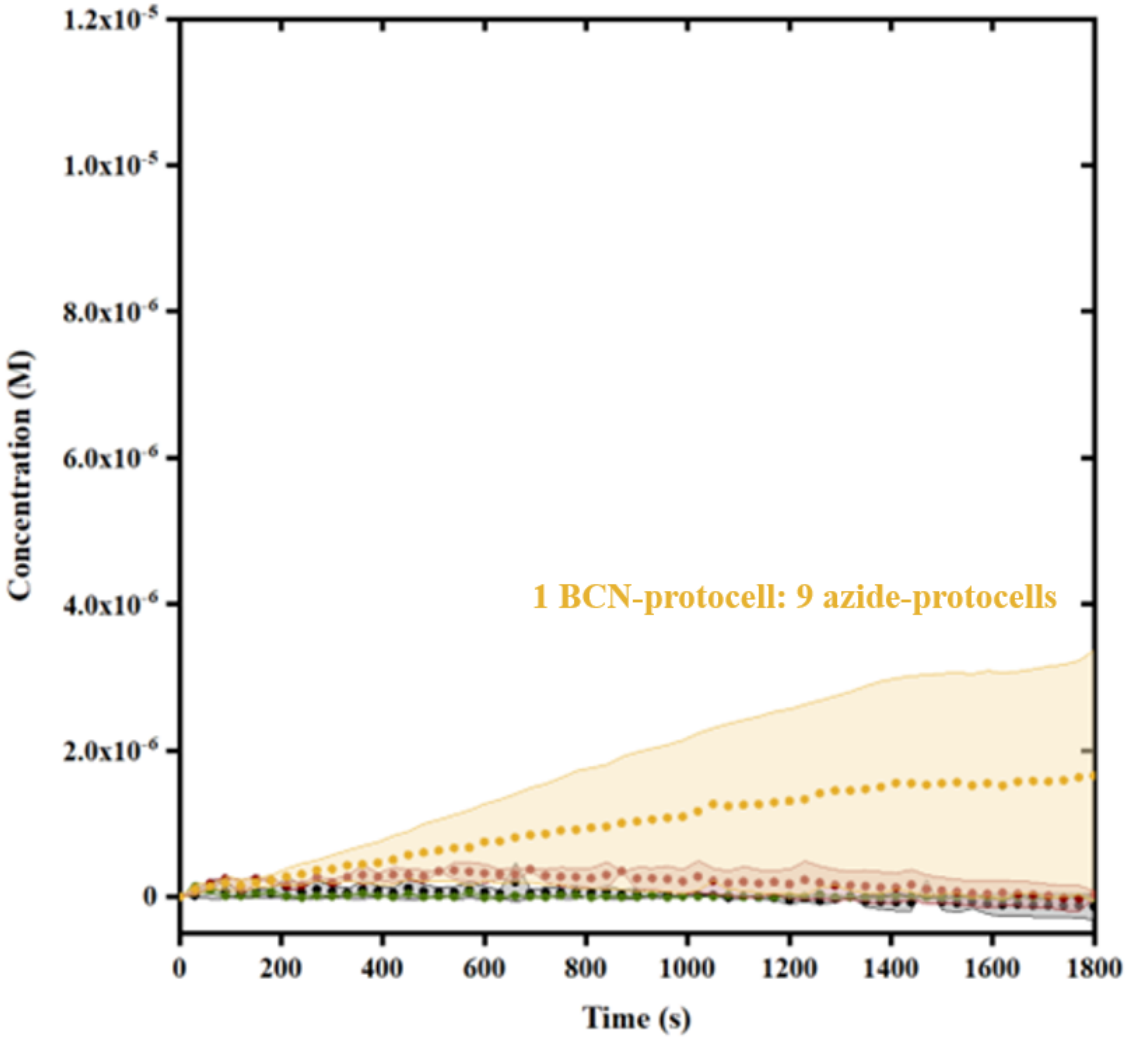

Figure 5.9: **Control data for the GOx/HRP enzyme cascade reaction hosted within a 9a,1b deca-compartmental prototissue spheroid.** The red plot represents a control experiment where only Amplex Red was used (no glucose), the green plot represents a control experiment where only glucose was used (no Amplex Red), the black plot represents a control experiment in the absence of substrates, and the yellow plot reports the positive experiment where both substrates were present (as shown in Figure 5.6b).

5.2.4 Conclusions

In conclusion, we have engineered a novel microfluidic platform that, for the first time, allows for the simultaneous creation of two bio-orthogonally reactive protocell populations with high throughput and narrow size distribution, and their direct assembly into prototissue spheroids with high control over their composition. Notably,

the assembled prototissue spheroids displayed a Janus architecture, which was obtained specifically by lining up the two different types of bio-orthogonally reactive protocells within the microfluidic device. Being able to generate Janus prototissue spheroids through spatial assembly of individual protocell building blocks with high precision is an important achievement in bottom-up synthetic biology. The possibility of segregating different protocell phenotypes within a prototissue architecture will open up a route to the engineering of tissue-like materials capable of chemotactic behaviours,[179,180] and to the generation of endogenous gradients of chemical signals, which could be exploited for the investigation of the physicochemical basis of important biological processes such as embryogenesis, wound healing, and cancer metastasis.

The high control over the assembly of the prototissue spheroids enabled by our microfluidic platform also allowed us to elucidate the key role of bio-orthogonal adhesions in the mechanism of their thermally induced collective contractility and fine tune the amplitude of the contractions. Similarly, we were then able to show that the endogenous biochemical reactivity of prototissue spheroids could be modulated by controlling the number and types of the protocells that compose them. These results open up a new methodology for the fabrication of tissue-like materials with programmable emergent biochemical activities that can be regulated through a careful assembly of protocell building blocks of different phenotypes using a microfluidic platform.

Overall, our results show that microfluidic technologies provide invaluable opportunities in prototissue engineering, allowing for the precise assembly of different protocell types into synthetic tissues with programmable and tuneable collective capabilities. From a more general perspective, the possibility of fine tuning the collective prop-

erties of prototissues by controlling their composition opens up a route to potential applications of this new biomimetic material in biotechnolgy, soft robotics and environmentally beneficial bioreactor technologies.

5.3 Methods

Materials

All reagents were used as received. Trichloromethysilane, 2-ethyl-1-hexanol, sodium bicarbonate, glucose oxidase (GOx) from Aspergillus niger (10000 U), beta-glucose, hydrolyzed polyvinyl alcohol (PVA, 87-90%), O,O'-bis[2-(N-succinimidyl-succinylamino) ethyl]polyethylene glycol (PEG-diNHS) and dialysis bags (MWCO 12–14 kDa) were purchased from Millipore Sigma. Amplex Red Hydrogen Peroxide/Peroxidase Assay Kit was purchased from ThermoFisher Scientific. Acetate masks were printed at 10 μm resolution by CAD/Art Services. SU-8 3050 and developer were purchased from MicroChem. Silicon wafers (100 mm diameter) were purchased from Silicon Materials. Polydimethylsiloxane (PDMS, Dow Sylgard 184) was purchased from Ellsworth Adhesives. Polytetrafluoroethylene (PTFE) tubing (1/16" outer diameter, 750 μm inner diameter) was purchased from Chromatographic Specialties. Jensen global 20 gauge IT series blunt stainless steel needles were purchased from Howard Electronics. RITC-labelled azide-functionalised, FITC-labelled BCN-functionalised, and unlabelled BSA/PNIPAM-co-MAA nanoconjugate stock solution in MilliQ water (8 mg mL^{-1}) were prepared according to our previously established procedure.[78] These solutions were stored at 4°C.

5.3.1 Fabrication of microfluidic platforms

Microfluidic platforms were designed using AutoCAD (Autodesk Student 2017 LTD) and printed onto acetate masks in order to create positive photomasks. The SU-8 layer was spin-coated onto the wafer at a thickness of 50±2 μm as determined by a DektakXT Stylus Profiler. Next, the wafer was soft baked for 5 min at 25°C, 2 min at 65°C and 30 min at 95°C. Following the soft bake, the wafer was exposed to UV light for 11 s at 19.96 mW cm^{-2} using an OAI Model 800 mask aligner through the acetate photomask. The wafer was then heated at 95°C for 15 min and cooled for 30 min. Unexposed SU-8 was removed using developer and the adhesion of the features was enhanced through exposure to UV light for 90 s at 19.96 mW cm^{-2} and a final hard bake for 30 min at 200°C. The wafer was then placed in a glass desiccator with 50 μL of trimethylchlorosilane and put under vacuum for 1 h to deposit a thin film of silane onto the surface of the wafer. A 10:1 ratio of PDMS base to curing agent was added to a 3D printed wafer holder which was designed to hold the wafer and a set volume of PDMS. The PDMS was degassed for 1 h under vacuum and then cured overnight at 65°C. The cured PDMS was peeled from the mould and individual devices were cut out using a scalpel. The inlets and outlets were created using a 1 mm biopsy punch. The channels were sealed with PDMS-coated glass microscope slides as described below. These slides were made by spin coating PDMS (prepared as described above) onto the slides at 1200 rpm for 25 s. Both the PDMS-coated glass slides and the PDMS devices were washed prior to bonding in soapy reverse osmosis water, reverse osmosis water, isopropyl alcohol, ethanol, Milli-Q water, and then blown dry with filtered air and baked at 95°C for 30 min.

5.3.2 Surface treatment of microfluidic devices

This surface treatment protocol is modified from prior literature.[133] The PVA solution was made by adding PVA to MilliQ water at a final concentration of 0.01 mg mL^{-1}. The solution was stirred at room temperature at 1200 rpm for 45 min, at 100°C at 1200 rpm for 45 min and then at 65°C at 1200 rpm overnight. The solution was used within 24 h. Prior to surface treatment, the PDMS devices and PDMS-coated slides were treated with air plasma (Diener Electronic, Zepto ONE, 1 min, 100 W, 0.64 mbar) in order to activate the surfaces and the slide and device were then placed into contact with each other so as to covalently bond their surfaces. The microfluidic devices were allowed to sit for approximately 2 min. Next, a 25 mL syringe filled with air was fitted with a 20 G syringe tip that had been heat-ligated to 25 cm of PTFE tubing. The syringe was placed into an Aladdin Single-Syringe Infusion Pump (World Precision Instruments) which was set to 800 $\mu Lmin^{-1}$. Next, a 1 mL glass gas-tight syringe (Hamilton) was filled with the PVA solution and connected to tubing as described above. The two innermost inlets on the platform (green and red circles, Figure 5.1a), were plugged with heat-sealed PTFE tubing, the aqueous inlet (brown circle) was connected to a 12 cm length of PTFE tubing to act as an outlet during surface treatment, the middle inlet (yellow circle) was connected to the PTFE tubing connected to the air-filled syringe and the platform outlet (white) was attached to the syringe filled with PVA solution. The pump was turned on and allowed to pump for a minimum of 1 min. After this time, the PVA solution was pushed manually into the platform until the liquid reached the third flow focusing junction, at which point the interface was held steady for 10 min. Then, the inlet attached to the air-filled syringe was removed and attached to a filtered air gun so that the PVA solution could be blown out of the device. The surface treated microfluidic device was then placed on a hot plate for 15 min at 110°C, and then stored at 65°C for a minimum of 72 h

prior to use.

5.3.3 Generation of multicompartmental prototissue spheroids using the microfluidic platform and measurement of their thermally induced reversible contractions

First, a solution of PEG-diNHS crosslinker 160 mg mL^{-1} in Na_2CO_3 buffer (100 mM, pH 8.5) was made. For the inner aqueous phase, 1 mL solutions comprising 500 μL of PEG-diNHS solution and 500 μL of the desired bio-orthogonal protein-polymer nanoconjugate solution were prepared and inserted into the inner inlets of the platform using 1 mL glass gas-tight syringes (Figure 5.1a, green and red circles). The oil phase consisted of 2-ethyl-1 hexanol (Figure 5.1a, yellow circle). The outer phase solution was made by dissolving 250 μL of untagged non-bio-orthogonal BSA/PNIPAM-co-MAA nanoconjugate solution (8 mg $mL^{-}1$) in 25 mL of 1 M Na_2CO_3. A 25 mL glass gas-tight syringe was used to insert the outer aqueous phase into the microfluidic platform. In order to connect all glass syringes to the microfluidic devices, 5 equal lengths (approximately 25 cm) of PTFE tubing were cut and heat ligated to 20 G syringe tips. The syringes were then placed into 4 neMESYS 290N low pressure syringe pumps (Cetoni) and the tips of the tubing were inserted into the respective inlets and outlets. A Phantom VEO710L high-resolution, high-speed camera was used for imaging. The flow rates were set as follows: outer phase = 250 μLmin^{-1}, middle phase = 6 μLmin^{-1}, and both inner phases = 1 μLmin^{-1}. All pumps were started at the same time and were allowed to equilibrate within the platform for approximately 2 min whereby the first multiple emulsions would begin to form. Once this occurred, the outermost flow rate could be tuned to either increase or decrease the encapsulation ratio of the emulsion droplets. After collection, the excess outer phase solution was

removed using a micropipette. Then, 500 μL of a solution of PEG-diNHS crosslinker in water (160 mg mL^{-1}) were added to the prototissue sample in an approximately 1:1 ratio and the mixture was left in the dark at room temperature for 72 h.. After this, the oil was removed *via* dialysis with 70% ethanol in MilliQ water for 3-4 h, followed by 30% ethanol in MilliQ water for 3–4 h, and finally MilliQ water for 18 h. Prototissues were introduced into a chamber created on microscope slide, which was placed onto a temperature stage (LTS420, Likham) on a LSM 880 Zeiss confocal laser scanning microscope. Excitation was provided by either a 488 nm Argon laser (FITC) or 561 nm laser (RITC). For thermoresponsivity experiments, the temperature was varied between 26°C and 47°C and 2 min were allowed for equilibration at each temperature. The changes in the prototissue cross-sectional area were determined using ImageJ (version 1.47t). All data were acquired in triplicate, where each repetition was from a completely new prototissue sample. All images were taken at either 20x or 50x wide-angle magnification.

5.3.4 Bulk generation of azide- and BCN-functionalised proteinosomes as W/O emulsion droplets

In a 1.75 mL vial, 30 μL of an aqueous solution of RITC-labelled azide- or FITC-labelled BCN-functionalised BSA/PNIPAAm-co-MAA nanoconjugates (8 mg mL^{-1}) and 30 μL of a solution PEG-diNHS (67 mg mL^{-1}) in Na_2CO_3 buffer (pH 8.5, 100 mM) were mixed together. Subsequently, 1 mL of 2-ethyl-1-hexanol was gently added to the aqueous phase. The mixture was shaken manually for 30 s to produce a white turbid solution. The changes in the prototissue cross-sectional area were determined using ImageJ (version 1.47t).

5.3.5 Modulation of the endogenous biochemical reactivity of prototissue spheroids

Multicompartmental prototissue spheroids comprised of different ratios of HRP-containing unlabelled azide-functionalised proteinosomes and GOx-containing FITC-labelled BCN-functionalised proteinosomes (5a,5b deca-prototissue spheroids, 1a,9b deca-prototissue spheroids, and 9a,1b deca-prototissue spheroids) were created on the microfluidic platform using the same general procedure described above. In order to enclose the enzyme inside the desired proteinosome type, an aqueous solution of the enzyme was co-dissolved with the appropriate bio-orthogonally reactive protein-polymer nanoconjugate for use as the inner aqueous phase in the microfluidic device. To generate the HRP-containing unlabelled azide-functionalised proteinosomes, 12 μL of a solution of HRP (1000 U mL^{-1}) were added to a 1 mL solution of PEG-diNHS and unlabelled azide-functionalised BSA/PNIPAM-co-MAA nanoconjugate. To generate the GOx-containing FITC-labelled BCN-functionalised proteinosomes, 12 μL of a solution of GOx (1000 U mL^{-1}) were added to the 1 mL solution of PEG-diNHS and FITC-labelled BCN-functionalised BSA/PNIPAM-co-MAA nanoconjugate. After the generation of the desired enzymatically active W/O/W Multicompartmentalal emulsion droplets, the corresponding prototissue spheroids were generated using dialysis following the procedure outlined above. UV-vis spectroscopy (SpectraMax M5) was used for the visualisation of the biochemical reactivity of the prototissue spheroids. To 125 μL of a dispersion of prototissue spheroids were added 37.5 μL of a solution of glucose (300 mM) in MilliQ water and 1.25 μL of a solution of Amplex Red (150 mM) in MilliQ water. The enzyme-mediated generation of the red fluorescent final product resorufin was followed by monitoring the absorbance at 560 nm. Automated path length correction was activated to correct for volume differences between the wells, and a reading was recorded every 30 s. Control experiments were performed

in the same way but either the glucose or Amplex Red solution was substituted with the same volume of MilliQ water.

Chapter 6

Conclusions and Future Work

6.1 Conclusions

The main research question I sought to answer was whether robust microfluidic platforms could be used for the study of bottom-up synthetic cells and tissues in ways that macro-scale methodologies cannot. As an extension of this, I also sought to elucidate new behaviours and applications for these synthetic cells and tissues.

There are three main conclusions from this dissertation. The first is that I was able to engineer reliable microfluidic platforms for the generation of multi-compartmental double emulsions: these platforms took two forms, microcapillary platforms and PDMS devices (Chapters 2 and 3). In Chapter 2, I showed a versatile plug-and-play microcapillary platform for the generation of multicompartmental double emulsions which only required a low cost 3D printer for fabrication and syringe pumps for operation. By doing this work, I have contributed towards making microcapillary devices more accessible to non-experts. In Chapter 3, I focused my efforts on the development of several PDMS platforms for the generation of proteinosomes as synthetic cells. By

doing this, I have shown that PDMS devices (which are useful for synthetic cell fabrication due to their versatility) can be designed to support complex biological double emulsion droplets which is a novel step towards addressing emerging challenges in bottom-up biosynthetic engineering.

The second conclusion was that each of these platforms could be used for specific applications in the study of synthetic cells, both of polymeric and liposomal composition. This aim was highlighted in Chapters 3 and 4. In Chapter 3, I demonstrated the use of my PDMS platform for the generation of proteinosomes. In doing so, I have shown that my microfluidic devices can reliably produce functional synthetic cells which are capable of interlinking. This work was an impactful step forward towards the generation of synthetic tissues. In Chapter 4, I generated liposomes from natural lipids and altered their bilayer composition such that it mimicked the asymmetric nature of red blood cell lipid bilayers. By doing so, I have shown that biomimetic synthetic cells could have great potential in drug development and medicine.

The final conclusion was that I was able to interconnect these polymeric synthetic cells into functional synthetic tissues. This work was shown in Chapter 5, where I explored the use of microfluidic technologies for the programmed assembly of protein-polymer protocells into prototissue spheroids of precise size and composition. In doing so, I have showed that microfluidic technologies enable a new route to the precise and high-throughput fabrication of synthetic tissues with programmable collective properties that can be tuned through a careful assembly of protocell building blocks of different phenotypes. These complex synthetic entities could have a wide range of applications in biotechnology, soft robotics as well as environmentally beneficial bioreactor technologies.

My research has contributed to knowledge on how different microfluidic technologies

can be designed to be used as valuable tools for the generation of multi-compartmental double emulsions to mimic synthetic cells and tissues for multidisciplinary applications.

6.2 Future work

There are several avenues where the work outlined in this dissertation could lead. First, the plug-and-play microcapillary device could be redesigned to generate smaller droplets. The device could easily be altered in one of two ways: first, by flame-tipping the ends of the glass capillaries, and second, by experimenting with different 3D printing resins and techniques in order to generate junction boxes with higher resolution capillary inlet holes. The capacity to make smaller droplets using these plug-and-play platforms is important for the field of droplet microfluidics as it would allow for the generation of droplets which more accurately reflect cell-sizes *in vivo* for use as synthetic cells for applications in drug delivery or as protocellular models. My work with proteinosomes and prototissues also has great potential for diversification. A wider variety of synthetic tissues could be built from different materials which are bespoke to specific applications. For example, the bio-orthogonal and thermoresponsive qualities of our prototissues could be used for the delivery of anti-cancer drugs at localized tumor sites (as the surrounding tumor environment is warmer than physiological temperature). Lastly, regarding my work with asymmetric liposomes, I expect to further develop these liposomes into simple red blood cell (RBC) mimics. The expected biomimeticity of these RBC mimics has the potential to provide earlier insight into the drug development process prior to *in vivo* drug studies. This insight could circumvent some of the high costs associated with the animals models most commonly used in the drugs development process.

Appendix A

Overview

The following appendices contain supplementary information for the previously detailed chapters which did not fit the story line of this dissertation. The appendix begins (Appendix B) with a list of QR codes/ hyperlinks which link the reader to videos which were described in the earlier chapters. All videos are divided by chapter and each contains a description of the experimental conditions. Appendix C details the exploratory work done on a 3D printed microcapillary device prior to the plug-and-play microcapillary device detailed in Chapter 2. Lastly, Appendix D goes into more detail on the troubleshooting process of the surface treatment protocol detailed in Chapter 3.

Appendix B

Video QR Codes

The following QR codes link to the videos described in this dissertation. The videos can be viewed by focusing a smartphone camera onto the code. A YouTube link will appear that connects to the reader to the desired video. The image also doubles as a hyperlink, and the QR code image can be clicked on to link the reader to the video if they are reading a PDF on your computer, tablet or cellular device.

B.1 Chapter 2: A plug-and-play modular microcapillary platform for the generation of multicompartmental double emulsions using glass or fluorocarbon capillaries

To acquire these videos, the microfluidic device was run for approximately 5 minutes. Videos were captured using a digital SLR camera (Canon EOS 6D Mark II) mounted on a stereomicroscope (SMZ800N, Nikon). Videos were cropped and scale bars were

added using Kapwing software.

B.1.1 Tetra-compartmental W/O/W droplets

The video linked to Figure B.1 shows the encapsulation of four inner water droplets (which contain 1 % w/w SDS and 0.25 % w.w blue dye) in FC-40 with PFO droplets on the microfluidic device. An outer flow rate of 2000 ± 100 μLmin^{-1}, a middle flow rate of 200 ± 10 μLmin^{-1}, and an inner flow rate of 20 ± 5 μLmin^{-1} were used to generate tetra-compartmental double emulsions.

Figure B.1: **Formation of water-in-oil-in-water (W/O/W) multicompartmental double emulsions.**

B.1.2 Tetra-compartmental O/W/O droplets

The video linked to Figure B.2 shows the encapsulation of four inner mineral oil droplets in water droplets (which contain 1 % w/w SDS) on the microfluidic device. An outer flow rate of 1000 ± 100 μLmin^{-1}, a middle flow rate of 500 ± 50 μLmin^{-1}, and an inner flow rate of 200 ± 20 μLmin^{-1}, were used to generate tetra-compartmental double emulsions.

Figure B.2: **Formation of oil-in-water-in-oil (O/W/O) multicompartmental double emulsions.**

B.1.3 Tetra-compartmental O/O/W droplets

The video linked to Figure B.3 shows the encapsulation of four Fc40 oil aqueous droplets in light mineral oil droplets on the microfluidic device. An outer flow rate of 300 ± 30 μLmin^{-1}, a middle flow rate of 200 ± 20 μLmin^{-1} and an inner flow rate of 80 ± 10 μLmin^{-1} were used to generate tetra-compartmental double emulsions.

Figure B.3: **Formation of oil-in-oil-in-water (O/O/W) multicompartmental double emulsions.**

B.1.4 Binary 0,4-tetra-compartmental droplets

The video linked to Figure B.4 shows the encapsulation of 2 blue and 2 red water droplets (which contain 1 % w/w SDS and 0.25 % w.w dye) in FC-40 with PFO droplets on the microfluidic device. An outer flow rate of 2000 ± 200 μLmin^{-1}, a middle flow rate of 200 ± 20 μLmin^{-1}, and inner flow rates for each inner phases of 50 ± 10 μLmin^{-1}, were used to generate deca-compartmental double emulsions with equal numbers of each type of inner droplet.

Figure B.4: **Modular microcapillary platform for binary W/O/W multicompartmental double emulsion formation.**

B.2 Chapter 3: Development of a microfluidic platform for the generation of proteinosome synthetic cells

To acquire these videos, the microfluidic device was run for 20-30 minutes. Videos were captured at 100 fps using a Dalsa camera (NanoTech). Channel size (for scale) on chip was 100 μm. Videos are unedited.

B.2.1 Mono-compartmental double emulsion generation

The video linked to Figure B.5 shows the encapsulation of a mono-compartmental double emulsion on the microfluidic device. The outer phase (1% SDS w/w in water) was set to 50 μL min^{-1}, the middle phase (FC40 with 2.5% w/w PicoSurf) was set to 10 μL min^{-1} and the inner phase (water) was set to 1 μL min^{-1}.

Figure B.5: **Mono-compartmental W/O/W double emulsion formation using non-biological materials.**

B.2.2 Bi-compartmental proteinosome generation

The video linked to Figure B.6 shows the encapsulation of a bi-compartmental double emulsion on the microfluidic device. The outer phase (8 mg/mL of BSA/PNIPAM-co-MAA nanoconjugate) was set to 50 μL min^{-1}, the middle phase (2-ethyl-1-hexanol) was set to 10 μL min^{-1} and the inner phase (8 mg/ml of azide-functionalised BSA/PNIPAM-co-MAA nanoconjugate) was set to 2 μL min^{-1}.

Figure B.6: **Bi-compartmental W/O/W double emulsion formation of a singular population of azide-functionalized proteinosomes.**

B.2.3 Tri-compartmental proteinosome generation

The video linked to Figure B.7 shows the encapsulation of a tri-compartmental double emulsion on the microfluidic device. The outer phase (8 mg/mL of BSA/PNIPAM-co-MAA nanoconjugate) was set to 50 μL min^{-1}, the middle phase (2-ethyl-1-hexanol) was set to 10 μL min^{-1} and the inner phase (8 mg/ml of azide-functionalised BSA/PNIPAM-

co-MAA nanoconjugate) was set to 3 μL min^{-1}.

Figure B.7: **Tri-compartmental W/O/W double emulsion formation of a singular population of azide-functionalized proteinosomes.**

B.2.4 Multi-compartmental proteinosome generation

The video linked to Figure B.8 shows the encapsulation of a multi-compartmental double emulsion on the microfluidic device. The outer phase (8 mg/mL of BSA/PNIPAM-co-MAA nanoconjugate) was set to 25 μL min^{-1}, the middle phase (2-ethyl-1-hexanol) was set to 10 μL min^{-1} and the inner phase (8 mg/ml of azide-functionalised BSA/PNIPAM-co-MAA nanoconjugate) was set to 1 μL min^{-1}.

Figure B.8: **Multi-compartmental W/O/W double emulsion formation of a singular population of azide-functionalized proteinosomes.**

B.3 Chapter 4: Bespoke asymmetric liposomes to model passive malarial drug transport across red blood cells

These videos were acquired with the liposomes in a watch glass onthe microscope over 25 minutes. Videos were captured at a frame rate of 7500 fps, with a resolution of 1920x1080. Videos are played at 30 fps. Videos are unedited.

B.3.1 Symmetric liposome formation with lipids in aqueous phase

The video linked to Figure B.9 shows the formation of a mono-compartmental liposome through de-wetting of the middle phase. The inner phase consisted of 8 wt% polyethylene glycol (PEG), 2 wt% poly(vinyl alcohol) (PVA) with 5 mg/ml of DOPC. The middle phase consisted of a mixture of chloroform and hexane (50:50 v/v). The outer phase consisted of 10 wt% PVA, 0.5 wt% Pluronic F-68 and 5 mg/mL of DOPC. Video taken using Phantom High Speed Camera, frame speed 100 fps.

Figure B.9: **Symmetric liposome formation with lipids in aqueous phase.**

B.3.2 Asymmetric liposome formation with lipids in aqueous phase

The video linked to Figure B.10 shows the formation of a mono-compartmental liposome through de-wetting of the middle solvent phase. The inner phase consisted of 8 wt% polyethylene glycol (PEG), 2 wt% poly(vinyl alcohol) (PVA) with 5 mg/ml of PE. The middle phase consisted of a mixture of chloroform and hexane (50:50 v/v). The outer phase consisted of 10 wt% PVA, 0.5 wt% Pluronic F-68 and 5 mg/mL of PC. Video taken using Phantom High Speed Camera, frame speed 100 fps.

Figure B.10: **Asymmetric liposome formation with lipids in aqueous phase.**

B.4 Chapter 5: Programmed assembly of bespoke prototissue spheroids on a microfluidic platform

To acquire the videos, the microfluidic device was run for 25 minutes. Videos were captured at a frame rate of 7500 fps, with a resolution of 1920x1080. Videos are played at 30 fps. All videos were edited and error bars were included using Kapwing editing software. For all videos, the outer phase consisted of 8 mg/mL of BSA/PNIPAM-co-MAA nanoconjugate, the middle phase consisted of 2-ethyl-1-hexaol and the two inner phases consisted of 8 mg/mL of either azide-functionalised BSA/PNIPAM-co-MAA

nanoconjugate or BCN-functionalised BSA/PNIPAM-co-MAA nanoconjugate.

B.4.1 Overview of prototissue synthesis

The video linked to Figure B.11 shows how the microfluidic device, pumps, Nikon Ti microscope and prototissue collection are put together. The video was captured using a smartphone.

Figure B.11: **Overview of microfluidic prototissue synthesis.**

B.4.2 Mono-compartmental W/O/W droplets

The video linked to Figure B.12 shows the encapsulation of a single protocell on the microfluidic device. The outer phase was set to 350 μL min^{-1}, the middle phase was set to 6 μL min^{-1} and both inner phases were set to 1 μL min^{-1}.

Figure B.12: **Mono-compartmental W/O/W double emulsions formation.**

B.4.3 1a,1b bi-compartmental W/O/W droplets

The video linked to Figure B.13 shows the encapsulation of 2 protocells on the microfluidic device. The outer phase was set to 330 μL min^{-1}, the middle phase was set to 6 μL min^{-1} and both inner phases were set to 1 μL min^{-1}.

Figure B.13: **Bi-compartmental W/O/W double emulsions.**

B.4.4 2a,2b tetra-compartmental W/O/W droplets

The video linked to Figure B.14 shows the encapsulation of 4 protocells on the microfluidic device. The outer phase was set to 310 μL min^{-1}, the middle phase was set to 6 μL min^{-1} and both inner phases were set to 1 μL min^{-1}.

Figure B.14: **Tetra-compartmental W/O/W double emulsions formation.**

B.4.5 3a,3b hexa-compartmental W/O/W droplets

The video linked to Figure B.15 shows the encapsulation of 6 protocells on the microfluidic device. The outer phase was set to 290 μL min^{-1}, the middle phase was set

to 6 μL min^{-1} and both inner phases were set to 1 μL min^{-1}.

Figure B.15: **Hexa-compartmental W/O/W double emulsions formation.**

B.4.6 4a,4b octa-compartmental W/O/W droplets

The video linked to Figure B.16 shows the encapsulation of 8 protocells on the microfluidic device. The outer phase was set to 260 μL min^{-1}, the middle phase was set to 6 μL min^{-1} and both inner phases were set to 1 μL min^{-1}.

Figure B.16: **Octa-compartmental W/O/W double emulsions formation.**

B.4.7 5a,5b deca-compartmental W/O/W droplets

The video linked to Figure B.17 shows the encapsulation of 10 protocells on the microfluidic device. The outer phase was set to 240 μL min^{-1}, the middle phase was set to 6 μL min^{-1} and both inner phases were set to 1 μL min^{-1}.

Figure B.17: **Deca-compartmental W/O/W double emulsions formation.**

B.4.8 Overview of working microfluidic device

The video linked to Figure B.18 shows the video for the a zoomed-out overview of the working microfluidic device. On the left-hand side of the field of view it is possible to see the first two parallel flow focusing junctions forming the bio-orthogonally reactive proteinosomes. The outer phase was set to 350 μL min^{-1}, the middle phase was set to 6 μL min^{-1} and both inner phases were set to 1 μL min^{-1}.

Figure B.18: **Overview of proteinosome and W/O/W double emulsion formation on the microfluidic device.**

B.4.9 Reorganisation of proteinosomes within multi-compartmental W/O/W droplets

The video linked to Figure B.19 shows the video for the free movement of bio-orthogonally reactive proteinosomes within multi-compartmental w/o/w emulsion droplets can be visualized. In this experiment, the outer phase was set to 200 μL

min^{-1}, the middle phase was set to 6 μL min^{-1} and both inner phases were set to 1 μL min^{-1}. Proteinosomes enclosed within the droplet's outer membrane move according to well-known flow re-circulation effects. Remarkably, due to the symmetry of the inner droplet flux they do not mix, hence maintaining the predetermined Janus-like organisation. The same effect was observed for every type of multi-compartmental w/o/w emulsion droplets generated with our microfluidic device.

Figure B.19: **Circular proteinosome movement within larger W/O/W double emulsions.**

B.4.10 Thermally induced contraction on a 2a,12b tetradeca-prototissue spheroid

The video linked to Figure B.20 shows the video for the temperature was varied from 26°C to 47°C with a rate of 5°C/min using a Linkham temperature stand. Time-dependent images were captured using confocal microscopy as described in the experimental section.

Figure B.20: **Thermally induced contraction of 2a,12b tetradeca-prototissue spheroid.**

Appendix C

Initial microcapillary device development

The following section details my attempted reproduction of the work by Martino *et al.*.[124] This 3D printed microcapillary device used glass microcapillaries in the place of PDMS channels. The 3D printed element serves as a holder for these tubes. As seen in Figure C.1, the 3D printed device was composed of five parts: two screws, two screw holders and a baseplate. The device required a high-resolution printer that is capable of printing wax filler as a support structure for the smaller device features. The authors printed this design on a ProJet 3510 HD, using an Acrylonitrile Butadiene Styrene (ABS) resin, which is not available at UVic. As a result, the printing job was outsourced to Camosun College. Unfortunately, as a result of the lower resolution of the 3D printing technology as well as some inherent design flaws (such as the lack of an O-ring sealant) the 3D printed device irreparably leaked (as shown in Figure C.1). Unlike the work outlined in Chapter 2, the Martino *et al.* device used the 3D printed elements to hold the capillaries. The leaking was mostly concentrated in the spool

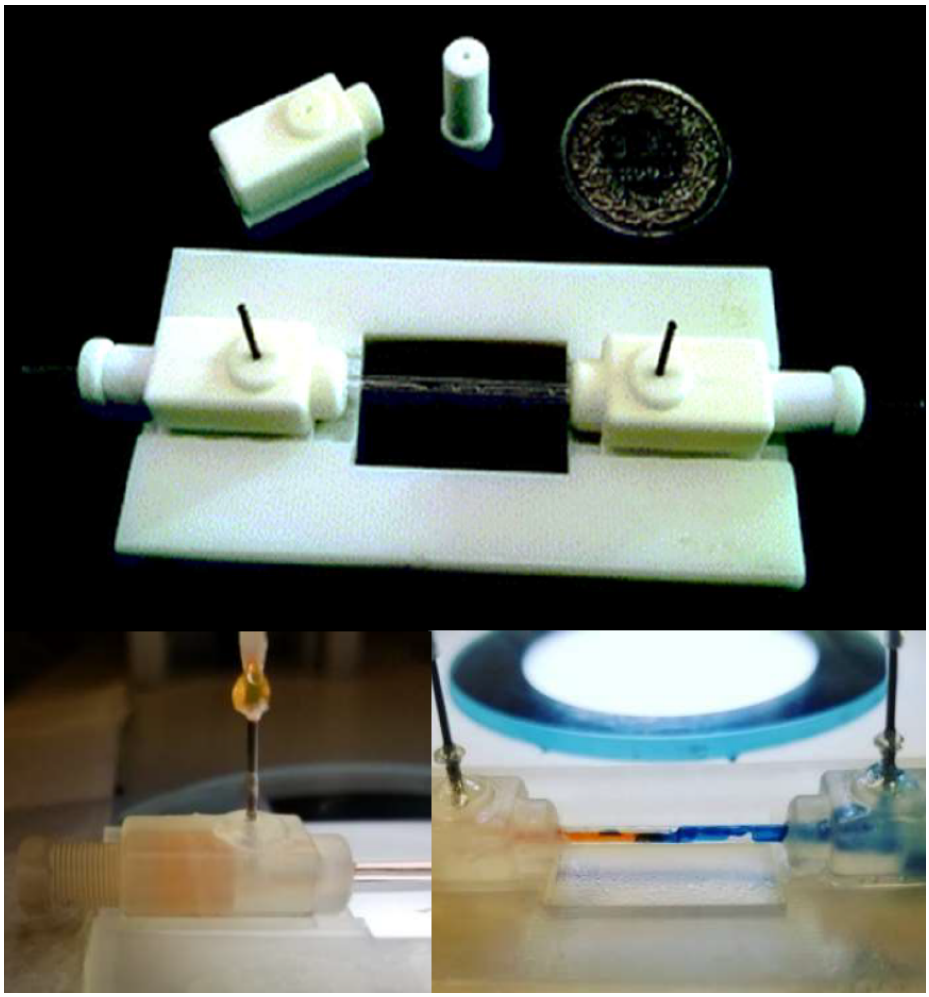

Figure C.1: **3D printed microcapillary device**. The top image depicts the relative size of the entire device and is taken from the original paper. The bottom two images were taken by me to show the irreparable leaking and uncontrollable flow that ensued. Top image reproduced from Martino *et al.* with permission.[124]

region and could not be easily corrected using glue while still being reusable. It was concluded that multiple emulsions could not be easily produced using this platform. That said, this time was not wasted as it birthed the idea of the new, more dynamic, functional and cheaper 3D printed microcapillary device shown in Chapter 2.

Appendix D

Surface treatment troubleshooting

The section below details (in chronological order) the troubleshooting of my surface treatment protocol for the generation of proteinosomes and prototissues from multi-compartmental double emulsions on a microfluidic device.

D.0.1 Approach 1: laundry bag PVA and hydrophobic surface treatment

My surface treatment protocol started with the use of "laundry bag" PVA, a water soluble film which is often used to wash soiled hospital clothing. We had this PVA on hand from a previous group, so it was used for preliminary trials out of convenience. This surface treatment approach also used a silane for hydrophobic surface treatment, trichloro(1H,1H,2H,2H-perfluorooctyl)silane (PFO, Sigma-Aldrich) in isopropanol which had been dried over molecular sieves. At the time, we assumed that though PDMS is naturally hydrophobic, it would not be enough for the initial droplet generation in which aqueous droplets are formed in an oil solution (W/O). The surface treatment protocol proceeded as described in Chapter 2, with several notable

differences. The first is that PFO was pushed through the outlet in the place of air. The second is that the PVA solution was prepared differently: 1 g of the laundry bag PVA was dissolved in water and stirred. It was immediately ready for use. Lastly, the PVA was also pumped through the device using an Aladdin syringe pump. The flow rate of the PFO was 100 μLmin^{-1} and of the PVA solution was 3 μLmin^{-1}.

We initially implemented the hydrophobic surface treatment of PDMS as there was a precedence in the literature.[131] That said, I observed that hydrophobic surface treatment often resulted in damaging crystallization in our smaller microfluidic channels. These crystals interfered with droplet formation. We decided that leaving our PDMS devices in the oven overnight after plasma bonding would be sufficient. I filled the syringes with air instead of IPA with PFO, and used the air to keep the hydrophillic PVA surface treatment from the channels I desired to keep hydrophobic. As I moved onto work with BSA however, I found that my microfluidic devices had to be left in the oven for approximately 72 h before BSA nanoconjugate droplets could be formed with any reliability. Where the double emulsions were formed (the encapsulation of the aqueous droplets in an oil droplet) I found that the oil droplets would stick and merge. This led me to believe that the laundry bag PVA would not result in a sufficiently hydrophillic surface.

D.0.2 Approach 2: new PVA protocol

Eventually, a point was reached in my project where there was not enough reliability in double emulsion generation between devices. Double emulsion droplets of consistent composition and size were not being produced. As a result, I started using 87-90% PVA (Sigma Aldrich). The reasoning behind this particular brand of PVA is due, in part, on the work done by Bauer *et al.*[132] and Transtidou *et al*[133] who both

conducted exhaustive studies on the benefits of differently hydrolyzed PVA types. I hence developed on my own protocol based on the literature. PVA solution had to be prepared fresh, the day prior to use and had to sit, mixing, on a hotplate overnight. Moreover, I decided to dose the PVA solution manually, rather than with a syringe pump. Manual dosage allowed real-time adjustments between different devices. The downside of manual dosage was that it took significant practice (and a steady hand) to get good at surface treatment. I also repeated the PVA surface treatment three times after plasma bonding, in order to ensure maximal coating. Though the protocol is exhaustive, I was able to generate multicompartmental double emulsions with high precision and accuracy.

References

1. Whitesides, G. M. The origins and the future of microfluidics. *Nature* **442,** 368–373. ISSN: 1476-4687. https://www.nature.com/articles/nature05058 (2021) (July 2006).
2. Elvira, K. S., i Solvas, X. C., Wootton, R. C. R. & deMello, A. J. The past, present and potential for microfluidic reactor technology in chemical synthesis. *Nature Chemistry* **5,** 905–915. ISSN: 1755-4349. https://www.nature.com/articles/nchem.1753 (2021) (Nov. 2013).
3. Sohrabi, S., Kassir, N. & Moraveji, M. K. Droplet microfluidics: fundamentals and its advanced applications. *RSC Advances* **10,** 27560–27574. ISSN: 2046-2069. https://pubs.rsc.org/en/content/articlelanding/2020/ra/d0ra04566g (2021) (July 21, 2020).
4. Teh, S.-Y., Lin, R., Hung, L.-H. & Lee, A. P. Droplet microfluidics. *Lab on a Chip* **8,** 198–220. ISSN: 1473-0189. https://pubs.rsc.org/en/content/articlelanding/2008/lc/b715524g (2020) (Jan. 29, 2008).
5. Zhu, P. & Wang, L. Passive and active droplet generation with microfluidics: a review. *Lab on a Chip* **17,** 34–75. ISSN: 1473-0189. https://pubs.rsc.org/en/content/articlelanding/2017/lc/c6lc01018k (2021) (Dec. 20, 2016).
6. Gu, S., Mogi, T. & Konno, M. Preparation of Monodisperse, Micron-Sized Polystyrene Particles with Single-Stage Polymerization in Aqueous Media. *Jour-*

nal of Colloid and Interface Science **207,** 113–118. ISSN: 0021-9797. https://www.sciencedirect.com/science/article/pii/S002197979895768X (2021) (Nov. 1, 1998).

7. Murakami, R., Moriyama, H., Noguchi, T., Yamamoto, M. & Binks, B. P. Effects of the Density Difference between Water and Oil on Stabilization of Powdered Oil-in-Water Emulsions. *Langmuir* **30,** 496–500. ISSN: 0743-7463. https://doi.org/10.1021/la4042056 (2021) (Jan. 21, 2014).
8. Wang, W., Zhang, M.-J. & Chu, L.-Y. Microfluidic approach for encapsulation via double emulsions. *Current Opinion in Pharmacology. Anti-infectives • New technologies* **18,** 35–41. ISSN: 1471-4892. https://www.sciencedirect.com/science/article/pii/S1471489214000952 (2021) (Oct. 1, 2014).
9. Deng, N.-N., Yelleswarapu, M. & Huck, W. T. S. Monodisperse Uni- and Multicompartment Liposomes. *Journal of the American Chemical Society* **138,** 7584–7591. ISSN: 0002-7863. https://doi.org/10.1021/jacs.6b02107 (2021) (June 22, 2016).
10. Butler, K. S. *et al.* Protocells: Modular Mesoporous Silica Nanoparticle-Supported Lipid Bilayers for Drug Delivery. *Small* **12,** 2173–2185. ISSN: 1613-6829. https://onlinelibrary.wiley.com/doi/abs/10.1002/smll.201502119 (2020) (2016).
11. Muschiolik, G. Multiple emulsions for food use. *Current Opinion in Colloid & Interface Science* **12,** 213–220. ISSN: 1359-0294. https://www.sciencedirect.com/science/article/pii/S1359029407000672 (2021) (Oct. 1, 2007).
12. *Multiple Emulsion - an overview — ScienceDirect Topics* https://www.sciencedirect.com/topics/chemistry/multiple-emulsion (2021).
13. Zhao, C.-X. Multiphase flow microfluidics for the production of single or multiple emulsions for drug delivery. *Advanced Drug Delivery Reviews. Design pro-*

duction and characterization of drug delivery systems by Lab-on-a-Chip technology **65,** 1420–1446. ISSN: 0169-409X. https://www.sciencedirect.com/science/article/pii/S0169409X13001476 (2021) (Nov. 15, 2013).

14. Liau, J. J., Hook, S., Prestidge, C. A. & Barnes, T. J. A lipid based multicompartmental system: Liposomes-in-double emulsion for oral vaccine delivery. *European Journal of Pharmaceutics and Biopharmaceutics* **97,** 15–21. ISSN: 0939-6411. https://www.sciencedirect.com/science/article/pii/S0939641115003987 (2021) (Nov. 1, 2015).

15. Adams, L. L. A. *et al.* Single step emulsification for the generation of multicomponent double emulsions. *Soft Matter* **8,** 10719–10724. ISSN: 1744-6848. https://pubs.rsc.org/en/content/articlelanding/2012/sm/c2sm25953b (2021) (Oct. 3, 2012).

16. Shum, H. C., Zhao, Y.-j., Kim, S.-H. & Weitz, D. A. Multicompartment Polymersomes from Double Emulsions. *Angewandte Chemie International Edition* **50,** 1648–1651. ISSN: 1521-3773. https://onlinelibrary.wiley.com/doi/abs/10.1002/anie.201006023 (2021) (2011).

17. Martino, C. & deMello, A. J. Droplet-based microfluidics for artificial cell generation: a brief review. *Interface Focus* **6.** ISSN: 2042-8898. https://www.ncbi.nlm.nih.gov/pmc/articles/PMC4918832/ (2021) (Aug. 6, 2016).

18. Zhang, W., Zhai, X., Ou, W., Song, L. & Zhang, Q. Influencing factors of multiple emulsions formed by one-step emulsification. *Colloid and Polymer Science* **296,** 259–269. ISSN: 1435-1536. https://doi.org/10.1007/s00396-017-4232-4 (2021) (Feb. 1, 2018).

19. Chang, T. M. S. Semipermeable Microcapsules. *Science* **146,** 524–525. ISSN: 0036-8075, 1095-9203. https://science.sciencemag.org/content/146/3643/524 (2021) (Oct. 23, 1964).

20. Swi Chang, T. M. 50th Anniversary of Artificial Cells: Their Role in Biotechnology, Nanomedicine, Regenerative Medicine, Blood Substitutes, Bioencapsulation, Cell/Stem Cell Therapy and Nanorobotics. *Artificial Cells, Blood Substitutes, and Biotechnology* **35,** 545–554. ISSN: 1073-1199, 1532-4184. http://www.tandfonline.com/doi/full/10.1080/10731190701730172 (2021) (Jan. 2007).

21. Liu, J., Stace-Naughton, A., Jiang, X. & Brinker, C. J. Porous Nanoparticle Supported Lipid Bilayers (Protocells) as Delivery Vehicles. *Journal of the American Chemical Society* **131,** 1354–1355. ISSN: 0002-7863. https://doi.org/10.1021/ja808018y (2020) (Feb. 4, 2009).

22. Durfee, P. N. *et al.* Mesoporous Silica Nanoparticle-Supported Lipid Bilayers (Protocells) for Active Targeting and Delivery to Individual Leukemia Cells. *ACS Nano* **10,** 8325–8345. ISSN: 1936-0851. https://doi.org/10.1021/acsnano.6b02819 (2020) (Sept. 27, 2016).

23. Mesoporous silica-supported lipid bilayers (protocells) for DNA cargo delivery to the spinal cord. *Journal of Controlled Release* **168,** 209–224. ISSN: 0168-3659. https://www.sciencedirect.com/science/article/pii/S0168365913001521 (2020) (June 10, 2013).

24. Yin, Y. *et al.* Electric field-induced circulation and vacuolization regulate enzyme reactions in coacervate-based protocells. *Soft Matter* **14,** 6514–6520. ISSN: 1744-6848. https://pubs.rsc.org/en/content/articlelanding/2018/sm/c8sm01168k (2020) (Aug. 8, 2018).

25. Kumar, B. V. V. S. P., Patil, A. J. & Mann, S. Enzyme-powered motility in buoyant organoclay/DNA protocells. *Nature Chemistry* **10,** 1154–1163. ISSN: 1755-4349. https://www.nature.com/articles/s41557-018-0119-3 (2020) (Nov. 2018).

26. Fox, S. W. *et al.* Experimental retracement of the origins of a protocell. *Journal of Biological Physics* **20,** 17–36. ISSN: 1573-0689. https://doi.org/10.1007/BF00700418 (2020) (Mar. 1, 1995).

27. Luisi, P. L. *et al.* Spontaneous protein crowding in liposomes: a new vista for the origin of cellular metabolism. *Chembiochem: A European Journal of Chemical Biology* **11,** 1989–1992. ISSN: 1439-7633 (Sept. 24, 2010).

28. Gobbo, P. From protocells to prototissues: a materials chemistry approach. *Biochemical Society Transactions* **48,** 2579–2589. ISSN: 0300-5127. https://doi.org/10.1042/BST20200310 (2021) (Nov. 6, 2020).

29. Chang, T. M. S. Therapeutic applications of polymeric artificial cells. *Nature Reviews Drug Discovery* **4,** 221–235. ISSN: 1474-1784. https://www.nature.com/articles/nrd1659 (2021) (Mar. 2005).

30. Huang, X. *et al.* Interfacial assembly of protein–polymer nano-conjugates into stimulus-responsive biomimetic protocells. *Nature Communications* **4,** 2239. ISSN: 2041-1723. https://www.nature.com/articles/ncomms3239 (2020) (July 30, 2013).

31. Yadavalli, S. S. *et al.* Bioactive cell-like hybrids from dendrimersomes with a human cell membrane and its components. *Proceedings of the National Academy of Sciences* **116,** 744–752. ISSN: 0027-8424, 1091-6490. https://www.pnas.org/content/116/3/744 (2021) (Jan. 15, 2019).

32. Zhuang, M. *et al.* Uricase-containing coacervate microdroplets as enzyme active membrane-free protocells for detoxification of uric acid in serum. *Chemical Communications* **55,** 13880–13883. ISSN: 1364-548X. https://pubs.rsc.org/en/content/articlelanding/2019/cc/c9cc07037k (2021) (Nov. 14, 2019).

33. Williams, D. S., Patil, A. J. & Mann, S. Spontaneous Structuration in Coacervate-Based Protocells by Polyoxometalate-Mediated Membrane Assembly. *Small*

10, 1830–1840. ISSN: 1613-6829. https://onlinelibrary.wiley.com/doi/abs/10.1002/smll.201303654 (2020) (2014).

34. Gobbo, P., Novoa, S., Biesinger, M. C. & Workentin, M. S. Interfacial strain-promoted alkyne–azide cycloaddition (I-SPAAC) for the synthesis of nanomaterial hybrids. *Chemical Communications* **49,** 3982–3984. ISSN: 1364-548X. https://pubs.rsc.org/en/content/articlelanding/2013/cc/c3cc41634h (2020) (Apr. 16, 2013).

35. Kim, B., Jeon, T. Y., Oh, Y.-K. & Kim, S.-H. Microfluidic Production of Semipermeable Microcapsules by Polymerization-Induced Phase Separation. *Langmuir* **31,** 6027–6034. ISSN: 0743-7463. https://doi.org/10.1021/acs.langmuir.5b01129 (2021) (June 9, 2015).

36. Li, M., Harbron, R. L., Weaver, J. V. M., Binks, B. P. & Mann, S. Electrostatically gated membrane permeability in inorganic protocells. *Nature Chemistry* **5,** 529–536. ISSN: 1755-4349. https://www.nature.com/articles/nchem.1644 (2020) (June 2013).

37. Li, M., Huang, X. & Mann, S. Spontaneous growth and division in self-reproducing inorganic colloidosomes. *Small (Weinheim an Der Bergstrasse, Germany)* **10,** 3291–3298. ISSN: 1613-6829 (Aug. 27, 2014).

38. Li, M., C. Green, D., Ross Anderson, J. L., P. Binks, B. & Mann, S. In vitro gene expression and enzyme catalysis in bio-inorganic protocells. *Chemical Science* **2,** 1739–1745. https://pubs.rsc.org/en/content/articlelanding/2011/sc/c1sc00183c (2020) (2011).

39. Martino, C. *et al.* Protein Expression, Aggregation, and Triggered Release from Polymersomes as Artificial Cell-like Structures. *Angewandte Chemie International Edition* **51,** 6416–6420. ISSN: 14337851. http://doi.wiley.com/10.1002/anie.201201443 (2021) (June 25, 2012).

40. Thiele, J. *et al.* Fabrication of Polymersomes using Double-Emulsion Templates in Glass-Coated Stamped Microfluidic Devices. *Small* **6,** 1723–1727. ISSN: 1613-6829. https://onlinelibrary.wiley.com/doi/abs/10.1002/smll.201000798 (2021) (2010).

41. Ugrinic, M. *et al.* Microfluidic formation of proteinosomes. *Chemical Communications* **54,** 287–290. ISSN: 1364-548X. https://pubs.rsc.org/en/content/articlelanding/2018/cc/c7cc08466h (2021) (Jan. 2, 2018).

42. in. *Wikipedia* Page Version ID: 1008254697 (Feb. 22, 2021). https://en.wikipedia.org/w/index.php?title=Lipid_bilayer&oldid=1008254697 (2021).

43. Akbarzadeh, A. *et al.* Liposome: classification, preparation, and applications. *Nanoscale Research Letters* **8,** 102. ISSN: 1931-7573. https://www.ncbi.nlm.nih.gov/pmc/articles/PMC3599573/ (2021) (Feb. 22, 2013).

44. Bretscher, M. S. Asymmetrical Lipid Bilayer Structure for Biological Membranes. *Nature New Biology* **236,** 11–12. ISSN: 2058-1092. https://www.nature.com/articles/newbio236011a0 (2021) (Mar. 1972).

45. Bangham, A. D. & Horne, R. W. Action of Saponin on Biological Cell Membranes. *Nature* **196,** 952–953. ISSN: 1476-4687. https://www.nature.com/articles/196952a0 (2021) (Dec. 1962).

46. Kamiya, K. & Takeuchi, S. Giant liposome formation toward the synthesis of well-defined artificial cells. *Journal of Materials Chemistry B* **5,** 5911–5923. ISSN: 2050-7518. https://pubs.rsc.org/en/content/articlelanding/2017/tb/c7tb01322a (2021) (Aug. 2, 2017).

47. Sato, Y. & Takinoue, M. Creation of Artificial Cell-Like Structures Promoted by Microfluidics Technologies. *Micromachines* **10,** 216. https://www.mdpi.com/2072-666X/10/4/216 (2021) (Apr. 2019).

48. Rideau, E., Dimova, R., Schwille, P., R. Wurm, F. & Landfester, K. Liposomes and polymersomes: a comparative review towards cell mimicking. *Chemical Society Reviews* **47,** 8572–8610. https://pubs.rsc.org/en/content/articlelanding/2018/cs/c8cs00162f (2021) (2018).

49. Montes, L.-R., Alonso, A., Goñi, F. M. & Bagatolli, L. A. Giant Unilamellar Vesicles Electroformed from Native Membranes and Organic Lipid Mixtures under Physiological Conditions. *Biophysical Journal* **93,** 3548–3554. ISSN: 00063495. https://linkinghub.elsevier.com/retrieve/pii/S0006349507716065 (2021) (Nov. 2007).

50. Rossier, O. *et al.* Giant Vesicles under Flows: Extrusion and Retraction of Tubes. *Langmuir* **19,** 575–584. ISSN: 0743-7463, 1520-5827. https://pubs.acs.org/doi/10.1021/la026236t (2021) (Feb. 2003).

51. Szoka, F. & Papahadjopoulos, D. Procedure for preparation of liposomes with large internal aqueous space and high capture by reverse-phase evaporation. *Proceedings of the National Academy of Sciences* **75,** 4194–4198. ISSN: 0027-8424, 1091-6490. http://www.pnas.org/cgi/doi/10.1073/pnas.75.9.4194 (2021) (Sept. 1, 1978).

52. Li, S. & Palmer, A. F. Structure of Small Actin-Containing Liposomes Probed by Atomic Force Microscopy: Effect of Actin Concentration & Liposome Size. *Langmuir* **20,** 7917–7925. ISSN: 0743-7463, 1520-5827. https://pubs.acs.org/doi/10.1021/la049035t (2021) (Sept. 2004).

53. Pautot, S., Frisken, B. J. & Weitz, D. A. Engineering asymmetric vesicles. *Proceedings of the National Academy of Sciences* **100,** 10718–10721. ISSN: 0027-8424, 1091-6490. http://www.pnas.org/cgi/doi/10.1073/pnas.1931005100 (2021) (Sept. 16, 2003).

54. Hishida, M., Seto, H., Yamada, N. & Yoshikawa, K. Hydration process of multi-stacked phospholipid bilayers to form giant vesicles. *Chemical Physics Letters* **455,** 297–302. ISSN: 00092614. https://linkinghub.elsevier.com/retrieve/pii/S0009261408002704 (2021) (Apr. 2008).

55. Van Swaay, D. & deMello, A. Microfluidic methods for forming liposomes. *Lab on a Chip* **13,** 752. ISSN: 1473-0197, 1473-0189. http://xlink.rsc.org/?DOI=c2lc41121k (2021) (2013).

56. Crane, J. M., Kiessling, V. & Tamm, L. K. Measuring lipid asymmetry in planar supported bilayers by fluorescence interference contrast microscopy. *Langmuir: the ACS journal of surfaces and colloids* **21,** 1377–1388. ISSN: 0743-7463 (Feb. 15, 2005).

57. Kalb, E., Frey, S. & Tamm, L. K. Formation of supported planar bilayers by fusion of vesicles to supported phospholipid monolayers. *Biochimica et Biophysica Acta (BBA) - Biomembranes* **1103,** 307–316. ISSN: 0005-2736. https://www.sciencedirect.com/science/article/pii/000527369290101Q (2021) (Jan. 31, 1992).

58. Hu, P. C., Li, S. & Malmstadt, N. Microfluidic Fabrication of Asymmetric Giant Lipid Vesicles. *ACS Applied Materials & Interfaces* **3,** 1434–1440. ISSN: 1944-8244. https://doi.org/10.1021/am101191d (2021) (May 25, 2011).

59. Matosevic, S. & Paegel, B. M. Stepwise Synthesis of Giant Unilamellar Vesicles on a Microfluidic Assembly Line. *Journal of the American Chemical Society* **133,** 2798–2800. ISSN: 0002-7863, 1520-5126. https://pubs.acs.org/doi/10.1021/ja109137s (2021) (Mar. 9, 2011).

60. Tan, Y.-C., Hettiarachchi, K., Siu, M., Pan, Y.-R. & Lee, A. P. Controlled Microfluidic Encapsulation of Cells, Proteins, and Microbeads in Lipid Vesicles. *Journal of the American Chemical Society* **128,** 5656–5658. ISSN: 0002-7863,

1520-5126. https://pubs.acs.org/doi/10.1021/ja056641h (2021) (May 2006).

61. Abkarian, M., Loiseau, E. & Massiera, G. Continuous droplet interface crossing encapsulation (cDICE) for high throughput monodisperse vesicle design. *Soft Matter* **7,** 4610. ISSN: 1744-683X, 1744-6848. http://xlink.rsc.org/?DOI=c1sm05239j (2021) (2011).

62. Deshpande, S., Caspi, Y., Meijering, A. E. C. & Dekker, C. Octanol-assisted liposome assembly on chip. *Nature Communications* **7,** 10447. ISSN: 2041-1723. http://www.nature.com/articles/ncomms10447 (2021) (Apr. 22, 2016).

63. Shum, H. C., Lee, D., Yoon, I., Kodger, T. & Weitz, D. A. Double Emulsion Templated Monodisperse Phospholipid Vesicles. *Langmuir* **24,** 7651–7653. ISSN: 0743-7463, 1520-5827. https://pubs.acs.org/doi/10.1021/la801833a (2021) (Aug. 2008).

64. Arriaga, L. R. *et al.* Ultrathin Shell Double Emulsion Templated Giant Unilamellar Lipid Vesicles with Controlled Microdomain Formation. *Small* **10,** 950–956. ISSN: 16136810. http://doi.wiley.com/10.1002/smll.201301904 (2021) (Mar. 2014).

65. Funakoshi, K., Suzuki, H. & Takeuchi, S. Formation of Giant Lipid Vesiclelike Compartments from a Planar Lipid Membrane by a Pulsed Jet Flow. *Journal of the American Chemical Society* **129,** 12608–12609. ISSN: 0002-7863, 1520-5126. https://pubs.acs.org/doi/10.1021/ja074029f (2021) (Oct. 2007).

66. Stachowiak, J. C. *et al.* Unilamellar vesicle formation and encapsulation by microfluidic jetting. *Proceedings of the National Academy of Sciences* **105,** 4697–4702. ISSN: 0027-8424, 1091-6490. http://www.pnas.org/cgi/doi/10.1073/pnas.0710875105 (2021) (Mar. 25, 2008).

67. Ota, S., Yoshizawa, S. & Takeuchi, S. Microfluidic Formation of Monodisperse, Cell-Sized, and Unilamellar Vesicles. *Angewandte Chemie International Edition* **48,** 6533–6537. ISSN: 14337851, 15213773. http://doi.wiley.com/10.1002/anie.200902182 (2021) (Aug. 17, 2009).

68. Boyd, M. A. & Kamat, N. P. Designing Artificial Cells towards a New Generation of Biosensors. *Trends in Biotechnology* **0.** ISSN: 0167-7799, 1879-3096. https://www.cell.com/trends/biotechnology/abstract/S0167-7799(20)30326-7 (2021) (Dec. 30, 2020).

69. Damiano, L. & Stano, P. On the "Life-Likeness" of Synthetic Cells. *Frontiers in Bioengineering and Biotechnology* **8.** ISSN: 2296-4185. https://www.frontiersin.org/articles/10.3389/fbioe.2020.00953/full (2021) (2020).

70. Artificial cells: from basic science to applications. *Materials Today* **19,** 516–532. ISSN: 1369-7021. https://www.sciencedirect.com/science/article/pii/S1369702116000699 (2021) (Nov. 1, 2016).

71. Buddingh', B. C. & van Hest, J. C. M. Artificial Cells: Synthetic Compartments with Life-like Functionality and Adaptivity. *Accounts of Chemical Research* **50,** 769–777. ISSN: 0001-4842. https://doi.org/10.1021/acs.accounts.6b00512 (2021) (Apr. 18, 2017).

72. Jeong, S., Nguyen, H. T., Kim, C. H., Ly, M. N. & Shin, K. Toward Artificial Cells: Novel Advances in Energy Conversion and Cellular Motility. *Advanced Functional Materials* **30,** 1907182. ISSN: 1616-3028. https://onlinelibrary.wiley.com/doi/abs/10.1002/adfm.201907182 (2021) (2020).

73. Bayley, H., Cazimoglu, I. & Hoskin, C. E. Synthetic tissues. *Emerging Topics in Life Sciences* **3,** 615–622. ISSN: 2397-8554. https://doi.org/10.1042/ETLS20190120 (2020) (Oct. 18, 2019).

74. Building synthetic multicellular systems using bottom–up approaches. *Current Opinion in Systems Biology* **24,** 56–63. ISSN: 2452-3100. https://www.sciencedirect.com/science/article/pii/S2452310020300470 (2021) (Dec. 1, 2020).

75. OpenStax. in *Anatomy and Physiology* (OpenStax, Mar. 6, 2013). https://opentextbc.ca/anatomyandphysiology/chapter/4-1-types-of-tissues/ (2020).

76. Toda, S., Blauch, L. R., Tang, S. K. Y., Morsut, L. & Lim, W. A. Programming self-organizing multicellular structures with synthetic cell-cell signaling. *Science* **361,** 156–162. ISSN: 0036-8075, 1095-9203. https://science.sciencemag.org/content/361/6398/156 (2021) (July 13, 2018).

77. Langer, R. & Vacanti, J. P. Tissue engineering. *Science* **260,** 920–926. ISSN: 0036-8075, 1095-9203. https://science.sciencemag.org/content/260/5110/920 (2021) (May 14, 1993).

78. Gobbo, P. *et al.* Programmed assembly of synthetic protocells into thermoresponsive prototissues. *Nature Materials* **17,** 1145–1153. ISSN: 1476-4660. https://www.nature.com/articles/s41563-018-0183-5 (2021) (Dec. 2018).

79. Zhu, S. *et al.* Rapid Multilevel Compartmentalization of Stable All-Aqueous Blastosomes by Interfacial Aqueous-Phase Separation. *ACS Nano* **14,** 11215–11224. ISSN: 1936-0851, 1936-086X. https://pubs.acs.org/doi/10.1021/acsnano.0c02923 (2021) (Sept. 22, 2020).

80. Karlsson, M. *et al.* Formation of geometrically complex lipid nanotube-vesicle networks of higher-order topologies. *Proceedings of the National Academy of Sciences of the United States of America* **99,** 11573–11578. ISSN: 0027-8424. https://www.ncbi.nlm.nih.gov/pmc/articles/PMC129310/ (2021) (Sept. 3, 2002).

81. Carrara, P., Stano, P. & Luisi, P. L. Giant Vesicles "Colonies": A Model for Primitive Cell Communities. *ChemBioChem* **13,** 1497–1502. ISSN: 14394227. http://doi.wiley.com/10.1002/cbic.201200133 (2021) (July 9, 2012).

82. Mantri, S., Tanuj Sapra, K., Cheley, S., Sharp, T. H. & Bayley, H. An engineered dimeric protein pore that spans adjacent lipid bilayers. *Nature Communications* **4,** 1725. ISSN: 2041-1723. https://www.nature.com/articles/ncomms2726 (2021) (Apr. 16, 2013).

83. Hadorn, M., Boenzli, E. & Hanczyc, M. M. Specific and Reversible DNA-Directed Self-Assembly of Modular Vesicle-Droplet Hybrid Materials. *Langmuir* **32,** 3561–3566. ISSN: 0743-7463. https://doi.org/10.1021/acs.langmuir.5b04003 (2021) (Apr. 19, 2016).

84. Villringer, S. *et al.* Lectin-mediated protocell crosslinking to mimic cell-cell junctions and adhesion. *Scientific Reports* **8,** 1932. ISSN: 2045-2322. https://www.nature.com/articles/s41598-018-20230-6 (2021) (Jan. 31, 2018).

85. Bolognesi, G. *et al.* Sculpting and fusing biomimetic vesicle networks using optical tweezers. *Nature Communications* **9,** 1882. ISSN: 2041-1723. https://www.nature.com/articles/s41467-018-04282-w (2021) (May 14, 2018).

86. Li, Q., Li, S., Zhang, X., Xu, W. & Han, X. Programmed magnetic manipulation of vesicles into spatially coded prototissue architectures arrays. *Nature Communications* **11,** 232. ISSN: 2041-1723. https://www.nature.com/articles/s41467-019-14141-x (2021) (Jan. 13, 2020).

87. Funakoshi, K., Suzuki, H. & Takeuchi, S. Lipid Bilayer Formation by Contacting Monolayers in a Microfluidic Device for Membrane Protein Analysis. *Analytical Chemistry* **78,** 8169–8174. ISSN: 0003-2700. https://doi.org/10.1021/ac0613479 (2021) (Dec. 1, 2006).

88. Bayley, H. *et al.* Droplet interface bilayers. *Molecular bioSystems* **4,** 1191–1208. ISSN: 1742-206X. https://www.ncbi.nlm.nih.gov/pmc/articles/PMC2763081/ (2021) (Dec. 2008).

89. Wauer, T. *et al.* Construction and Manipulation of Functional Three-Dimensional Droplet Networks. *ACS Nano* **8,** 771–779. ISSN: 1936-0851, 1936-086X. https://pubs.acs.org/doi/10.1021/nn405433y (2021) (Jan. 28, 2014).

90. Dupin, A. & Simmel, F. C. Signalling and differentiation in emulsion-based multi-compartmentalized in vitro gene circuits. *Nature Chemistry* **11,** 32–39. ISSN: 1755-4349. https://www.nature.com/articles/s41557-018-0174-9 (2021) (Jan. 2019).

91. Bachler, S., Haidas, D., Ort, M., Duncombe, T. A. & Dittrich, P. S. Microfluidic platform enables tailored translocation and reaction cascades in nanoliter droplet networks. *Communications Biology* **3,** 1–9. ISSN: 2399-3642. https://www.nature.com/articles/s42003-020-01489-w (2021) (Dec. 14, 2020).

92. Villar, G., Graham, A. D. & Bayley, H. A Tissue-Like Printed Material. *Science* **340,** 48–52. ISSN: 0036-8075, 1095-9203. https://science.sciencemag.org/content/340/6128/48 (2021) (Apr. 5, 2013).

93. Alcinesio, A. *et al.* Controlled packing and single-droplet resolution of 3D-printed functional synthetic tissues. *Nature Communications* **11,** 2105. ISSN: 2041-1723. https://www.nature.com/articles/s41467-020-15953-y (2021) (Apr. 30, 2020).

94. Bayoumi, M., Bayley, H., Maglia, G. & Sapra, K. T. Multi-compartment encapsulation of communicating droplets and droplet networks in hydrogel as a model for artificial cells. *Scientific Reports* **7.** ISSN: 2045-2322. https://www.ncbi.nlm.nih.gov/pmc/articles/PMC5377250/ (2021) (Apr. 3, 2017).

95. Baxani, D. K. *et al.* Bilayer Networks within a Hydrogel Shell: A Robust Chassis for Artificial Cells and a Platform for Membrane Studies. *Angewandte Chemie International Edition* **55,** 14240–14245. ISSN: 1521-3773. https://onlinelibrary.wiley.com/doi/abs/10.1002/anie.201607571 (2021) (2016).

96. Villar, G., Heron, A. J. & Bayley, H. Formation of droplet networks that function in aqueous environments. *Nature Nanotechnology* **6,** 803–808. ISSN: 1748-3395. https://www.nature.com/articles/nnano.2011.183 (2021) (Dec. 2011).

97. Booth, M. J., Cazimoglu, I. & Bayley, H. Controlled deprotection and release of a small molecule from a compartmented synthetic tissue module. *Communications Chemistry* **2,** 1–8. ISSN: 2399-3669. https://www.nature.com/articles/s42004-019-0244-y (2021) (Dec. 12, 2019).

98. Booth, M. J., Schild, V. R., Graham, A. D., Olof, S. N. & Bayley, H. Light-activated communication in synthetic tissues. *Science Advances* **2,** e1600056. ISSN: 2375-2548. https://advances.sciencemag.org/content/2/4/e1600056 (2021) (Apr. 1, 2016).

99. Booth, M. J., Restrepo Schild, V., Box, S. J. & Bayley, H. Light-patterning of synthetic tissues with single droplet resolution. *Scientific Reports* **7,** 9315. ISSN: 2045-2322. https://www.nature.com/articles/s41598-017-09394-9 (2021) (Aug. 24, 2017).

100. Team, T. E. PDMS in biology research: A critical review on PDMS lithography for biological studies. *Elveflow.* https://www.elveflow.com/microfluidic-reviews/microfluidics-for-cell-biology/pdms-in-biology-researches-a-critical-review-on-pdms-lithography-for-biological-studies/ (2021) (Jan. 6, 2021).

101. Damiati, S., Kompella, U. B., Damiati, S. A. & Kodzius, R. Microfluidic Devices for Drug Delivery Systems and Drug Screening. *Genes* **9,** 103. https://www.mdpi.com/2073-4425/9/2/103 (2021) (Feb. 2018).

102. Fontana, F., Ferreira, M. P. A., Correia, A., Hirvonen, J. & Santos, H. A. Microfluidics as a cutting-edge technique for drug delivery applications. *Journal of Drug Delivery Science and Technology. Special Issue: Scandinavia* **34,** 76–87. ISSN: 1773-2247. https://www.sciencedirect.com/science/article/pii/S1773224716300235 (2021) (Aug. 1, 2016).

103. Chong, D. *et al.* Advances in fabricating double-emulsion droplets and their biomedical applications. *Microfluidics and Nanofluidics* **19,** 1071–1090. ISSN: 1613-4990. https://doi.org/10.1007/s10404-015-1635-8 (2021) (Nov. 1, 2015).

104. Kaimainen, M., Marze, S., Järvenpää, E., Anton, M. & Huopalahti, R. Encapsulation of betalain into w/o/w double emulsion and release during in vitro intestinal lipid digestion. *LWT - Food Science and Technology* **60,** 899–904. ISSN: 0023-6438. http://www.sciencedirect.com/science/article/pii/S0023643814006379 (2021) (Mar. 1, 2015).

105. Mutaliyeva, B. *et al.* Microencapsulation of insulin and its release using w/o/w double emulsion method. *Colloids and Surfaces A: Physicochemical and Engineering Aspects. Dynamics of wetting by surfactant solutions* **521,** 147–152. ISSN: 0927-7757. http://www.sciencedirect.com/science/article/pii/S0927775716309001 (2021) (May 20, 2017).

106. Michelon, M., Huang, Y., de la Torre, L. G., Weitz, D. A. & Cunha, R. L. Single-step microfluidic production of W/O/W double emulsions as templates for -carotene-loaded giant liposomes formation. *Chemical Engineering Journal*

366, 27–32. ISSN: 1385-8947. http://www.sciencedirect.com/science/article/pii/S1385894719302384 (2021) (June 15, 2019).

107. Liu, L. *et al.* Preparation of monodisperse calcium alginate microcapsules via internal gelation in microfluidic-generated double emulsions. *Journal of Colloid and Interface Science* **404,** 85–90. ISSN: 0021-9797. http://www.sciencedirect.com/science/article/pii/S0021979713004037 (2021) (Aug. 15, 2013).

108. Ren, P.-W., Ju, X.-J., Xie, R. & Chu, L.-Y. Monodisperse alginate microcapsules with oil core generated from a microfluidic device. *Journal of Colloid and Interface Science* **343,** 392–395. ISSN: 0021-9797. http://www.sciencedirect.com/science/article/pii/S0021979709014489 (2021) (Mar. 1, 2010).

109. Nie, Z., Xu, S., Seo, M., Lewis, P. C. & Kumacheva, E. Polymer Particles with Various Shapes and Morphologies Produced in Continuous Microfluidic Reactors. *Journal of the American Chemical Society* **127,** 8058–8063. ISSN: 0002-7863. https://doi.org/10.1021/ja042494w (2021) (June 1, 2005).

110. Ai, Y., Xie, R., Xiong, J. & Liang, Q. Microfluidics for Biosynthesizing: from Droplets and Vesicles to Artificial Cells. *Small* **16,** 1903940. ISSN: 1613-6829. https://onlinelibrary.wiley.com/doi/abs/10.1002/smll.201903940 (2021) (2020).

111. Deng, N.-N., Yelleswarapu, M. & Huck, W. T. S. Monodisperse Uni- and Multicompartment Liposomes. *Journal of the American Chemical Society* **138,** 7584–7591. ISSN: 0002-7863. https://doi.org/10.1021/jacs.6b02107 (2021) (June 22, 2016).

112. Debon, A. P., Wootton, R. C. R. & Elvira, K. S. Droplet confinement and leakage: Causes, underlying effects, and amelioration strategies. *Biomicrofluidics* **9,** 024119. https://aip.scitation.org/doi/abs/10.1063/1.4917343 (2021) (Mar. 1, 2015).

113. Becker, H. It's the economy... *Lab on a Chip* **9,** 2759–2762. ISSN: 1473-0189. https://pubs.rsc.org/en/content/articlelanding/2009/lc/b916505n (2021) (Oct. 7, 2009).

114. Gale, B. K. *et al.* A Review of Current Methods in Microfluidic Device Fabrication and Future Commercialization Prospects. *Inventions* **3,** 60. https://www.mdpi.com/2411-5134/3/3/60 (2021) (Sept. 2018).

115. Hwang, J., Cho, Y. H., Park, M. S. & Kim, B. H. Microchannel Fabrication on Glass Materials for Microfluidic Devices. *International Journal of Precision Engineering and Manufacturing* **20,** 479–495. ISSN: 2005-4602. https://doi.org/10.1007/s12541-019-00103-2 (2021) (Mar. 1, 2019).

116. Utada, A. S. *et al.* Monodisperse Double Emulsions Generated from a Microcapillary Device. *Science* **308,** 537–541. ISSN: 0036-8075, 1095-9203. https://science.sciencemag.org/content/308/5721/537 (2021) (Apr. 22, 2005).

117. Designer emulsions using microfluidics. *Materials Today* **11,** 18–27. ISSN: 1369-7021. https://www.sciencedirect.com/science/article/pii/S1369702108700531 (2021) (Apr. 1, 2008).

118. Iwasa, Y., Yamanoi, K., Kaneyasu, Y. & Norimatsu, T. Controlled Generation of Double Emulsions for Laser Fusion Target Fabrication Using a Glass Capillary Microfluidic Device. *Fusion Science and Technology* **73,** 258–264. ISSN: 1536-1055. https://doi.org/10.1080/15361055.2017.1372988 (2021) (Feb. 17, 2018).

119. Levenstein, M. A. *et al.* A reproducible approach to the assembly of microcapillaries for double emulsion production. *Microfluidics and Nanofluidics* **20,** 143. ISSN: 1613-4990. https://doi.org/10.1007/s10404-016-1806-2 (2021) (Oct. 7, 2016).

120. Versatile reconfigurable glass capillary microfluidic devices with Lego® inspired blocks for drop generation and micromixing. *Journal of Colloid and Interface Science* **542,** 23–32. ISSN: 0021-9797. https://www.sciencedirect.com/science/article/pii/S0021979719301407 (2021) (Apr. 15, 2019).

121. Benson, B. R., Stone, H. A. & Prud'homme, R. K. An "off-the-shelf" capillary microfluidic device that enables tuning of the droplet breakup regime at constant flow rates. *Lab on a Chip* **13,** 4507–4511. ISSN: 1473-0189. https://pubs.rsc.org/en/content/articlelanding/2013/lc/c3lc50804h (2021) (Oct. 30, 2013).

122. Zhang, J. M., Aguirre-Pablo, A. A., Li, E. Q., Buttner, U. & Thoroddsen, S. T. Droplet generation in cross-flow for cost-effective 3D-printed "plug-and-play" microfluidic devices. *RSC Advances* **6,** 81120–81129. ISSN: 2046-2069. https://pubs.rsc.org/en/content/articlelanding/2016/ra/c6ra11724d (2021) (Aug. 25, 2016).

123. Meng, Z.-J. *et al.* Plug-n-play microfluidic systems from flexible assembly of glass-based flow-control modules. *Lab on a Chip* **15,** 1869–1878. ISSN: 1473-0189. https://pubs.rsc.org/en/content/articlelanding/2015/lc/c5lc00132c (2021) (Mar. 31, 2015).

124. Martino, C., Berger, S., Wootton, R. C. R. & deMello, A. J. A 3D-printed microcapillary assembly for facile double emulsion generation. *Lab on a Chip* **14,** 4178–4182. ISSN: 1473-0189. https://pubs.rsc.org/en/content/articlelanding/2014/lc/c4lc00992d (2021) (Sept. 30, 2014).

125. Zhou, Z., Kong, T., Mkaouar, H., Salama, K. N. & Zhang, J. M. A hybrid modular microfluidic device for emulsion generation. *Sensors and Actuators A: Physical* **280,** 422–428. ISSN: 0924-4247. http://www.sciencedirect.com/science/article/pii/S0924424718307180 (2021) (Sept. 1, 2018).

126. Ramsay, K., Levy, J., Gobbo, P. & Elvira, K. *Programmed Assembly of Bespoke Prototissue Spheroids on a Microfluidic Platform* preprint (Dec. 28, 2020). https://chemrxiv.org/articles/preprint/Programmed_Assembly_of_Bespoke_Prototissue_Spheroids_on_a_Microfluidic_Platform/13487247/1 (2021).

127. Zhao, C. *et al.* Engineering proteinosomes with renewable predatory behaviour towards living organisms. *Materials Horizons* **7,** 157–163. ISSN: 2051-6355. https://pubs.rsc.org/en/content/articlelanding/2020/mh/c9mh00976k (2020) (Jan. 2, 2020).

128. Chen, I. A. & Walde, P. From Self-Assembled Vesicles to Protocells. *Cold Spring Harbor Perspectives in Biology* **2.** ISSN: 1943-0264. https://www.ncbi.nlm.nih.gov/pmc/articles/PMC2890201/ (2020) (July 2010).

129. Chen, I. A. & Szostak, J. W. Membrane growth can generate a transmembrane pH gradient in fatty acid vesicles. *Proceedings of the National Academy of Sciences* **101,** 7965–7970. ISSN: 0027-8424, 1091-6490. https://www.pnas.org/content/101/21/7965 (2020) (May 25, 2004).

130. Hwang, S., Choi, C.-H. & Lee, C.-S. Regioselective surface modification of pdms microfluidic device for the generation of monodisperse double emulsions. *Macromolecular Research* **20,** 422–428. ISSN: 2092-7673. https://doi.org/10.1007/s13233-012-0048-8 (2020) (Apr. 1, 2012).

131. Li, S. *et al.* Rapid preparation of highly reliable PDMS double emulsion microfluidic devices. *RSC Advances* **6,** 25927–25933. ISSN: 2046-2069. https://pubs.rsc.org/en/content/articlelanding/2016/ra/c6ra03225g (2020) (Mar. 8, 2016).

132. Bauer, W.-A. C., Fischlechner, M., Abell, C. & Huck, W. T. S. Hydrophilic PDMS microchannels for high-throughput formation of oil-in-water microdroplets

and water-in-oil-in-water double emulsions. *Lab on a Chip* **10,** 1814–1819. ISSN: 1473-0189. https://pubs.rsc.org/en/content/articlelanding/2010/lc/c004046k (2021) (June 29, 2010).

133. Trantidou, T., Elani, Y., Parsons, E. & Ces, O. Hydrophilic surface modification of PDMS for droplet microfluidics using a simple, quick, and robust method via PVA deposition. *Microsystems & Nanoengineering* **3,** 1–9. ISSN: 2055-7434. https://www.nature.com/articles/micronano201691 (2020) (Apr. 24, 2017).

134. Vladisavljević, G. T., Al Nuumani, R. & Nabavi, S. A. Microfluidic Production of Multiple Emulsions. *Micromachines* **8.** ISSN: 2072-666X. https://www.ncbi.nlm.nih.gov/pmc/articles/PMC6190154/ (2021) (Mar. 2, 2017).

135. *Dropletex — Droplet microfluidic experts* https://dropletex.com/ (2021).

136. Nisisako, T., Okushima, S. & Torii, T. Controlled formulation of monodisperse double emulsions in a multiple-phase microfluidic system. *Soft Matter* **1,** 23–27. ISSN: 1744-6848. https://pubs.rsc.org/en/content/articlelanding/2005/sm/b501972a (2021) (May 27, 2005).

137. Deng, N.-N., Yelleswarapu, M., Zheng, L. & Huck, W. T. S. Microfluidic Assembly of Monodisperse Vesosomes as Artificial Cell Models. *Journal of the American Chemical Society* **139,** 587–590. ISSN: 0002-7863, 1520-5126. https://pubs.acs.org/doi/10.1021/jacs.6b10977 (2021) (Jan. 18, 2017).

138. Sathi, A., Viswanad, V., Aneesh, T. P. & Kumar, B. A. Pros and cons of phospholipid asymmetry in erythrocytes. *Journal of Pharmacy & Bioallied Sciences* **6,** 81–85. ISSN: 0976-4879. https://www.ncbi.nlm.nih.gov/pmc/articles/PMC3983750/ (2021) (2014).

139. Romanov, V., McCullough, J., Gale, B. K. & Frost, A. A Tunable Microfluidic Device Enables Cargo Encapsulation by Cell- or Organelle-Sized Lipid Vesicles

Comprising Asymmetric Lipid Bilayers. *Advanced Biosystems* **3,** 1900010. ISSN: 2366-7478. https://onlinelibrary.wiley.com/doi/abs/10.1002/adbi.201900010 (2021) (2019).

140. Matosevic, S. & Paegel, B. M. Layer-by-layer cell membrane assembly. *Nature Chemistry* **5,** 958–963. ISSN: 1755-4349. https://www.nature.com/articles/nchem.1765 (2021) (Nov. 2013).

141. Kamiya, K., Osaki, T. & Takeuchi, S. Formation of vesicles-in-a-vesicle with asymmetric lipid components using a pulsed-jet flow method. *RSC Advances* **9,** 30071–30075. ISSN: 2046-2069. https://pubs.rsc.org/en/content/articlelanding/2019/ra/c9ra04622d (2021) (Sept. 23, 2019).

142. Gotanda, M., Kamiya, K., Osaki, T., Miki, N. & Takeuchi, S. Automatic generation system of cell-sized liposomes. *Sensors and Actuators B: Chemical* **292,** 57–63. ISSN: 0925-4005. https://www.sciencedirect.com/science/article/pii/S0925400519306197 (2021) (Aug. 1, 2019).

143. Lu, L., Schertzer, J. W. & Chiarot, P. R. Continuous microfluidic fabrication of synthetic asymmetric vesicles. *Lab on a Chip* **15,** 3591–3599. ISSN: 1473-0189. https://pubs.rsc.org/en/content/articlelanding/2015/lc/c5lc00520e (2021) (Aug. 11, 2015).

144. Swaay, D. v. & deMello, A. Microfluidic methods for forming liposomes. *Lab on a Chip* **13,** 752–767. ISSN: 1473-0189. https://pubs.rsc.org/en/content/articlelanding/2013/lc/c2lc41121k (2021) (Feb. 5, 2013).

145. Deshpande, S. & Dekker, C. On-chip microfluidic production of cell-sized liposomes. *Nature Protocols* **13,** 856–874. ISSN: 1750-2799. https://www.nature.com/articles/nprot.2017.160 (2021) (May 2018).

146. Lee, J. N., Park, C. & Whitesides, G. M. Solvent Compatibility of Poly(dimethylsiloxane)-Based Microfluidic Devices. *Analytical Chemistry* **75,** 6544–6554. ISSN: 0003-2700. https://doi.org/10.1021/ac0346712 (2021) (Dec. 1, 2003).

147. Lee, J. *et al.* Effect of thermal treatment on the chemical resistance of polydimethylsiloxane for microfluidic devices. *Journal of Micromechanics and Microengineering* **23,** 035007. ISSN: 0960-1317, 1361-6439. https://iopscience.iop.org/article/10.1088/0960-1317/23/3/035007 (2021) (Mar. 1, 2013).

148. Carugo, D., Bottaro, E., Owen, J., Stride, E. & Nastruzzi, C. Liposome production by microfluidics: potential and limiting factors. *Scientific Reports* **6,** 25876. ISSN: 2045-2322. https://www.nature.com/articles/srep25876 (2021) (May 19, 2016).

149. Barlow, N. E. *et al.* Rheological Droplet Interface Bilayers (rheo-DIBs): Probing the Unstirred Water Layer Effect on Membrane Permeability via Spinning Disk Induced Shear Stress. *Scientific Reports* **7,** 17551. ISSN: 2045-2322. https://www.nature.com/articles/s41598-017-17883-0 (2021) (Dec. 14, 2017).

150. Verkleij, A. J. *et al.* The asymmetric distribution of phospholipids in the human red cell membrane. A combined study using phospholipases and freeze-etch electron microscopy. *Biochimica et Biophysica Acta (BBA) - Biomembranes* **323,** 178–193. ISSN: 0005-2736. https://www.sciencedirect.com/science/article/pii/0005273673901430 (2021) (Oct. 11, 1973).

151. Gershfeld, N. L. & Murayama, M. Thermal instability of red blood cell membrane bilayers: Temperature dependence of hemolysis. *The Journal of Membrane Biology* **101,** 67–72. ISSN: 1432-1424. https://doi.org/10.1007/BF01872821 (2021) (Dec. 1, 1988).

152. Marquardt, D., Geier, B. & Pabst, G. Asymmetric Lipid Membranes: Towards More Realistic Model Systems. *Membranes* **5,** 180–196. ISSN: 2077-0375. http://www.mdpi.com/2077-0375/5/2/180 (2021) (May 6, 2015).

153. Vahedi, A., Bigdelou, P. & Farnoud, A. M. Quantitative analysis of red blood cell membrane phospholipids and modulation of cell-macrophage interactions using cyclodextrins. *Scientific Reports* **10,** 15111. ISSN: 2045-2322. https://www.nature.com/articles/s41598-020-72176-3 (2021) (Sept. 15, 2020).

154. Achan, J. *et al.* Quinine, an old anti-malarial drug in a modern world: role in the treatment of malaria. *Malaria Journal* **10,** 144. ISSN: 1475-2875. https://doi.org/10.1186/1475-2875-10-144 (2021) (May 24, 2011).

155. O'Reilly, J. E. Fluorescence experiments with quinine. *Journal of Chemical Education* **52,** 610. ISSN: 0021-9584. https://doi.org/10.1021/ed052p610 (2021) (Sept. 1, 1975).

156. Kapishnikov, S. *et al.* Mode of action of quinoline antimalarial drugs in red blood cells infected by Plasmodium falciparum revealed in vivo. *Proceedings of the National Academy of Sciences* **116,** 22946–22952. ISSN: 0027-8424, 1091-6490. https://www.pnas.org/content/116/46/22946 (2021) (Nov. 12, 2019).

157. Baicu, S. C. & Taylor, M. J. Acid–base buffering in organ preservation solutions as a function of temperature: new parameters for comparing buffer capacity and efficiency. *Cryobiology* **45,** 33–48. ISSN: 00112240. https://linkinghub.elsevier.com/retrieve/pii/S0011224002001049 (2021) (Aug. 2002).

158. Korner, J. L., Stephenson, E. B. & Elvira, K. S. A bespoke microfluidic pharmacokinetic compartment model for drug absorption using artificial cell membrane. *Lab on a Chip,* 10.1039.D0LC00263A. ISSN: 1473-0197, 1473-0189. http:

//pubs.rsc.org/en/Content/ArticleLanding/2020/LC/D0LC00263A (2020) (2020).

159. Yewdall, N. A., Mason, A. F. & van Hest, J. C. M. The hallmarks of living systems: towards creating artificial cells. *Interface Focus* **8,** 20180023. https://royalsocietypublishing.org/doi/full/10.1098/rsfs.2018.0023 (2020) (Oct. 6, 2018).

160. Pohorille, A. & Deamer, D. Artificial cells: prospects for biotechnology. *Trends in Biotechnology* **20,** 123–128. ISSN: 0167-7799 (Mar. 2002).

161. Kurihara, K. *et al.* A recursive vesicle-based model protocell with a primitive model cell cycle. *Nature Communications* **6,** 8352. ISSN: 2041-1723. https://www.nature.com/articles/ncomms9352 (2020) (Sept. 29, 2015).

162. Kamat, N. P., Tobé, S., Hill, I. T. & Szostak, J. W. Electrostatic Localization of RNA to Protocell Membranes by Cationic Hydrophobic Peptides. *Angewandte Chemie (International Ed. in English)* **54,** 11735–11739. ISSN: 1521-3773 (Sept. 28, 2015).

163. Mason, A. F. & Thordarson, P. Polymersomes as protocellular constructs. *Journal of Polymer Science Part A: Polymer Chemistry* **55,** 3817–3825. ISSN: 1099-0518. https://onlinelibrary.wiley.com/doi/abs/10.1002/pola.28780 (2020) (2017).

164. Kubilis, A., Abdulkarim, A., Eissa, A. M. & Cameron, N. R. Giant Polymersome Protocells Dock with Virus Particle Mimics via Multivalent Glycan-Lectin Interactions. *Scientific Reports* **6,** 32414. ISSN: 2045-2322. https://www.nature.com/articles/srep32414 (2020) (Aug. 31, 2016).

165. Jang, W.-S. *et al.* Enzymatically triggered rupture of polymersomes. *Soft Matter* **12,** 1014–1020. ISSN: 1744-6848. https://pubs.rsc.org/en/content/articlelanding/2016/sm/c5sm01881a (2020) (Jan. 20, 2016).

166. Torre, P. *et al.* Encapsulation of hydrophobic components in dendrimersomes and decoration of their surface with proteins and nucleic acids. *Proceedings of the National Academy of Sciences* **116,** 15378–15385. ISSN: 0027-8424, 1091-6490. https://www.pnas.org/content/116/31/15378 (2020) (July 30, 2019).

167. Douliez, J.-P. *et al.* Preparation of Swellable Hydrogel-Containing Colloidosomes from Aqueous Two-Phase Pickering Emulsion Droplets. *Angewandte Chemie International Edition* **57,** 7780–7784. ISSN: 1521-3773. https://onlinelibrary.wiley.com/doi/abs/10.1002/anie.201802929 (2020) (2018).

168. Miguel, A. S. & Behrens, S. H. Permeability control in stimulus-responsive colloidosomes. *Soft Matter* **7,** 1948–1956. ISSN: 1744-6848. https://pubs.rsc.org/en/content/articlelanding/2011/sm/c0sm01107j (2020) (Feb. 22, 2011).

169. Martin, N., Li, M. & Mann, S. Selective Uptake and Refolding of Globular Proteins in Coacervate Microdroplets. *Langmuir* **32,** 5881–5889. ISSN: 0743-7463. https://doi.org/10.1021/acs.langmuir.6b01271 (2020) (June 14, 2016).

170. Fothergill, J., Li, M., Davis, S. A., Cunningham, J. A. & Mann, S. Nanoparticle-Based Membrane Assembly and Silicification in Coacervate Microdroplets as a Route to Complex Colloidosomes. *Langmuir* **30,** 14591–14596. ISSN: 0743-7463. https://doi.org/10.1021/la503746u (2020) (Dec. 9, 2014).

171. Mason, A. F., Buddingh', B. C., Williams, D. S. & van Hest, J. C. M. Hierarchical Self-Assembly of a Copolymer-Stabilized Coacervate Protocell. *Journal of the American Chemical Society* **139,** 17309–17312. ISSN: 0002-7863. https://www.ncbi.nlm.nih.gov/pmc/articles/PMC5724030/ (2020) (Dec. 6, 2017).

172. Huang, X., Patil, A. J., Li, M. & Mann, S. Design and Construction of Higher-Order Structure and Function in Proteinosome-Based Protocells. *Journal of the American Chemical Society* **136,** 9225–9234. ISSN: 0002-7863. https://doi.org/10.1021/ja504213m (2020) (June 25, 2014).

173. Wang, T. *et al.* Giant "Breathing" Proteinosomes with Jellyfish-like Property. *ACS applied materials & interfaces* **11,** 47619–47624. ISSN: 1944-8252 (Dec. 18, 2019).

174. Wang, X. *et al.* Chemical Information Exchange in Organized Protocells and Natural Cell Assemblies with Controllable Spatial Positions. *Small* **16,** 1906394. ISSN: 1613-6829. https://onlinelibrary.wiley.com/doi/abs/10.1002/smll.201906394 (2020) (2020).

175. Ugrinic, M., deMello, A. & Tang, T.-Y. D. Microfluidic Tools for Bottom-Up Synthetic Cellularity. *Chem* **5,** 1727–1742. ISSN: 2451-9294, 2451-9308. https://www.cell.com/chem/abstract/S2451-9294(19)30116-0 (2020) (July 11, 2019).

176. Staufer, O., Schröter, M., Platzman, I. & Spatz, J. P. Bottom-Up Assembly of Functional Intracellular Synthetic Organelles by Droplet-Based Microfluidics. *Small* **16,** 1906424. ISSN: 1613-6829. https://www.onlinelibrary.wiley.com/doi/abs/10.1002/smll.201906424 (2020) (2020).

177. Can Bottom-Up Synthetic Biology Generate Advanced Drug-Delivery Systems? *Trends in Biotechnology.* ISSN: 0167-7799. https://www.sciencedirect.com/science/article/pii/S0167779920302109 (2020) (Sept. 7, 2020).

178. Song, H., Tice, J. D. & Ismagilov, R. F. A Microfluidic System for Controlling Reaction Networks in Time. *Angewandte Chemie International Edition* **42,** 768–772. ISSN: 1521-3773. https://onlinelibrary.wiley.com/doi/abs/10.1002/anie.200390203 (2021) (2003).

179. Joseph, A. *et al.* Chemotactic synthetic vesicles: Design and applications in blood-brain barrier crossing. *Science Advances* **3,** e1700362. ISSN: 2375-2548. https://advances.sciencemag.org/content/3/8/e1700362 (2020) (Aug. 1, 2017).

180. Pijpers, I. A. B. *et al.* Hybrid Biodegradable Nanomotors through Compartmentalized Synthesis. *Nano Letters* **20,** 4472–4480. ISSN: 1530-6984. https://doi.org/10.1021/acs.nanolett.0c01268 (2020) (June 10, 2020).